

Direct Coupling Feasibility Evaluation

Tom Schoehuijs

Delft University of Technology

Direct Coupling Feasibility Evaluation

Predicting the Price of Hydrogen Produced by
Solar Energy

by

Tom Schoehuijs

to obtain the degree of Master of Science
at the Delft University of Technology,
to be defended publicly on Friday, July 20th, 2018 at 10:00.

Student number:	4205650
Project duration:	December 2017 – July 2018
Thesis committee:	Prof. Dr. J.J.C. Geerlings, TU Delft, Supervisor
	Prof. Dr. F.M. Mulder, TU Delft
	Dr. O. Isabella, TU Delft
	Dr. A. Higler, Shell, Supervisor

This thesis is confidential and cannot be made public until July 20th, 2020.

An electronic version of this thesis is available at <http://repository.tudelft.nl/>.

Preface

Before you lies the dissertation "Direct Coupling Feasibility Evaluation: Predicting the Price of Hydrogen Produced by Solar Energy". It has been written to fulfill the graduation requirements of the Sustainable Energy Technology MSc at the Faculty of Electrical Engineering, Mathematics and Computer Science at Delft University of Technology. I was engaged in researching and writing this dissertation from December 2017 to July 2018.

The project was undertaken at the request of the New Energies Research and Technology (NERT) group within Shell, where I undertook an internship. My research question was formulated together with both my supervisors, Prof. Hans Geerlings and Dr. Arnoud Higler.

I would like to thank my supervisors for their excellent guidance and support during this process. I also wish to thank a number of others from Shell who helped me model and generate the content of this report, including Sipke Wadman, Jeff Martin, Jayakrishnan (Jay) Harikumaran, Tatiana Kozlova, and Quirine Dechesne. To my other colleagues at Shell: I would like to thank you for your wonderful cooperation as well. It was always helpful to be in the office and bounce ideas off of you.

For my family and Cerianne a particular note of thanks: your wise counsel and kind words have, as always, served me well and kept me on the right track. I'd finally also like to thank Tim de Vries for helping in brainstorming, problem-solving and for reviewing this report.

I hope you enjoy reading this report as much as I enjoyed working on it.

*Tom Schoehuijs
Amsterdam, July 2018*

Executive Summary

This report aims to evaluate the feasibility of a small pilot plant placed near Broome, Australia to produce 3 tons of hydrogen per day using photovoltaic (PV) energy. Using PVsyst, a PV modelling software, the maximum power operating points were determined for a test layout. This was then transformed to other layouts which allowed the optimum layout to be found for a system connected to electrolyzers using maximum power point tracking technology. A second scenario using a battery was also modelled and optimized. Finally, the third scenario used direct coupling, meaning that the PV panels were not operated at their maximum power point but rather at where the electrolyzer and PV current and voltage lines crossed. This resulted in a lower power yield but also lower costs. To find the current and voltage curve for the PV field, the data from PVsyst analyzed to find the short circuit current and the open circuit voltage. This allowed the full current and voltage curve to be determined, which allowed the intersection point with the (experimental) electrolyzer current and voltage curve to be determined.

In all simulations piping storage was used to remove the intermittency of the hydrogen production by having a capacity of 3 tons of gaseous H_2 . This ensures a constant stream of hydrogen to the liquefaction system.

Using preliminary results an electrolyzer degradation simulation was carried out, to find how the electrolyzer would behave after 20 years of use. Although the influence of intermittency could not be found in literature, it was shown that the electrolyzer produces, on average during its 20 year lifetime, approximately 5.7% less hydrogen than it would without any degradation. This has been included in all financial analyses carried out in this report, along with a 7% weighted average cost of capital.

The financial framework has been based off of a number of different sources and forecasts. Due to the limitations of publicly available data some forecasts were replaced with constant prices which do not evolve throughout the years.

Using the hydrogen production models and financial frameworks it is possible to compare the different scenarios. From this a price of 4.16\$ kg^{-1} was found for a MPP coupled system, 4.39\$ kg^{-1} for a MPP coupled system including a battery, and 4.02\$ kg^{-1} for a direct coupled system. The third scenario was furthermore looked at in terms of physical layout; it was found that the decentralized layout consisting of smaller subplots was slightly more expensive than the standard centralized layout (4.09\$ kg^{-1}). For this pilot plant it is advised to use a decentralized topology, combined with a decentralized layout consisting of multiple smaller plots. Although the centralized layout is slightly cheaper, it contains more system critical components which could cause a large portion of the system to be inactive if they are broken.

Contents

Contents	v
List of Figures	ix
List of Tables	xi
1 Introduction	1
1.1 Electrolyzers	1
1.2 Photovoltaics	2
1.3 System components.	2
1.4 Scenarios	2
2 Electrolyzers	5
2.1 Electrolyzer Model	7
2.2 Utility energy costs	9
2.3 Electrolyzer degradation and lifetime	10
3 PV Systems	13
3.1 The One Diode Model	15
3.2 Diode Ideality Factor	18
3.3 Calculating the open circuit voltage and short circuit current	20
3.4 Intersection points for DC connection	24
4 System components	27
4.1 Transformers and inverters.	27
4.2 Battery	27
4.3 Hydrogen storage	28
4.4 Cabling	28
5 Model tools	31
5.1 Dependency	31
5.2 Ramping	32
6 Economic Evaluation	35
6.1 Layout.	35
6.2 Electrolyzer	36
6.3 Photovoltaics	36
6.4 Battery costs	38
6.5 Piping	38
6.6 Cable costs	39
6.7 Hydrogen storage	39
6.8 Transformers and inverters.	39
7 Results and Discussion	41
7.1 Scenario topology optimization	41
7.1.1 Scenario 1: MPPT technology	41
7.1.2 Scenario 2: MPPT technology with battery.	43
7.1.3 Scenario 3: Direct coupling	45
7.1.4 Scenario comparison	47

7.2	Layout	48
7.2.1	Centralized layout	48
7.2.2	Decentralized layout	52
7.3	Sensitivity Analysis	56
7.4	Ramping	58
8	Summary and recommendations	61
8.1	Out of scope	62
8.2	Suggestions for further research	62
	Bibliography	65
	Appendix	73
A	PV panel characteristics	73
B	SMA Central Inverter Datasheet.	74

List of Figures

1.1	A schematic of the different topologies possible.	3
2.1	A Hydrogenics alkaline electrolyzer [44].	5
2.2	The basis of alkaline electrolysis [91].	6
2.3	Characteristic I-V curves for electrolyzers at 25°C and 65°C and 20 bar [98].	7
2.4	An example I-V curve for an alkaline electrolyzer, using data from [54] and operating points from [44].	8
2.5	Hydrogen production from a single cell.	9
2.6	Electrolyzer degradation after a lifetime of 20 years (intermittent usage).	12
3.1	An example I-V curve for a typical PV cell.	13
3.2	An overview of terms frequently used to describe PV systems, taken from [89].	14
3.3	A schematic of the one diode model, adapted from [86].	15
3.4	Shift of the I-V curve due to the Newton-Raphson method. The blue line represents the initial guess, and the red line indicates the final I-V curve. This system uses 769 strings in parallel and 20 in series and is only meant as an illustration.	17
3.5	A schematic of the two diode model, adapted from [86].	18
3.6	Error in P_{mpp} at varying temperatures [93].	18
3.7	Variations in DIF as a result of varying operating conditions. The red dot indicates NOCT conditions.	20
3.8	All I-V and P-V curves have different V_{oc} and I_{sc} values and go through the MPP as defined by PVsyst, shown in red. However, only one has the MPP shown in red at its maximum. This line is indicated in green.	21
3.9	Finding the V_{oc} and I_{sc} (corrected to 1000 W m ⁻²) from PVsyst data for irradiances more than 100 W m ⁻²	22
3.10	Comparing the V_{mpp} 's from PVsyst and the reconstructed I-V curves, for irradiances higher than 100 W m ⁻²	22
3.11	Comparing the MPP points from PVsyst to the reconstructed MPP points for irradiances higher than 100 W m ⁻²	23
3.12	I-V curve matching on 11:00 (AM) on January 12th.	23
3.13	Operating points of a sample direct coupled system. Δ indicates the MPP as defined by PVsyst, \circ indicates the MPP found by MATLAB using the average V_{oc} and I_{sc} , and ∇ indicates the intersection of the I-V curves.	25
3.14	Power curve of a 6.6 MW _p solar power system showing curtailment. On the left, the inverter and maximum electrolyzer capacity are placed closely together.	25
5.1	Temperature and Irradiance Dependency.	31
5.2	Comparing V_{oc} and I_{sc} data from PVsyst and equations 5.2 and 5.3.	33
5.3	A simple cloud coverage simulation.	34
6.1	Electrolyzer CAPEX historical data and forecast until 2030, taken from [10].	36
6.2	Historical and forecast LCOE range for utility-scale PV plants [45].	37
6.3	IEA forecasting trends [103].	37
6.4	Historical data of CAPEX of car Li-ion battery systems, assumed to be comparable to batteries used in scenario 2 and 3 [75].	38

6.5	CAPEX of inverter stations, taken from [70]. In this report the bottom line will be used.	39
7.1	Hydrogen production using MPPT technology as in scenario 1 for one inverter, with a red dot showing the optimum number of panels.	41
7.2	Costs for hydrogen production for scenario 1 over the entire system lifetime for one inverter, with the optimum configuration given by the red dot.	42
7.3	Power production from the solar farm using MPPT technology as in scenario 1 for one inverter, with a red dot showing the optimum number of panels.	42
7.4	Hydrogen production using MPPT technology as in scenario 2 for one inverter, with a red dot showing the optimum number of panels.	43
7.5	Costs for hydrogen production for scenario 2 over the entire system lifetime for one inverter, with the optimum configuration given by the red dot.	44
7.6	Power production from the solar farm using MPPT technology as in scenario 2 for one inverter, with a red dot showing the optimum number of panels.	44
7.7	Price of hydrogen dependence on battery capacity.	45
7.8	Hydrogen production using MPPT technology as in scenario 3 for one busbar, with a red dot showing the optimum number of panels.	46
7.9	Costs for hydrogen production for scenario 3 over the entire system lifetime for one busbar, with the optimum configuration given by the red dot.	46
7.10	Power production from the solar farm using MPPT technology as in scenario 3 for one busbar, with a red dot showing the optimum number of panels.	47
7.11	Hydrogen cost comparison.	47
7.12	OPEX breakdown.	48
7.13	MPP optimum layout, with maximum cable specifications given in the yellow text boxes.	49
7.14	DC optimum layout, with maximum cable specifications given in the yellow text boxes.	50
7.15	Decentralized DC optimum layout.	53
7.16	Hydrogen cost comparison (including decentralized DC).	54
7.17	OPEX breakdown (including decentralized DC).	54
7.18	Specific energy demand comparison.	55
7.19	Comparison of lifetime hydrogen production per W_p of solar power installed.	55
7.20	Comparison of usable solar energy generated per W_p installed.	56
7.21	Sensitivity analysis with the WACC at 0.5 and 0.9 (default 0.7), and the PV, electrolyzer, inverter and battery prices varied from 90% to 110% of the current values.	57
7.22	Voltage changes due to changing environmental conditions on a minute time scale.	58
7.23	Voltage changes due to changing environmental conditions on a minute time scale.	59
A.1	Characteristic I-V and P-V curves of Tallmax modules, taken from [95].	73

List of Tables

2.1	Typical electrolyzer parameters to be used in the electrolyzer model, adapted from [54].	8
2.2	Electrolyzer utility costs overview for DC scenario	10
2.3	Electrolyzer degradation and lifetime data, partially taken from [79].	11
2.4	Translated electrolyzer degradation values.	11
4.1	An overview of the battery characteristics used.	28
7.1	Optimal plot layout and corresponding H ₂ cost.	48
7.2	Overview of total in-field piping specifications.	51
7.3	Overview of header piping specifications.	51
7.4	Piping CAPEX overview.	52
7.5	Decentralized DC piping CAPEX.	52
7.6	Overview of the ramping results	59
A.1	Module parameters for the Tallmax modules, taken from [95].	73

Chapter 1

Introduction

With the political and energy systems of the world turning to a more sustainable and carbon dioxide (CO₂) neutral future, it is important to find technology to decrease our dependence on fossil fuels. There is an increasing need worldwide for (dense) energy carriers, and many look to hydrogen to fill the void left by society's turn from fossil fuels to intermittent renewable energy sources [109]. Shell hopes to develop technology that can be used worldwide to develop and sustain energy supply chains and believes that after 2040 hydrogen will emerge as a material energy carrier, steadily growing to account of 10% of the global energy consumption by 2100. Looking closer to the present, Japan aims to develop commercial-scale supply chains by 2030 to procure 300,000 tons of hydrogen per year and in the future this is expected to increase even further to 5-10 million tons per year [69]. In order to reach this goal, Shell is currently looking to establish a value chain between Australia, a very (solar) energy rich environment, and Japan, an energy short environment.

By combining a large PV system with a number of large electrolyzers it is possible to produce "green" (sustainable) hydrogen without producing any greenhouse gases. To facilitate this, Shell aims to develop a large solar and electrolysis based hydrogen production facility in Australia that will produce 80-100 tons H₂ per day in Broome, Australia. This location has been chosen because it receives a high amount of solar irradiance each year, and it is close to a number of other parties that would be interested in using green hydrogen.

This report aims to scope out a small pilot plant to be placed in Broome, Australia to test the possible technologies that will be used in the full-scale plant and to get a better grip on the technological difficulties that these projects will face. Building a small pilot plant allows insight to be gained into which technologies should be derisked and further developed before being implemented on a large scale.

1.1 Electrolyzers

In 2014 approximately 4% of global hydrogen production was supplied via electrolysis [11]. This number has not increased much since then, and of all the commercial hydrogen production taking place only 2-6% is powered by renewable energy [12, 34]. The rest of the energy is derived from fossil fuels. In order for hydrogen to be a truly sustainable energy carrier which can not only be used as a fuel but also to store energy, it must be generated through sustainable means.

Electrolyzers can produce hydrogen through electrolysis, a process in which an incoming feed of pure water is split into hydrogen (H₂) and oxygen (O₂). This is done by creating a potential difference between two electrodes in an electrolyte to separate water into its anionic (OH⁻) and cationic (H⁺) components. From this gaseous hydrogen and oxygen is produced.

There are currently two different types of electrolyzers readily available on the market; polymer (or proton) exchange membrane (PEM) electrolyzers and alkaline electrolyzers. These will both be elaborated on in chapter 2.

1.2 Photovoltaics

Photovoltaic (PV) technologies are playing an increasingly large role in the energy transition of humanity moving towards a greener future [96]. Currently, the total solar production worldwide only accounts for approximately 1% of the total primary energy supply worldwide [15, 77]. The conversion of solar irradiation into electricity by making use of the photovoltaic effect within semiconductor materials allows PV modules to produce electricity without emitting greenhouse gasses. When sufficiently energetic sunlight falls on a solar panel, a charge carrier pair, consisting of one electron and one "hole", is generated. These are then separated by a potential difference caused by the different doping types present in the silicon-rich wafer, and are then collected at the front and rear side. The electron then travels through an electric circuit and recombines with the hole at the other side. This is the basis of the photovoltaic effect [46].

The performance of a PV module depends on a number of factors such as the intensity of incident irradiation from the sun and on the module temperature. The PV module temperature can affect module characteristics and by extension the electrical properties observed in the module. PV modules are always tested under standard testing conditions (STC), meaning that the module is illuminated by 1000 W m^{-2} according to the AM1.5 spectrum irradiance normal to the panel at a module temperature of 25°C . This makes it possible to compare the performance and other parameters of different types of modules.

1.3 System components

Most PV systems require electronic system components which perform various actions such as maximum power point tracking, voltage regulation, limiting the battery's depth of discharge, and power conversion. Without these functionalities PV systems would not perform as well as they do. In most systems maximum power point trackers ensure that PV arrays always operate near their maximum power point, resulting in a higher solar panel efficiency. Inverters then convert the generated power from DC into AC power to allow the power to either be fed into the grid or to power an AC load.

In the future PV technologies will most likely be heavily incorporated into the existing grid, meaning storage will also play a crucial role in maintaining grid stability. The intermittency of PV systems will cause large fluctuations throughout the grid, which could be resolved by using batteries. Charge controllers are required to ensure that batteries are charged and discharged at optimal speeds and to prevent overloading or too much discharge. Operating outside the battery's operating conditions can cause irreversible damage. If batteries are installed in a very humid or warm place this could cause the lifetime of the battery cells to decrease further.

1.4 Scenarios

There are a number of ways to connect an electrolyzer and PV systems; this report will look at three different connection methods. Scenarios one and two use maximum power point tracking (MPPT) technology, meaning that if the PV system produces too much power it will be curtailed. Scenario two adds a battery and charge controller to the MPPT setup from scenario one. Finally, the third scenario will look at the direct coupling method, which removes a large part of the system components. The three scenarios are shown below in figure 1.1. More information on MPPT can be found in chapter 3.

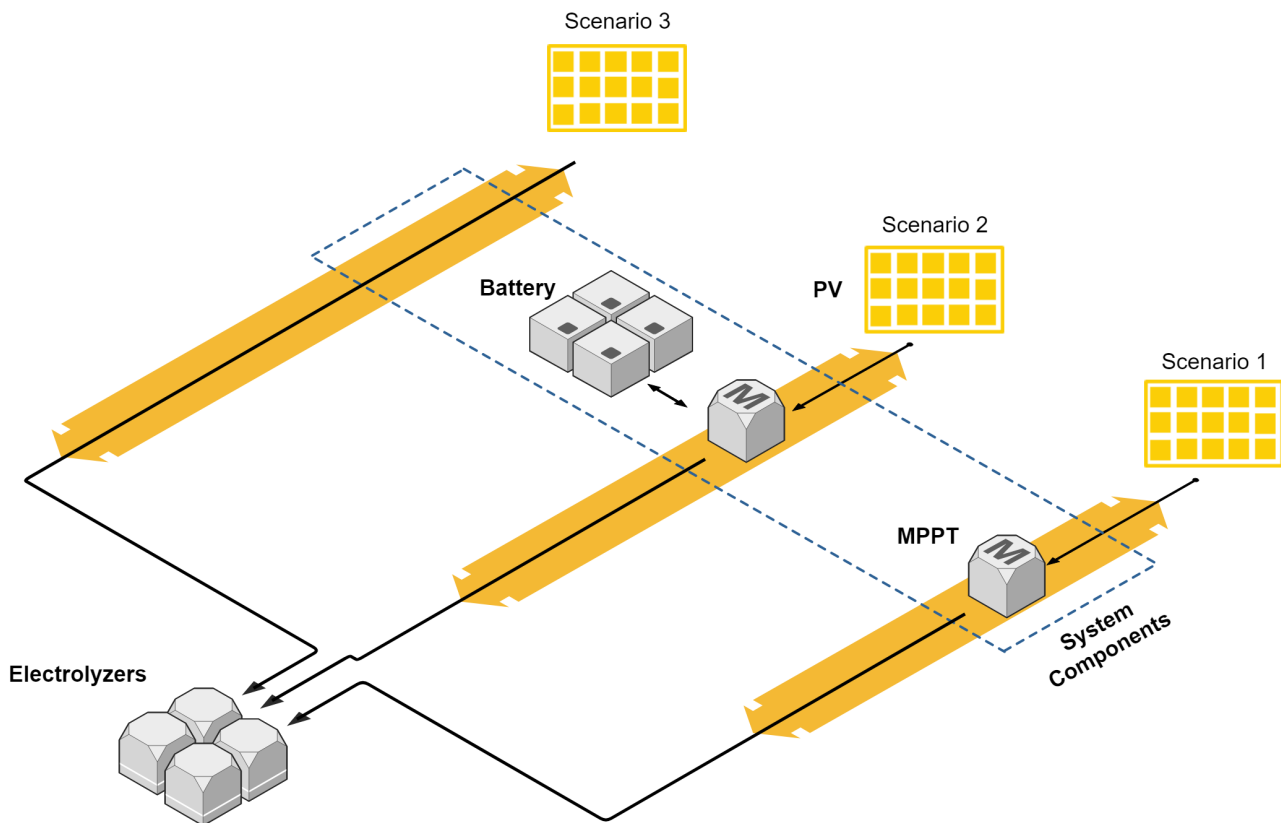


Figure 1.1: A schematic of the different topologies possible.

The direct coupling method operates the PV system at the point defined by the intersection of the I-V curves of the PV system and the electrolyzer system. An absence of many of the system components will cause a large decrease in investment (CAPEX) and operation/maintenance (OPEX) costs, although it will cause the overall performance of the system to decrease by not using the maximum PV power. In previous research it is estimated that the decrease in CAPEX will be approximately 700 USD kW^{-1} , or 3.5-6%, showing that the DC scenario has a potentially large advantage over the MPP scenarios [80, 81].

This report aims to assess the feasibility of building a solar and electrolysis plant in Broome, using the three different topologies discussed above; one scenario with normal MPPT technology, one scenario with MPPT technology and electricity storage, and finally one scenario with a direct coupling interlink. This will be done by first designing the required electrolyzer and PV models in chapter 2 and 3 respectively. Then, the tools to analyze the data generated from the models will be described in chapter 5. In chapter 6 an economic evaluation framework will be constructed to process the data from the previous chapters. The results will be given and discussed in chapter 7, after which conclusions will be drawn in chapter 8.

Chapter 2

Electrolyzers

An electrolyzer stack is made up of multiple cells coupled in series. An electrolyzer system, commonly referred to as an electrolyzer, is a system of multiple stacks incorporated into one large system. Each cell has a voltage between 1.48 V and 2.15 V, while the maximum current and number of cells in series depends on the size of the electrolyzer. In this report a Hydrogenics 48 kW unit will be used, shown below in figure 2.1.

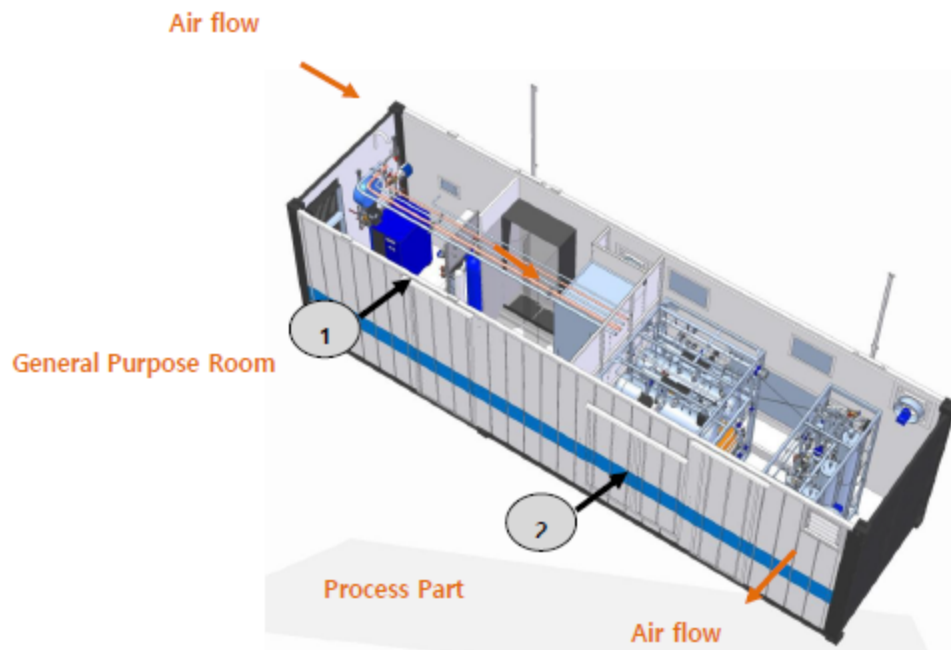


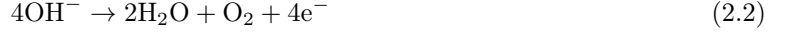
Figure 2.1: A Hydrogenics alkaline electrolyzer [44].

This electrolyzer has been modelled because there was actual experimental data available. The equations and procedures that follow can be altered to use different electrolyzers. Additionally, the optimization model determines the optimum topology of the electrolyzer system by placing a number of electrolyzers in series and in parallel, essentially simulating a larger electrolyzer.

At the cathode in an alkaline electrolyzer hydrogen is produced from pure water via the following reduction reaction [31]:



At the anode, a highly oxidizing environment, the following oxidation reaction takes place:



A schematic of an alkaline electrolyzer is shown below:

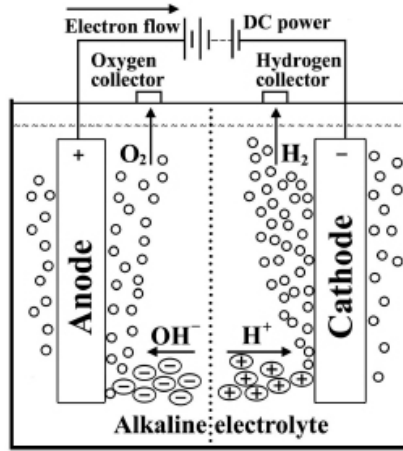


Figure 2.2: The basis of alkaline electrolysis [91].

There are many factors that influence the performance of an alkaline electrolyzer, such as voltage, current, pressure, electrode spacing, electrolyte temperature, and electrolyte concentration [7, 25]. However, these will not be investigated in this report as we are not looking in to the fundamentals of electrolyzers; instead, this report will look at how existing electrolyzers perform within the systems described in chapter 1. The electrolyzer degradation will be taken into account in section 2.3, which will be looked at in conjunction with electrolyzer lifetimes. This report focuses mostly on alkaline electrolyzers as the capabilities of PEM electrolyzers are well documented compared to alkaline electrolyzers, and because PEM electrolyzers have already been (experimentally) investigated in such a system [80]. The equations that follow hereafter could easily be adjusted to model a PEM electrolyzer, just as the upper and lower operational bounds could be adjusted. An integrated solar and electrolysis unit, in which sunlight is directly used to split water into oxygen and hydrogen, is not considered due to the current limitations in scale-up. This system uses direct photochemical conversion to absorb the incoming radiation and split water [14, 23]. This technology is still in a very early phase and it is expected that it will take a number of years before this is competitive with other technologies on such a scale.

The electrolyte usually consists of a 25-30 % aqueous KOH solution. Alkaline electrolyzers produce hydrogen between 40-100% of their maximum capacity and, combined with after-treatment such as driers or scrubbers, can result in a hydrogen purity of up to 99.99999% [18]. Hydrogen has a higher heating value (HHV) of $142.80 \text{ MJ kg}^{-1}$, or $39.38 \text{ kWh kg}^{-1}$, meaning that 39.38 kWh is needed to produce 1 kg of hydrogen at $25 \text{ }^\circ\text{C}$ and 1 bar from pure liquid water [80]. This results in a minimum thermoneutral cell voltage of 1.48 V , according to the following formula:

$$V_{\text{thermoneutral}} = \frac{\Delta H}{zF} \quad (2.3)$$

with ΔH the enthalpy change which is equal to $285.83 \text{ kJ mol}^{-1}$, z the amount of electrons released (2 in this case) and F the Faraday constant. This equation is highly temperature dependent, as each of the parameters above changes with temperature. Furthermore, we can rewrite ΔH as:

$$\Delta H = \Delta G + T\Delta S \quad (2.4)$$

with ΔG the Gibbs free energy which indicates the amount of energy required for the reaction to take place assuming no energy is needed to heat the material up, ΔS the entropy change which is equal to 163.3 J mol^{-1} , and T the electrolyzer temperature. To simplify this, ΔH is usually referred to as the

total energy for electrolysis, ΔG the electrical energy required and $T\Delta S$ the heat energy required. If there is an external heat source available, only ΔG needs to be taken into account:

$$V_{\text{rev}} = \frac{\Delta G}{zF} \quad (2.5)$$

This results in a minimum reversible cell voltage of 1.23 V [59]. The thermoneutral and reversible voltages are shown below in figure 2.3.

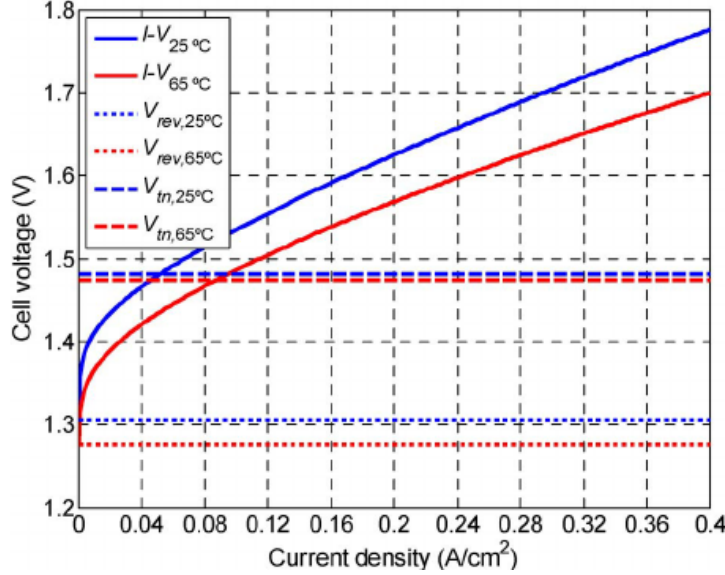


Figure 2.3: Characteristic I-V curves for electrolyzers at 25°C and 65°C and 20 bar [98].

The amount of gas produced by an electrolyzer is frequently expressed in Nm^3 , otherwise known as a normal cubic meter. This represents the volume a gas would occupy at 0°C, 101.3 kPa, and 0% humidity. One kilogram of hydrogen equates to 11.121 Nm^3 .

The efficiency of an electrolyzer cell can furthermore be expressed as:

$$\eta_{EZ} = \frac{1.48 \text{ V}}{V} \quad (2.6)$$

with V the voltage applied across the cell. Typically around 1.6-2V are applied to a cell, meaning that the efficiency varies from 70-90% depending on the voltage.

The Faradaic efficiency η_f , sometimes also called the current efficiency, gives how much of the current within the cell is used to produce hydrogen and is frequently reported as being close to unity in the range we are operating the electrolyzer [97, 108]. Therefore, it is assumed that the alkaline electrolyzer in question has a Faraday efficiency of 100%.

2.1 Electrolyzer Model

There are many different (complex) models for electrolyzers, such as [32, 33, 55] for PEM electrolyzers and [2, 17, 55] for alkaline electrolyzers. A more simple yet effective empirical model, based on work by Ulleberg, is given by Khalilnejad and Riahy as the following [54]:

$$V = V_{\text{rev}} + \frac{r_1 + r_2}{A} I + s \log \left(\frac{t_1 + t_2/T + t_3/T^2}{A} I + 1 \right) \quad (2.7)$$

with V_{rev} the minimum reversible cell voltage, r_1 and r_2 the cathodic and anodic ohmic losses, t_1 , t_2 , t_3 and s the overvoltage temperature coefficients, T the temperature of the electrolyzer and A the area of the electrolyzer [97]. Typical values are given below in table 2.1.

Table 2.1: Typical electrolyzer parameters to be used in the electrolyzer model, adapted from [54].

r_1	$7.3 \cdot 10^5 \Omega m^2$	t_3	$247.3 A^{-1} m^2 C^2$
r_2	$-1.1 \cdot 10^{-7} \Omega m^2 C^{-1}$	s	$1.6 \cdot 10^{-1} V$
t_1	$-1.002 A^{-1} m^2$	A	$0.16 m^2$
t_2	$8.424 A^{-1} m^2 C$		

Using these parameters an approximation can be made for the I-V characteristic of the electrolyzer, as shown below in figure 2.4.

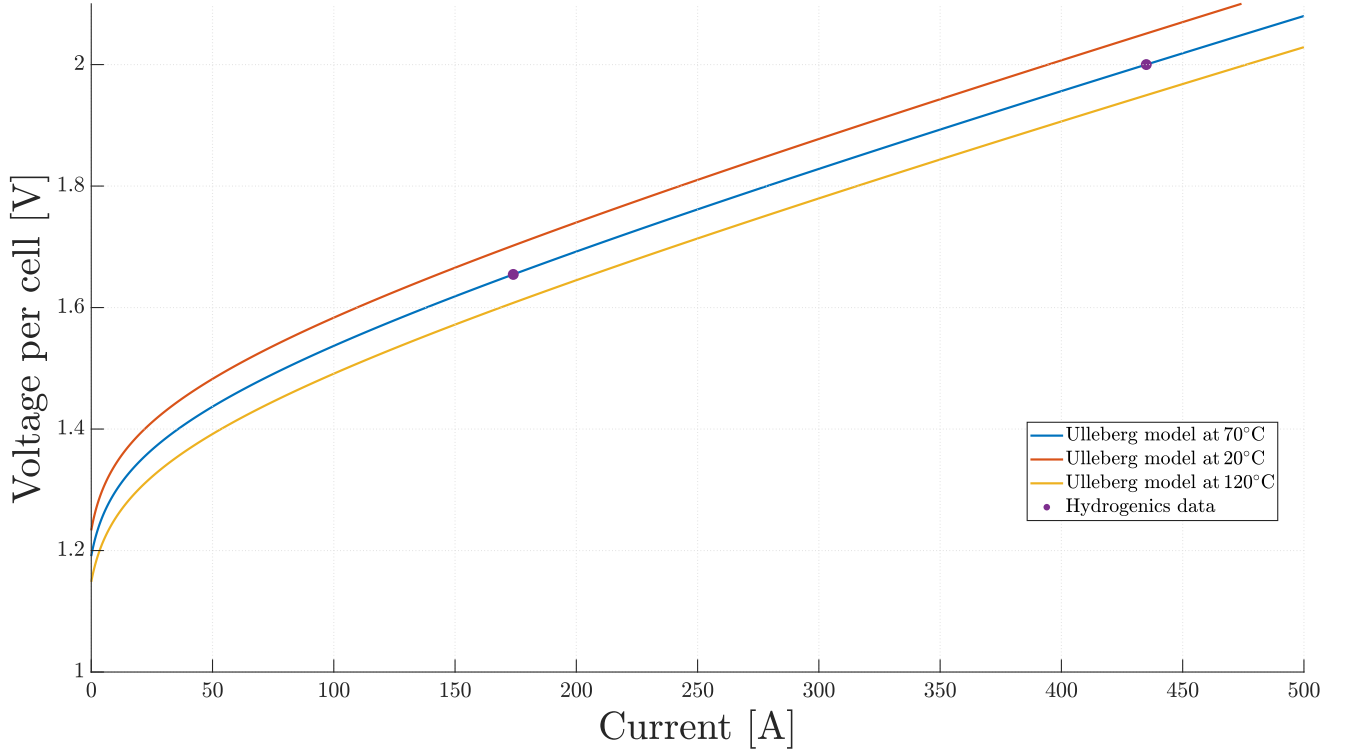


Figure 2.4: An example I-V curve for an alkaline electrolyzer, using data from [54] and operating points from [44].

An alkaline electrolyzer operates between 40% to 100% of its maximum load. Using data from [44] we can fit the model to their operating points, given that the electrolyzer they produce operates at 70°C. We see that between these points, the relationship is almost linear. Thus, the electrolyzer can further be simplified within this region to:

$$I = A \cdot V + C \quad (2.8)$$

with $A = 12.6 A V^{-1}$ and $C = -964.6 A$ at 70°C. Electrolyzers only marginally cool off overnight [97], meaning that we could simplify this model even further by keeping A and C fixed. This fixed method will be used when each of the scenario's are calculated. For the ramping investigation, detailed in section 5.2, A and C will vary depending on the temperature.

The electrolyzer from [44] comes in a 20 foot container, which has a footprint of 6.1 m by 2.4 m. As the electrolyzer comes in the shipping container, it is protected from the environment, meaning no

additional buildings are necessary to protect them. The outfeed of the electrolyzer is hydrogen at 27 bar [44], and it requires an infeed of approximately 1 liter of pure demineralised water to produce 1 Nm³ of hydrogen. This will later be addressed in section 6.5.

2.2 Utility energy costs

To go from a single cell to a stack of 60 cells which are all connected in series for the Hydrogenics electrolyzer, the voltage multiplies according to the number of cells present in a stack. Furthermore, electricity is not only required for the production of hydrogen but also to run pumps and other system processes. It is reasonable to assume that per normal cubic meter (Nm⁻³) hydrogen produced, 0.5 kWh is required to account for these losses and discrepancies between cell voltage and system voltage [64]. This difference E_u is attributed to utility costs and stack losses. Translated to kWh kg⁻¹, this means that 5.61 kWh per kg hydrogen is required. In scenario's 1 and 2 (1: MPP and 2: MPP combined with a battery) this can be added to the total energy demand of hydrogen conversion. To convert water to hydrogen 39.38 kWh kg⁻¹ is required when 1.48 V is applied to a cell. Adding the utility costs, this is increased to 44.99 kWh kg⁻¹. If the voltage changes this also changes the energy requirement to produce hydrogen, according to a linear relationship [35]:

$$E(V) = \frac{E(1.48)}{\eta_{EZ}} = E(1.48) \cdot \frac{V}{1.48} \quad (2.9)$$

with V the voltage per cell. Using this, it is possible to predict how much hydrogen will be produced per hour (H) per stack:

$$H = \frac{P}{E(V) + E_u} \eta_f n_{\text{cells}} = \frac{V \cdot I}{E(V) + E_u} \eta_f n_{\text{cells}} = \frac{V(A \cdot V + C)}{E(1.48) \cdot \frac{V}{1.48} + E_u} n_{\text{cells}} \quad (2.10)$$

This is shown below in figure 2.5.

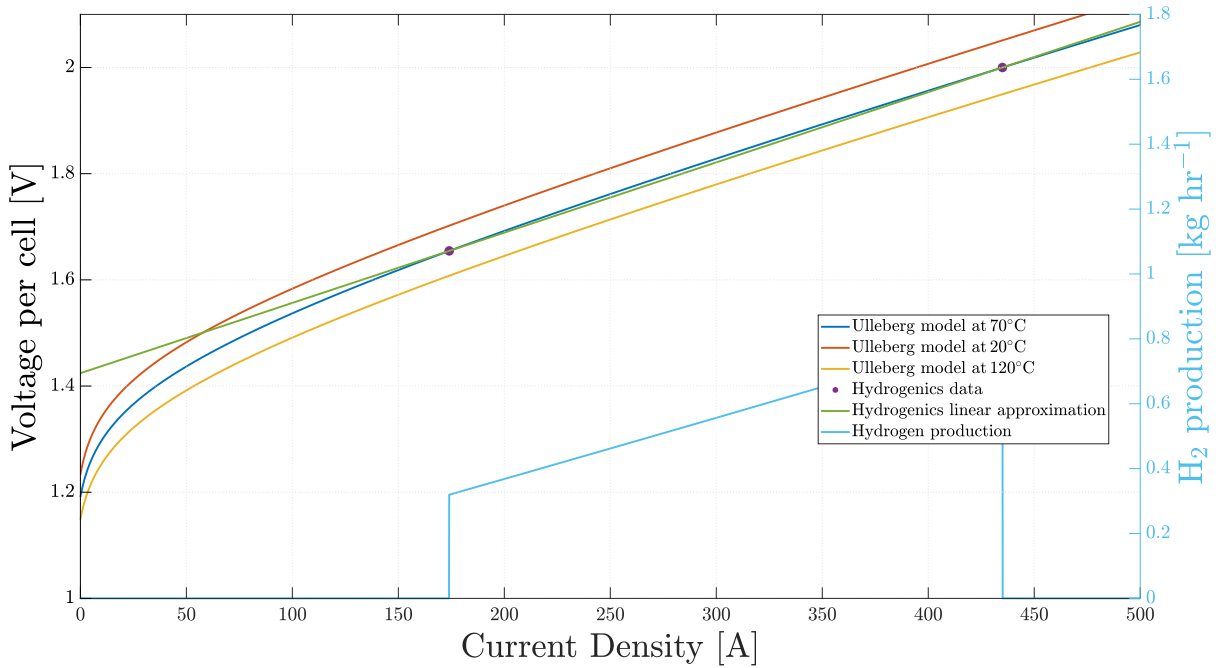


Figure 2.5: Hydrogen production from a single cell.

In scenario 3 the PV and electrolyzer are directly coupled to each other. This means that there is no control over the incoming energy to power the utilities. Therefore a separate, smaller, PV system must

be designed to operate the stack utilities. We should also include a small battery to store 2 hours worth of energy, to guarantee operation of start up and shutdown mechanisms within the electrolyzers. If the goal is to produce 3 tons of hydrogen per day and assuming that there is at least 12 hours between sunrise and sunset, then this means that on average 0.25 tons of hydrogen are produced each hour. In reality, most of this is produced around noon while at the beginning and end of the day less hydrogen is produced. We may therefore be overestimating the required battery capacity, although this would allow for the system to shutdown at almost any time. The total storage should therefore be, using a utility cost of 5.61 kWh per kg, 2805 kWh per day for all electrolyzers combined.

The average specific energy demand from early tests is found to be on approximately 52.5 kWh per kg, excluding utility costs. The utility energy requirement is 5.61 kWh per kg, plus an additional 2805 kWh per day or 935 Wh per kg to charge the batteries every day. This totals to an average of 6.55 kWh per kg hydrogen. The ratios of the panels should be equal to the ratios of the energy requirements, meaning that for every 1000 panels for hydrogen production, 125 extra panels are required to run utilities.

In the DC scenario this ratio will further increase, as the intersection point of the electrolyzer is to the left of the MPP, resulting in a lower voltage and thus decreasing the specific energy required to produce 1 kg of hydrogen. Taking into account an additional safety margin, we can safely assume that for every 1000 panels, 150 extra panels should be included to just run the electrolyzer utilities and charge the utility battery. We additionally know that the goal is to produce 3 tons of hydrogen a day and using meteorological data from Broome an average equivalent sun hours (ESH) of 8.4 hours was found. This means that approximately 3.5 MW_p of solar power is needed in total for utilities, or 10,000 panels. An overview of all these parameters is given below in table 2.2.

Table 2.2: Electrolyzer utility costs overview for DC scenario

Property	
Battery capacity	2805 kWh
Utility energy cost	5.61 kWh kg ⁻¹
Panel ratio	125:1000
Total number of panels	~ 10,000

2.3 Electrolyzer degradation and lifetime

Just like the PV modules, the electrolyzers will also degrade over time. How much it will degrade is heavily dependent on the temperature and pressure at the catalyst, electrolyte and membrane [79]. Electrolyzer stacks do not often fail catastrophically, such that from one moment to the next their output is greatly decreased. Instead, as the cell ages, various degradation processes take place in the catalyst, membrane and electrolyte. These lead to a higher internal cell resistance resulting in an increase of overpotential that must be applied to produce the same amount of hydrogen [10]. It is assumed that the faradaic efficiency remains constant. In reality, this will also degrade slightly.

It is thus important to define when an electrolyzer has reached the end of its life. If the degradation is approximately 5 $\mu\text{V h}^{-1}$ and a typical lifetime of 60,000 hours is used, then the efficiency has fallen by approximately 10% by the end of its life. This is frequently taken as a typical "end of life" threshold, which can further be assumed to be a linear decay [10]. Leading manufacturers of PEM and alkaline cells state that the lifetime of these electrolyzer stacks is approximately 60,000 to 90,000 hours. It is worth mentioning here that there is very limited data available on long-term electrolyzer degradation powered by intermittent renewable energy, making it difficult to verify this statement. An operating lifetime of 90,000 hours translates to approximately 10 years of continuous operation.

Barbir claims a higher initial degradation of 20 to 50 $\mu\text{V h}^{-1}$ for the first few hours of operation, after which it levels off to degradation below 3 $\mu\text{V h}^{-1}$. For state of the art electrolyzer systems under continuous operation, degradation values of as low as 0.4 to 5 μV per operating hour have been reported [10]. Many papers however find the electrolyzer average degradation to be higher [8, 79].

The following values given in table 2.3 will be used in the calculations to find the price of the hydrogen produced by each of the different scenarios. These values are primarily based off of the paper by Parra and Patel, although the alkaline degradation has been increased to $3 \mu\text{V h}^{-1}$ as given by Bertuccioli et al..

Table 2.3: Electrolyzer degradation and lifetime data, partially taken from [79].

		PEM	Alkaline
Lifetime	[h]	50,000	90,000
Degradation	$[\mu\text{V h}^{-1}]$	5	3

The degradation in the aforementioned papers is for an electrolyzer with continuous usage. In the case of an electrolyzer being powered by solar energy which is inherently intermittent, there will be some intermittency in the power profile. It has been shown by Rakousky et al. that periods of non-operation, or relaxation with lower current densities may help reduce the degradation of the unit by allowing the processes that contribute to reversible losses to relax and not progress to permanent losses [87]. It is however worth noting that the effect of variable generation or intermittent power profiles is not well documented. Furthermore, allowing the electrolyzer to operate below its minimum threshold for up to ten minutes would cause a decrease in stops by approximately 34.8% [99]. These factors will not be included in this report as it is not possible to verify that this also holds for alkaline electrolyzers. However, it is interesting to note that research has been done in these areas and these could be incorporated in future modelling work. The number of actual operating hours per year for an electrolyzer depends on the system topology, as there are moments when the PV system does not produce enough power to make the electrolyzer produce hydrogen. A simulation for an electrolyzer in Broome has been built, using the same solar data for 20 years. Assuming that the solar panels do not degrade because they are replaced (costs included in PV OPEX), the electrolyzers are found to run approximately 4000 hours per year. This is less than half of what it would operate if they were to run continuously.

In order to relate the degradation in $\mu\text{V h}^{-1}$ to degradation in % of output H_2 per year, a number of assumptions must be made. Assuming that the faradaic efficiency is unity, the relationship is indeed linear between electrolyzer current and voltage, and assuming that the reversible voltage does not change, it is possible to find the degradation in % of output H_2 per year [35]. Namely, taking the reversible voltage as fixed and shifting the operating point of the Hydrogenics electrolyzer (right most point) up according to the degradation data from table 2.3 a new linear profile can be found. The difference in current for the same voltage then gives the degradation in percentage of kWh per kg H_2 , as the current and power requirements are linearly related. The new degradation values can be found in table 2.4 and the degradation itself is shown in figure 2.6.

Table 2.4: Translated electrolyzer degradation values.

Year	H_2 output loss [%]
0	0
5	2.7
10	5.6
15	8.3
20	10.9

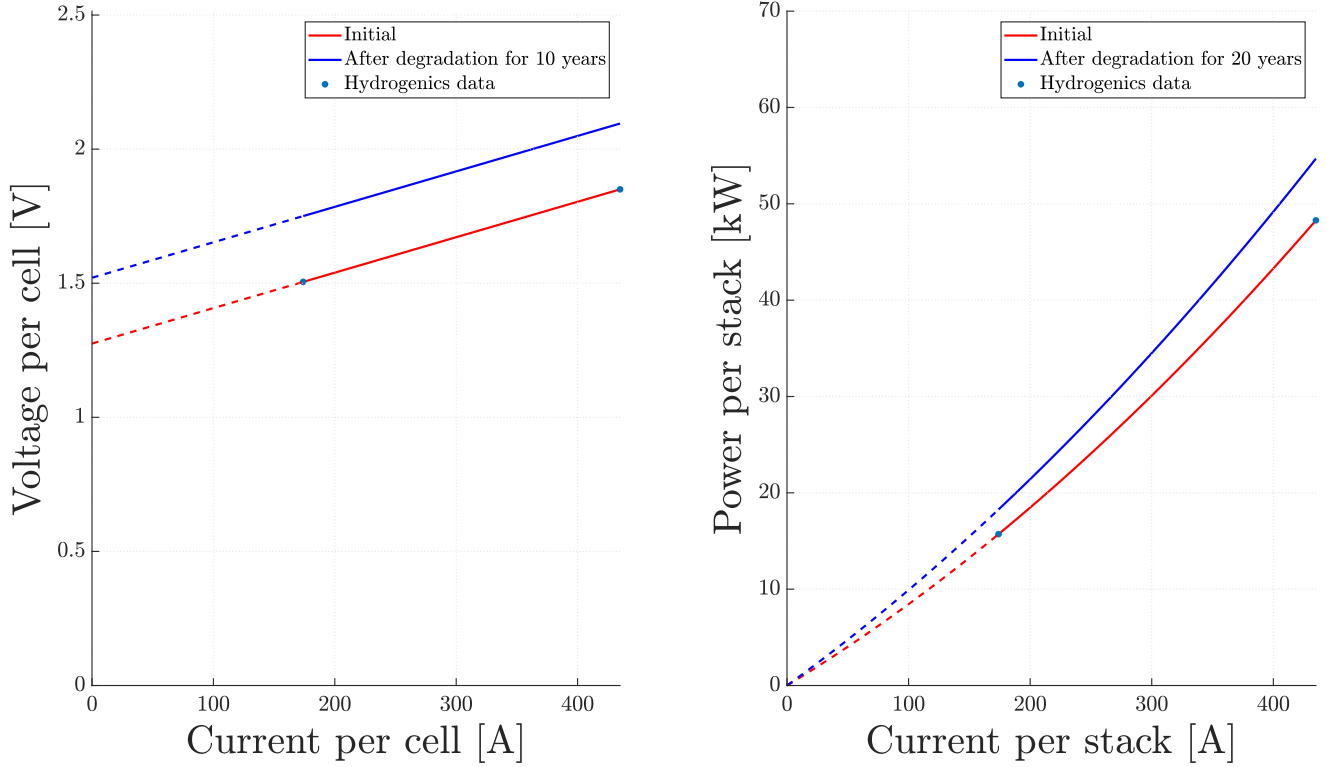


Figure 2.6: Electrolyzer degradation after a lifetime of 20 years (intermittent usage).

After 20 years the electrolyzers have run for approximately 81,500 hours, meaning an availability of 46%. A maximum lifetime of 90,000 hours was initially referred to as being the lifetime of a continuously operated alkaline electrolyzer. As the electrolyzers used in this simulation are run intermittently, it can be assumed that these will have a shorter lifetime. The lifetime will therefore be taken as 20 years.

After 20 years the total amount of hydrogen produced over the entire lifetime of the electrolyzer is found to be 5.73% less if degradation is taken into account.

Initially the degradation causes the specific energy demand to increase to produce hydrogen. However, the maximum production rate of hydrogen does not change because the current is not limited. Any change in hydrogen production is due to the increased specific energy demand to produce one kilogram of hydrogen. After the voltage reaches above 2.15 V per cell however, the current is limited so that the voltage does not exceed 2.15 V. At this moment an electrolyzer has reached the end of its life and the current is not allowed to increase beyond the point at which the voltage is equal to 2.15 V.

Chapter 3

PV Systems

A silicon PV cell typically generates around 0.6 V at open circuit conditions and 9.6 A at short circuit conditions. Between these two values the I-V curve for a cell usually looks something like what is shown in figure 3.1. The maximum power point (MPP) is defined by the point where the panel generates its maximum power. At the MPP, the voltage and current are said to be equal to V_{mpp} and I_{mpp} respectively. A panel is operated close to its MPP through maximum power point tracking (MPPT), using methods such as perturb and observe, linear approximation methods (such as fractional V_{oc} or I_{sc} methods) or by using a small test cell [47]. Of these different techniques, the perturb and observe (P&O) method is most frequently implemented due to its simplicity and low cost compared to the increase in generation. However, this algorithm is not good at distinguishing local power maximums from the global maximum, and can be slow when the incident irradiance changes rapidly [90].

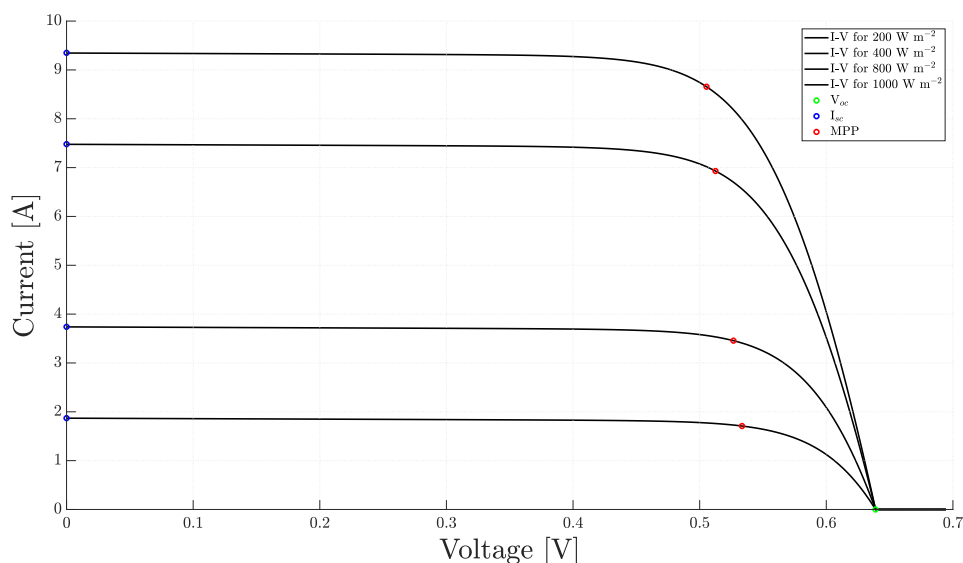


Figure 3.1: An example I-V curve for a typical PV cell.

Full size panels are usually made of 60 or 72 cells in series. In this report the term "module" and "panel" have no distinction, and multiple connected panels will be called an array. A string is an array of modules which are only connected in series. A module of 60 cells is typically split into 3 strings of 20 cells each, with each string connected in series to the others while a bypass diode is connected in parallel. This bypass diode allows current to pass when the module is partially shaded, preventing large losses. All of the cells are connected in series to produce a higher voltage and a low current. This is preferred as the resistance through wiring is quadratically dependent on the current running through it. When a string of 20 cells is shaded, the power produced in that string is limited, depending on how opaque the shading is. If the cells receive absolutely no light then the total module power will decrease

by a third. Because a bypass diode is connected per 20 cells, the cell with the lowest performance determines the power production for the other 19 cells within that string. Partial shading can cause multiple maximum power points to form, making MPPT difficult and causing further losses.

The output of a panel can be increased in shaded conditions by implementing more bypass diodes. Although bypass diodes are generally not expensive, implementing more bypass diodes would require producers to change the layout of the panel and hence this tactic is usually averted. Hence, it is very important to avoid shading if possible, and otherwise minimize shading as much as possible.

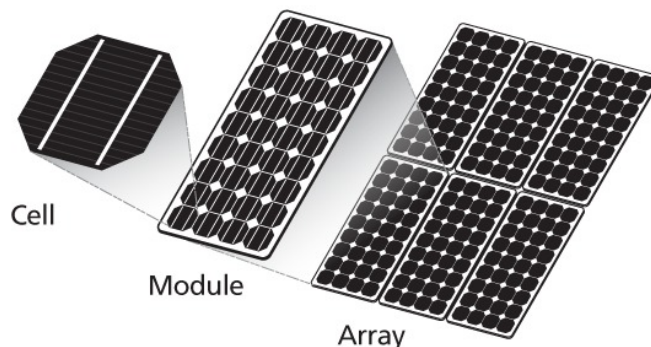


Figure 3.2: An overview of terms frequently used to describe PV systems, taken from [89].

Information specific to the Tallmax PV modules that will be used in this model can be found in table A.1 in appendix A.

There are multiple ways to model and simulate PV systems. Some allow the user to build the model from the ground up and some provide tools to quickly produce detailed simulations. Programs like MATLAB, QUCS and LTspice have predefined components allowing equivalent electrical circuits to be built [62, 65, 85]. However, these programs do not lend themselves well to modelling the behaviour of the power optimizers, micro-inverters and central inverters as these must be built from the ground up. Additionally, more basic programs like Excel are not suited due to the difficulty in finding solutions through iteration and will therefore not be used to model the complex system proposed.

PV*SOL, PVsyst and SAM are powerful tools which can combine meteorological data, 3D system designs and solar positions throughout the year, to provide a detailed analysis of systems [74, 84, 100]. PV*SOL and SAM are both comparable to PVsyst, and it has been stated that PV*SOL is almost just as accurate as PVsyst and calculates shading on a panel level, just like PVsyst [5, 30, 36, 63]. The accuracy of PVsyst has also been demonstrated before [30, 41, 60, 63, 92, 102]. However, PVsyst provides a more detailed breakdown of the different losses within a system, and is already being implemented within Shell [107]. Furthermore, SAM is still a relatively new modelling program, and can only model the PV side of the system while PVsyst can also model inverters. Therefore, PVsyst will be implemented instead of PV*SOL or SAM. It is furthermore assumed that the amount of panels (and electrolyzers) in series or parallel have a linear relationship with the total system voltage and current respectively.

PV panels degrade throughout their life. Many manufacturers give warranties up to 30 years, although not much is currently known about the performance of solar panels after their warranty has expired, as there have not been many large scale tests for such a long period of time. Typically, degradation rates of 0.5% to 1.5% are seen per year [51]. In this report the operational expenditure (OPEX) also includes the replacing of panels, such that degradation can be ignored.

If MPPT is used then the maximum output power of the PV system is transformed to lie on the electrolyzer's I-V curve. In the case that a battery is also added, then the battery will absorb excess power from the PV system when the electrolyzer cannot handle it, and supplement the PV system's output when it is operating below the minimum electrolyzer threshold to produce hydrogen. In order to be able to operate the electrolyzer during the night a lot of energy must be stored and hence the PV system should ideally be oversized. In the case of direct coupling the operating point can be found through the process described in section 3.4. Due to mismatching the DC system will also likely be

larger than the MPP system from scenario 1. It is thus reasonable to assume that the PV system size will decrease as we move from scenario 2 (MPPT with battery) to scenario 3 (direct coupling) to scenario 1 (MPPT).

The data used to simulate scenario 1 and 2 is produced using a test PVsyst installation located in Broome, Australia. This data is then transformed to the current system being tested, and in the case of scenario 2 a battery system is added. This is done by storing energy when the PV system produces more energy than the inverter or electrolyzer system can handle, and by withdrawing energy when there is energy available and when the electrolyzers need it. In order to use the data for scenario 3, a more comprehensive analysis must be implemented as the I-V curves need to be utilized. This will be shown later in section 3.4.

3.1 The One Diode Model

PVsyst (version 6.67) is a powerful tool which not only model PV modules but also use inverter characteristics, meteorological data, 3D sketches and solar positions throughout the year, to provide a detailed analysis of any system [84]. Shading is done on a panel level as opposed to a cell or bypass diode string level, as there is only a small difference in accuracy [63]. PVsyst uses the one diode model to simulate a solar cell, shown below in figure 3.3 [66].

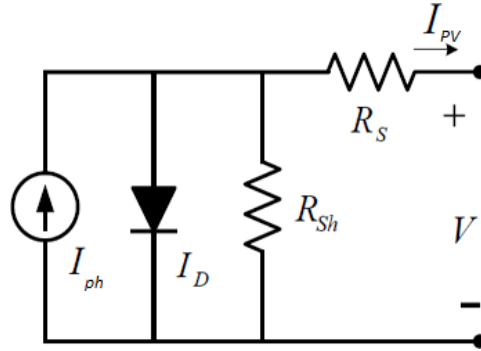


Figure 3.3: A schematic of the one diode model, adapted from [86].

In this model the current produced by the solar cell is the superposition of the dark current through the diode and the current generated in the solar cell due to the illumination (represented by a current source) [93]. Using Kirchoff's current law, the following can be stated:

$$I_{PV} = I_{ph} - I_D - I_{sh} \quad (3.1)$$

Here I_{ph} represents the current produced by the cell as a response to the light shining on it, I_D the current through the diode, I_{sh} the current through the shunt resistance R_p (called R_{sh} in figure 3.3), and I_{PV} the cell output current in the external circuit. Furthermore, the thermic voltage $V_t(T)$, open circuit voltage $V_{oc}(T)$, photocurrent $I_{ph}(G, T)$ and loss current $I_{sh}(G, T)$ are given by the following relationships [106]:

$$V_t(T) = \frac{Ak_B T}{q} \quad (3.2)$$

$$V_{oc}(T) = V_{oc,STC}(1 + K_v \Delta T) \quad (3.3)$$

$$I_{ph}(G, T) = I_{sc,STC}(1 + K_i \Delta T) \frac{G}{G_{STC}} \quad (3.4)$$

$$I_{sh}(G, T) = \frac{V + IR_s}{R_p} \quad (3.5)$$

Here ΔT is the difference in operating temperature from the STC temperature, R_p the shunt (parallel) resistance, K_i and K_v the temperature coefficient of the short circuit current and open circuit voltage respectively, G and G_{STC} indicate the global irradiance at operating and STC conditions respectively, q the elementary charge (1.602×10^{-19} C), k_B the Boltzman constant (1.38×10^{-23} J K⁻¹), and A the diode ideality factor (DIF) which is usually between 1 and 2, depending on the type of the PV panel. The current through the diode can be described by the Shockley equation for an ideal diode [19]:

$$I_D(G, T) = I_{sat}(G, T) \left[e^{\frac{V+IR_s}{V_t(T)N_{cs}}} - 1 \right] \quad (3.6)$$

Here, I_{sat} is the diode saturation current, V the operating voltage of the cell, R_s the series resistance, N_{cs} the number of cells in series, and $V_t(T)$ the thermal junction constant which depends on the temperature. The saturation current can be expressed as [105]:

$$I_{sat} = I_o \left(\frac{T}{T_{STC}} \right)^3 e^{V_t(T) - V_t(T_{STC})} \quad (3.7)$$

At open circuit conditions we can find the value of I_o . Namely, at open circuit conditions equation 3.1 reduces to:

$$0 = I_{ph} - I_o \left(\frac{T}{T_{STC}} \right)^3 e^{V_t(T) - V_t(T_{STC})} \left[e^{\frac{V_{oc}}{V_t(T)N_{cs}}} - 1 \right] - \frac{V_{oc}}{R_p} \quad (3.8)$$

Rewriting this, we see that:

$$I_o = \frac{I_{ph} - \frac{V_{oc}}{R_p}}{\left[e^{\frac{V_{oc}}{V_t(T)N_{cs}}} - 1 \right] e^{V_t(T) - V_t(T_{STC})} \left(\frac{T}{T_{STC}} \right)^3} \quad (3.9)$$

These equations can be substituted into equation 3.7 to find the reverse saturation current I_{sat} :

$$I_{sat} = \frac{I_{ph} - \frac{V_{oc}}{R_p}}{\left[e^{\frac{V_{oc}}{V_t(T)N_{cs}}} - 1 \right] e^{V_t(T) - V_t(T_{STC})} \left(\frac{T}{T_{STC}} \right)^3} \left(\frac{T}{T_{STC}} \right)^3 e^{V_t(T) - V_t(T_{STC})} \quad (3.10)$$

$$I_{sat} = \frac{I_{ph} - \frac{V_{oc}}{R_p}}{e^{\frac{V_{oc}}{V_t(T)N_{cs}}} - 1} \quad (3.11)$$

This can be then be substituted in equation 3.1 to find the output panel current:

$$I_{PV} = I_{ph}(G, T) - I_{sat}(G, T) \left[e^{\frac{V+I_{PV}R_s}{V_t(T)N_{cs}}} - 1 \right] - \frac{V + I_{PV}R_s}{R_p} \quad (3.12)$$

$$I_{PV} = \left(I_{ph}(G, T) - \left[I_{ph}(G, T) - \frac{V_{oc}}{R_p} \right] \frac{e^{\frac{V+I_{PV}R_s}{V_t(T)N_{cs}}} - 1}{e^{\frac{V_{oc}}{V_t(T)N_{cs}}} - 1} - \frac{V}{R_p} \right) / \left(1 + \frac{R_s}{R_p} \right) \quad (3.13)$$

We see that this is an implicit equation and hence cannot be solved analytically. In order to find the current I_{PV} we must apply the Newton-Raphson iteration method iterate multiple times over this equation. Newton-Raphson finds the current I_{PV} as follows:

$$I_{PV,n+1} = I_{PV,n} - \frac{f(I_{PV,n})}{\frac{\partial f(I_{PV,n})}{\partial I_{PV}}} \quad (3.14)$$

with

$$f(I_{PV,n}) = I_{PV,n} - \left(I_{ph}(G, T) - I_{sat}(G, T) \left(e^{\frac{V + I_{PV,n} R_s}{V_t(T) N_{cs}} - 1} \right) - \frac{V}{R_p} \right) / \left(1 + \frac{R_s}{R_p} \right) \quad (3.15)$$

$$\frac{\partial f(I_{PV,n})}{\partial I_{PV,n}} = 1 - \left(-I_{sat}(G, T) \frac{R_s}{V_t N_{cs}} e^{\frac{V + I_{PV,n} R_s}{V_t(T) N_{cs}}} \right) / \left(1 + \frac{R_s}{R_p} \right) \quad (3.16)$$

The initial guess will neglect the current term in the exponent. This can then be expressed as:

$$I_{PV,0} = \left(I_{ph}(G, T) - \left[I_{ph}(G, T) - \frac{V_{oc}}{R_p} \right] \frac{e^{\frac{V}{V_t(T) N_{cs}} - 1}}{e^{\frac{V_{oc}}{V_t(T) N_{cs}} - 1}} - \frac{V}{R_p} \right) / \left(1 + \frac{R_s}{R_p} \right) \quad (3.17)$$

The shape of the I-V curve of the solar cell changes slightly with respect to the initial guess $I_{PV,0}$, as can be seen below in figure 3.4.

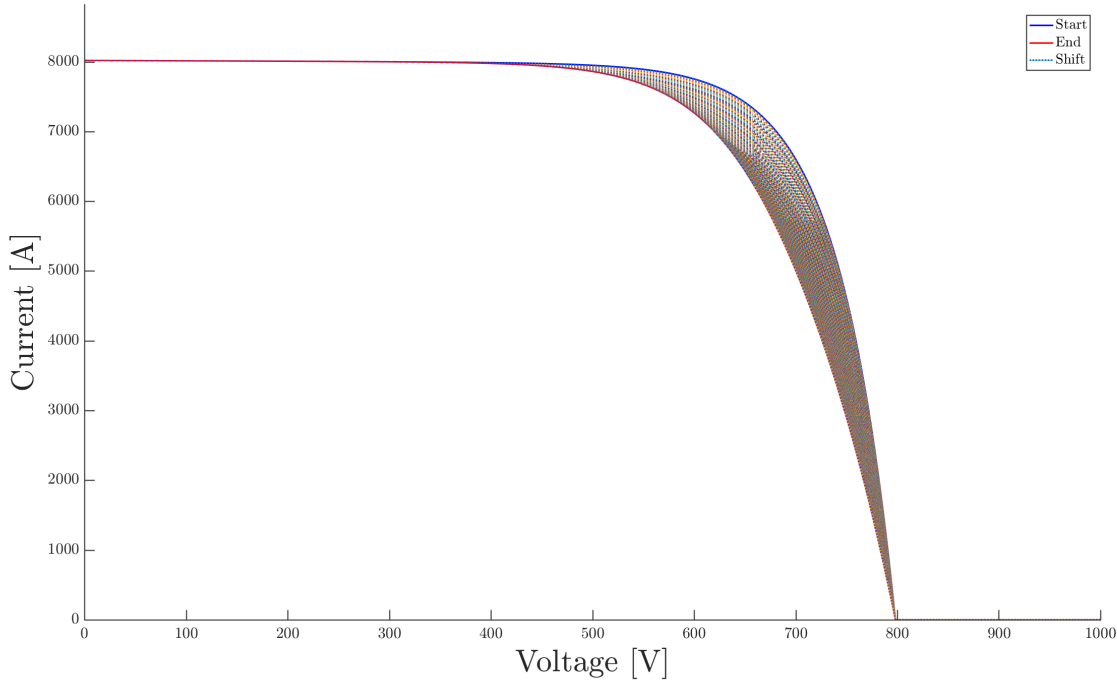


Figure 3.4: Shift of the I-V curve due to the Newton-Raphson method. The blue line represents the initial guess, and the red line indicates the final I-V curve. This system uses 769 strings in parallel and 20 in series and is only meant as an illustration.

Using the Newton-Raphson method takes very few iterations to reach an acceptable error margin. Using just one module and three iterations, the difference between $|I_{PV,n} - I_{PV,n+1}|$ is less than 0.01 %.

The one diode model is somewhat inaccurate in the performance of a cell at low irradiance as the recombination losses in the depletion region of the cell are approximated through the diode ideality factor, which does not reflect a real cell [93]. A more comprehensive and complicated model which incorporates these losses, the two diode model, is shown in figure 3.5.

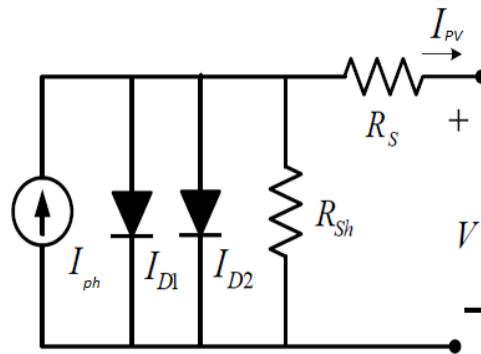


Figure 3.5: A schematic of the two diode model, adapted from [86].

In a recent paper by Shannan et al. it was shown that at STC the two diode model can take up to 30% longer to produce results than the one diode model would [93]. However, when temperature variations are included the error of the one-diode model is larger as shown below in figure 3.6.

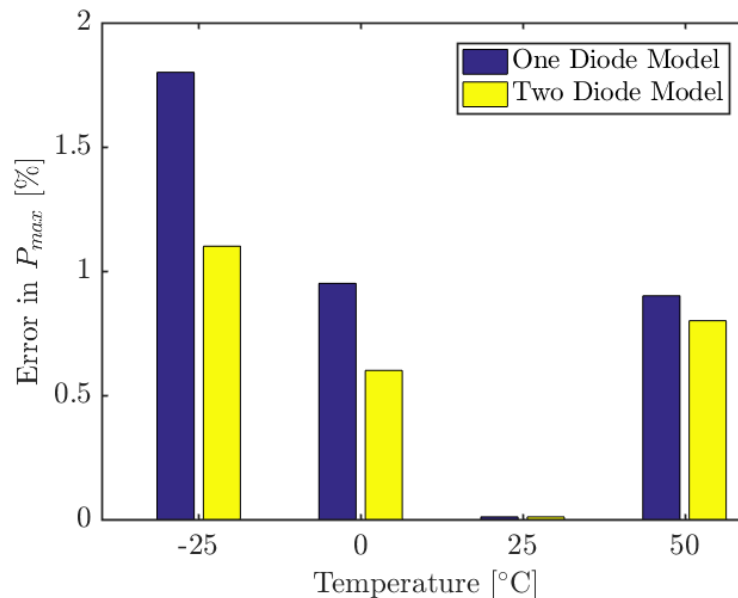


Figure 3.6: Error in P_{mpp} at varying temperatures [93].

Figure 3.6 shows the error in maximum power estimation for c-Si solar cells. It is not stated whether these are mono-, poly-, or multi-crystalline, let alone if this applies for MWT or regular cells. However, the exact value of the error is perhaps not entirely relevant; because the model that will be constructed will be placed in Broome where the module temperature is usually between 30°C and 65°C, it is reasonable to assume that the error of the one diode model will be small. Therefore, the one diode model as used by PVsyst is acceptable to model this system and will therefore be implemented. The accuracy of PVsyst itself has been shown to be quite high [41, 60, 92]. It is worth mentioning that this model can also be applied to other locations, as the module temperature is most likely lower than the module temperatures in Broome due to its high irradiance and temperatures.

3.2 Diode Ideality Factor

In order to use this model the parallel (shunt) and series resistances must be found and substituted into equation 3.1. A good approximation for the shunt (parallel) resistance R_p is the inverse of the slope of

the I-V curve at short circuit ($V = 0$) [19]:

$$\left. \frac{\partial I}{\partial V} \right|_{V=0V} = -\frac{1}{R_p} \quad (3.18)$$

As this is given by the producer of the solar panels however, the value from the datasheet will be taken as constant. The DIF is however not provided. PVsyst assumes this to be constant at 1.35, a measurement taken at nominal operating cell temperature (NOCT). In reality this changes, depending on the irradiance, temperature, and even voltage [38]. We will assume it to be uniform throughout a single I-V profile.

The DIF can be found by minimizing the absolute value of the following equation at the maximum power point [106]:

$$\left. \frac{dI}{dV} \right|_{\text{mpp}} + \frac{I_{\text{mpp}}}{V_{\text{mpp}}} \quad (3.19)$$

Taking the derivative of equation 3.13, the following is found:

$$\frac{dI}{dV} \left(1 + \frac{R_s}{R_p} \right) = -I_{\text{sat}} e^{\frac{V+IR_s}{V_t(T)N_{cs}}} \left[\frac{1}{V_t(T)N_{cs}} + \frac{dI}{dV} \frac{R_s}{V_t(T)N_{cs}} \right] - \frac{1}{R_p} \quad (3.20)$$

$$\frac{dI}{dV} \left(1 + \frac{R_s}{R_p} \right) + I_{\text{sat}} e^{\frac{V+IR_s}{V_t(T)N_{cs}}} \frac{dI}{dV} \frac{R_s}{V_t(T)N_{cs}} = -I_{\text{sat}} e^{\frac{V+IR_s}{V_t(T)N_{cs}}} \frac{1}{V_t(T)N_{cs}} - \frac{1}{R_p} \quad (3.21)$$

$$\frac{dI}{dV} = \frac{-\frac{I_{\text{sat}}}{V_t(T)N_{cs}} e^{\frac{V+IR_s}{V_t(T)N_{cs}}} - \frac{1}{R_p}}{1 + \frac{I_{\text{sat}} R_s}{V_t(T)N_{cs}} e^{\frac{V+IR_s}{V_t(T)N_{cs}}} + \frac{R_s}{R_p}} \quad (3.22)$$

Hence, the diode ideality factor can be found by minimizing the following equation:

$$\left| \frac{-\frac{I_{\text{sat}}}{V_t(T)N_{cs}} e^{\frac{V_{\text{mpp}}+I_{\text{mpp}}R_s}{V_t(T)N_{cs}}} - \frac{1}{R_p}}{1 + \frac{I_{\text{sat}} R_s}{V_t(T)N_{cs}} e^{\frac{V_{\text{mpp}}+I_{\text{mpp}}R_s}{V_t(T)N_{cs}}} + \frac{R_s}{R_p}} + \frac{I_{\text{mpp}}}{V_{\text{mpp}}} \right| \quad (3.23)$$

Using this equation, the following DIF values are found.

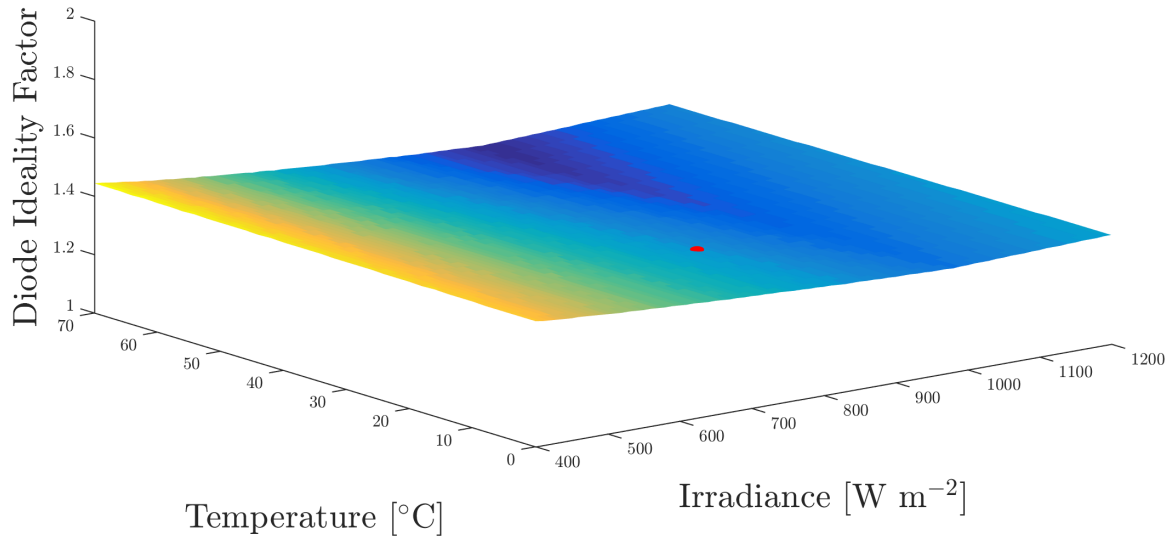


Figure 3.7: Variations in DIF as a result of varying operating conditions. The red dot indicates NOCT conditions.

At NOCT the DIF is 1.38, which varies 1.9% from the value PVsyst uses. However, it is visible from figure 3.7 that the DIF varies with changing temperatures and irradiance, from a minimum of around 1.3 to a maximum of 1.5.

If the DIF is fixed at its minimum or maximum the variation in output H_2 is approximately 1%. Due to this small variation it is assumed that the assumption PVsyst makes is adequate and no further attempts to rectify this will be made.

There are many different papers detailing how to best calculate the DIF. For more methods, see [1, 9, 20, 27, 43, 48, 53, 71, 88, 94].

3.3 Calculating the open circuit voltage and short circuit current

The data for the maximum power point connection is computed by PVsyst, which is then given as an output for hourly intervals. From this it is beneficial to recompute the V_{oc} and I_{sc} as these, together with the incident irradiation and module temperature, fix the I-V curve.

V_{oc} and I_{sc} can be determined by using equation 3.13 at the maximum power point:

$$I_{mpp} = I_{ph}(G, T) - I_{sat}(G, T) \left[e^{\frac{V_{mpp} + I_{mpp}R_s}{V_t(T)N_{cs}}} - 1 \right] - \frac{V_{mpp} + I_{mpp}R_s}{R_p} \quad (3.24)$$

$$I_{mpp} = I_{sc} \frac{G}{G_{STC}} - \left(I_{sc} \frac{G}{G_{STC}} - \frac{V_{oc}}{R_p} \right) \left[\frac{e^{\frac{V_{mpp} + I_{mpp}R_s}{V_t(T)N_{cs}}} - 1}{e^{\frac{V_{oc}}{V_t(T)N_{cs}}} - 1} \right] - \frac{V_{mpp} + I_{mpp}R_s}{R_p} \quad (3.25)$$

Rewriting gives us:

$$I_{sc} = \frac{I_{mpp} - \frac{V_{oc}}{R_p} + \frac{V_{mpp} + I_{mpp}R_s}{R_p}}{\frac{G}{G_{STC}} - \frac{G}{G_{STC}} \left[\frac{e^{\frac{V_{mpp} + I_{mpp}R_s}{V_t(T)N_{cs}} - 1}}{e^{\frac{V_{oc}}{V_t(T)N_{cs}} - 1}} \right]} \quad (3.26)$$

By varying the V_{oc} , and thus the I_{sc} , the I-V curve given by equation 3.13 will change. The correct V_{oc} and I_{sc} is found when the P-V curve has its maximum power point at (V_{mpp}, P_{mpp}) . This is shown in figure 3.8.

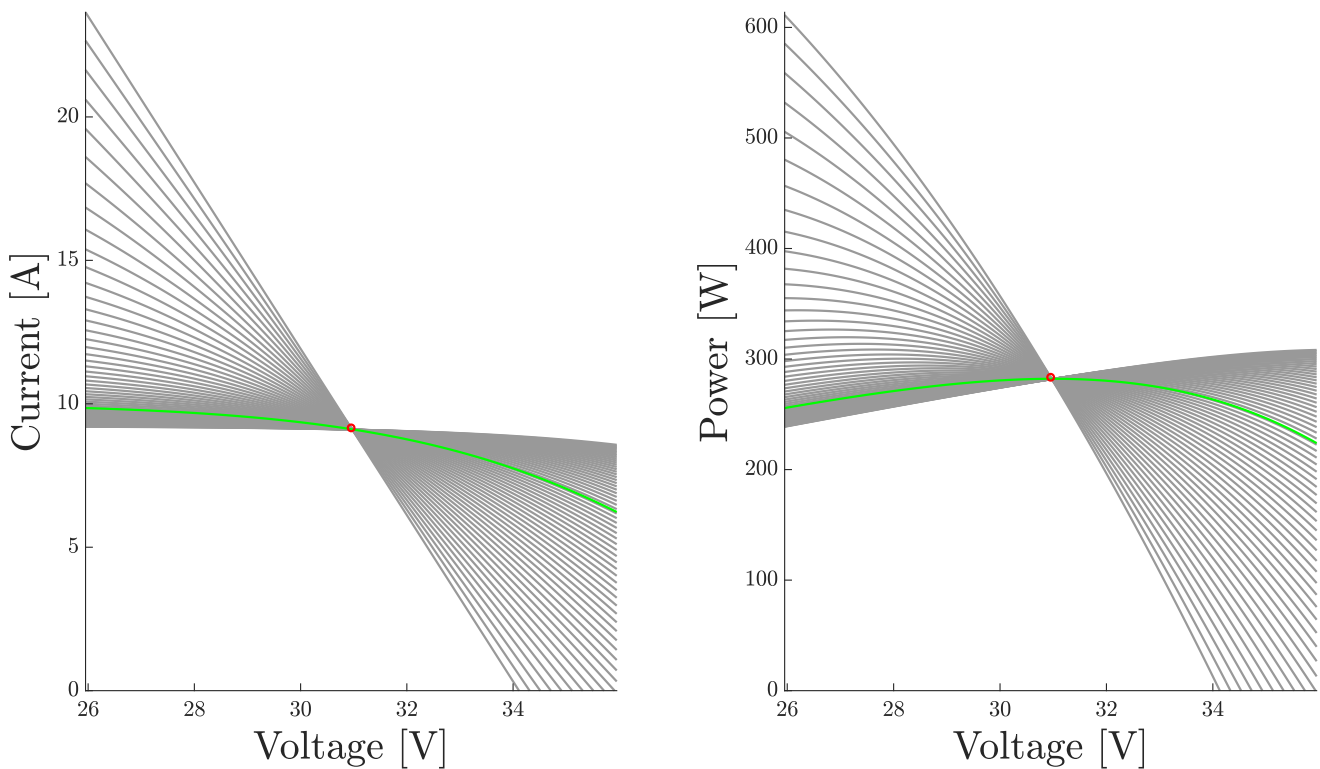


Figure 3.8: All I-V and P-V curves have different V_{oc} and I_{sc} values and go through the MPP as defined by PVsyst, shown in red. However, only one has the MPP shown in red at its maximum. This line is indicated in green.

The following data is found when the V_{oc} and I_{sc} are calculated for all data points from PVsyst.

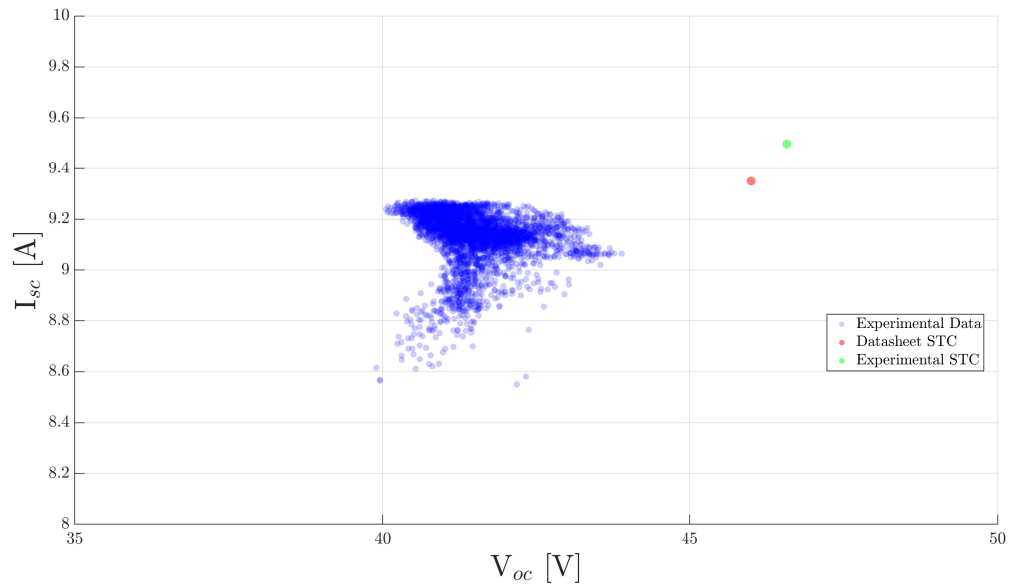


Figure 3.9: Finding the V_{oc} and I_{sc} (corrected to 1000 W m^{-2}) from PVsyst data for irradiances more than 100 W m^{-2} .

Using the now calculated V_{oc} and I_{sc} it is possible to reconstruct the I-V curves for each moment in time. Comparing the voltages from PVsyst to the reconstructed MPP voltages from our model can show that the calculations done have not augmented the data and that hence our reconstructed values are as trustworthy as those generated by PVsyst.

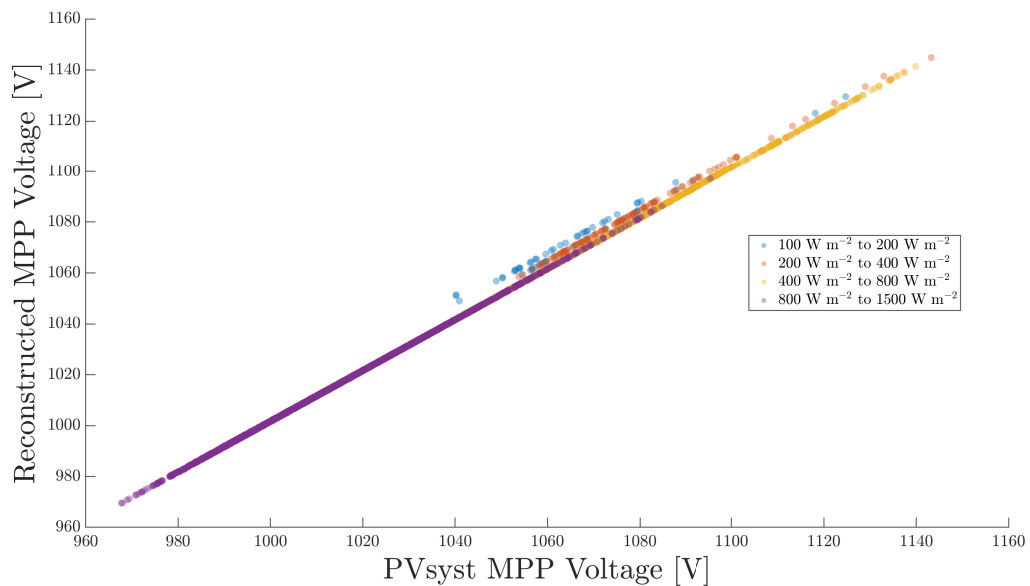


Figure 3.10: Comparing the V_{mpp} 's from PVsyst and the reconstructed I-V curves, for irradiances higher than 100 W m^{-2} .

From this we see that the points lie mostly along a straight line ($V_{reconstructed} = V_{PVsyst}$), although there are some deviations where the reconstructed voltage is much higher than the reconstructed voltage which happens under low irradiance. The overall shape of the line supports our decision to use the reconstructed V_{oc} and I_{sc} approach and shows that there is a strong correlation.

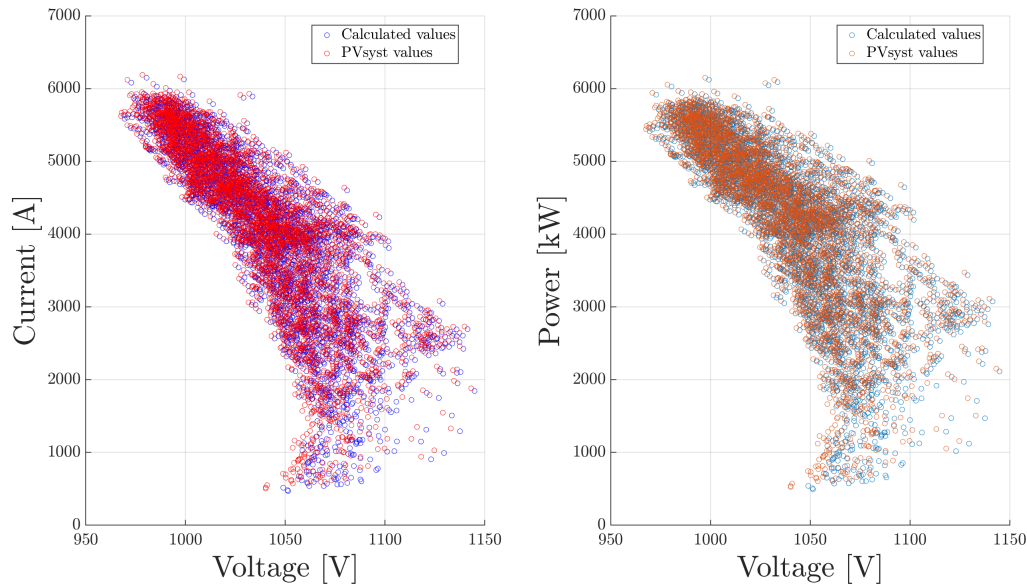


Figure 3.11: Comparing the MPP points from PVsyst to the reconstructed MPP points for irradiances higher than 100 W m^{-2} .

The total power generated in the reconstructed case has a systematic error of $+0.8\%$ compared to the values PVsyst gives. The consequence of the slightly higher reconstructed voltages is that the power production is also slightly higher than what is predicted by PVsyst, increasing the time the electrolyzers can operate slightly. However, as the average difference is quite small this effect will not further be compensated for. The difference in cutoff points along the y-axis is due to the direct relation between current and irradiance, while the power also depends on other elements such as temperature. Looking at a single time frame with a high irradiance (more than 1000 W m^{-2}) the following match is found:

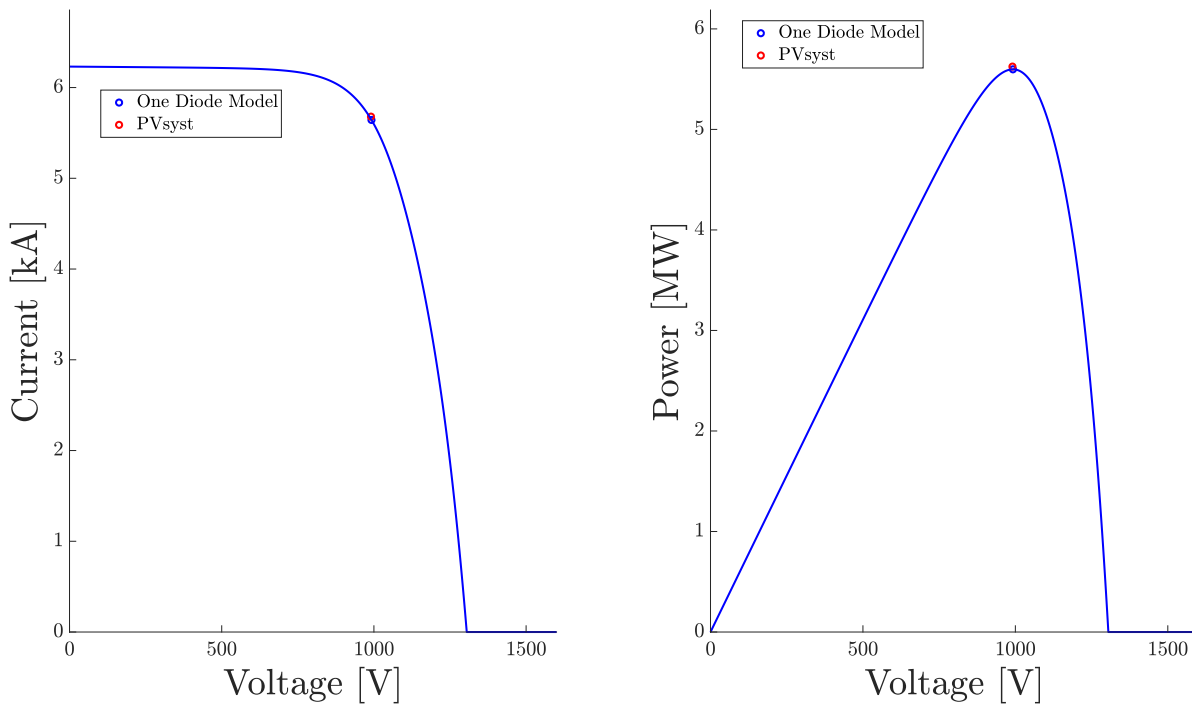


Figure 3.12: I-V curve matching on 11:00 (AM) on January 12th.

In figure 3.12 the power at MPP deviates by 0.48% further supporting the validity of the model.

3.4 Intersection points for DC connection

Using the V_{oc} and I_{sc} found in the previous section and equation 3.13 it is possible to find the I-V curve for each data value provided by PVsyst. The electrolyzer I-V curve is given in section 2.1.

To find the intercept of the I-V curve of the electrolyzer and the PV array, the Newton-Raphson iteration method is used. This is applied as follows:

$$f(V_n) = I_{PV}(V_n) - I_{EZ}(V_n) \quad (3.27)$$

At the intersection point $I_{PV}(V_i) = I_{EZ}(V_i)$, meaning $f(V_i) = 0$. Newton-Raphson finds this point by iterating as follows:

$$V_{n+1} = V_n - \frac{f(V_n)}{\frac{\partial f(V_n)}{\partial V}} = V_n - \frac{I_{PV}(V_n) - I_{EZ}(V_n)}{\frac{\partial I_{PV}(V_n)}{\partial V} - \frac{\partial I_{EZ}(V_n)}{\partial V}} \quad (3.28)$$

Here, $\frac{\partial I_{PV}(V_n)}{\partial V}$ is given by equation 3.22 and $I_{PV}(V_n)$ by equation 3.13. $I_{EZ}(V_n)$ is given by equation 2.8, and $\frac{\partial I_{EZ}(V_n)}{\partial V}$ is given by:

$$\frac{\partial I_{EZ}(V_n)}{\partial V} = A \quad (3.29)$$

with A given in section 2.1.

A (simple) MPPT algorithm can be implemented here as an initial guess, as the system being modelled ideally has the intersection point near the MPP. The open circuit voltage MPPT method proposes that a good estimation of the maximum power point voltage \tilde{V}_{mpp} can be expressed as:

$$V_0 = \tilde{V}_{mpp} = kV_{oc} \quad (3.30)$$

with $k = 0.75$ [82]. Using this as a first guess and iterating according to the Newton-Raphson method, this gives the following result for a randomly selected time interval:

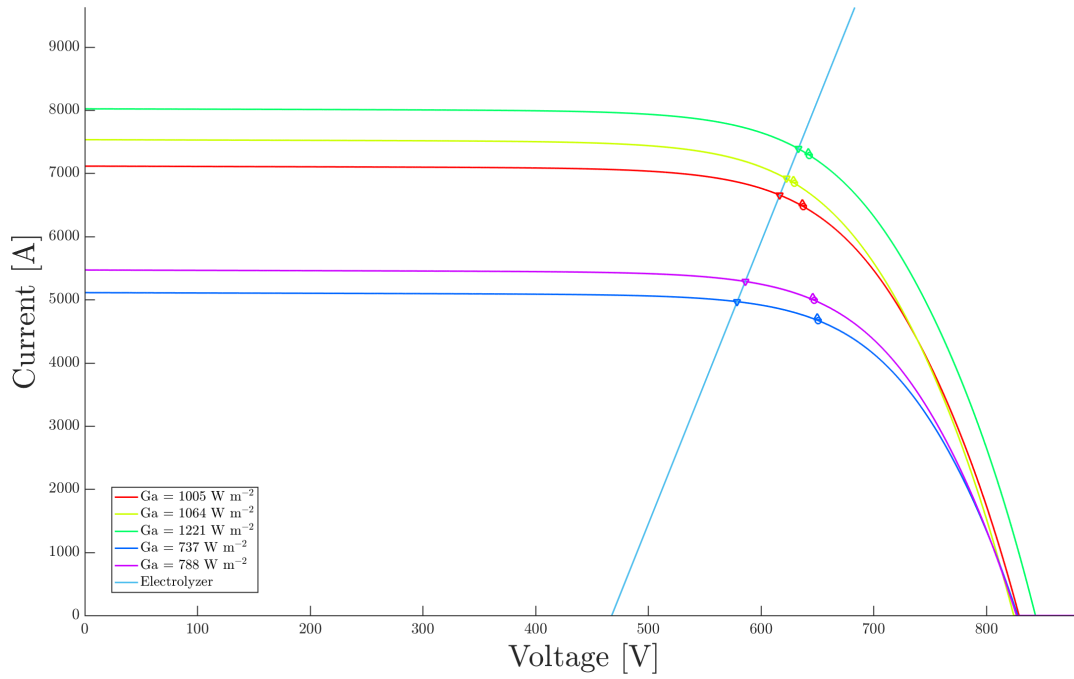


Figure 3.13: Operating points of a sample direct coupled system. \triangle indicates the MPP as defined by PVsyst, \circ indicates the MPP found by MATLAB using the average V_{oc} and I_{sc} , and ∇ indicates the intersection of the I-V curves.

The system used in figure 3.13 represents a feasible layout for scenario 1. The reason that the I-V curve of the electrolyzer is positioned to the left of the MPP points is because the PV system rarely operates at or above P_{STC} . This is shown below in figure 3.14.

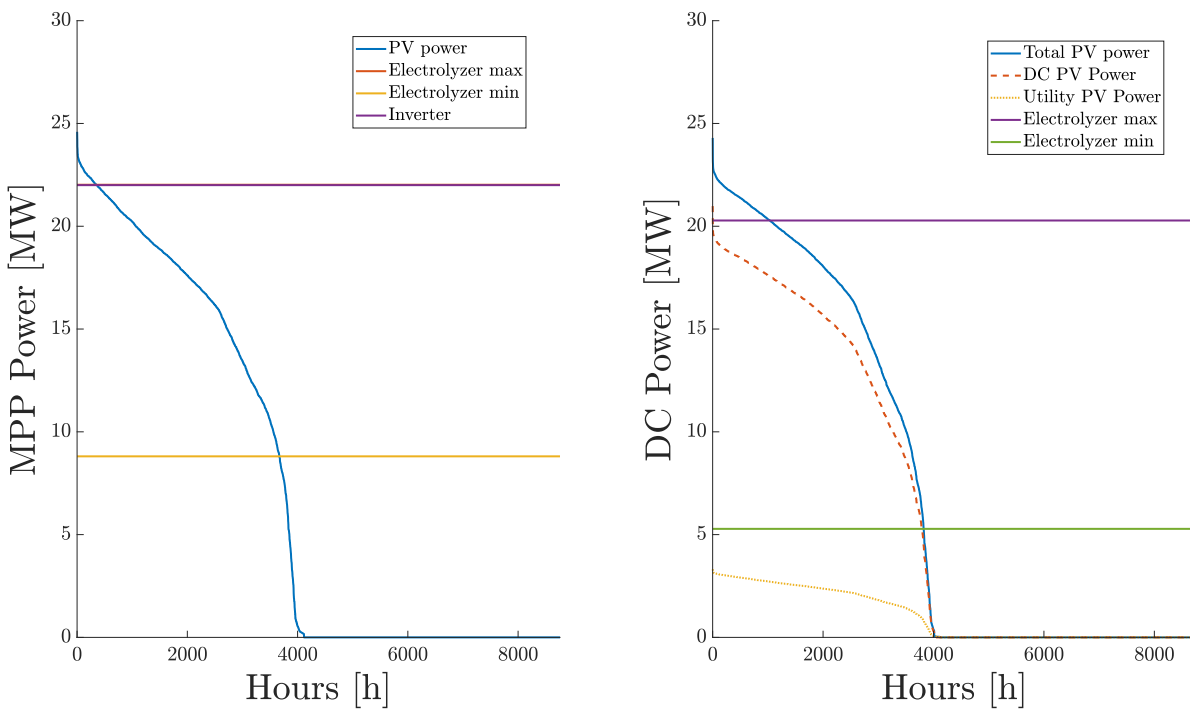


Figure 3.14: Power curve of a 6.6 MW_p solar power system showing curtailment. On the left, the inverter and maximum electrolyzer capacity are placed closely together.

Sizing the electrolyzer for the maximum electricity generation would cause a large portion of the bottom of figure 3.14 to fall away. Therefore, we see that it is better to indeed size the inverter and electrolyzer for a slightly smaller system as increasing the electrolyzer system size will cut off a larger portion of the incoming energy than what is gained by decreasing the amount curtailed.

Chapter 4

System components

In this chapter the different system components that will be used to connect the PV and electrolyzer systems will be addressed. Some of these, such as the inverter and battery, will not be present in all of the different scenarios.

4.1 Transformers and inverters

There are different kinds of inverters that can be used in a PV system. String inverters (SI) or central inverters (CI) can operate multiple modules at their average maximum power point and are most commonly implemented due to their low price to capacity ratio. It is also possible to implement MPPT on a module level, through either power optimizers (PO) or micro-inverters (MI). String and central inverters combine the inputs of multiple panels and find the average MPP of their combined outputs. Micro-inverters convert the DC power of each individual panel to AC power, while power optimizers instead act as transformers, stepping up or down the voltage of each panel to ensure a constant DC current for multiple cells in series. The power then gets fed to a companion central inverter, which transforms the DC power to AC power. A power optimizer is comparable to an inverter split in two; one part optimizes the solar panel output on a modular level, while the other acts as an inverter for multiple panels [24]. MPPT on a module level is usually only implemented on rooftops and for small PV systems. For large systems central inverters are preferred, due to the lower cost per W_p .

Transformers are similar to inverters, except for that they convert the DC current from the solar panels to DC current at a different voltage level. These can also include MPPT technology. They can be found for different sizing options, analogous to the different inverter types. Transformers are required for DC microgrids as most DC loads, such as batteries or electrolyzers in this case, require a constant voltage to operate at.

Assuming standby and load-dependent losses small, DC/DC transformers have efficiencies between 94-99.9% [29, 76, 104]. In this report the DC/DC transformer efficiency will be chosen in the higher part of this range to accurately reflect literature and future developments: all DC/DC transformer actions will have an efficiency of 99%. Inverter efficiency will be taken as 98%, using SMA inverters as an indication of typical efficiencies. The inverters are assumed to have a lifetime equal to that of the PV system.

4.2 Battery

Lithium ion batteries are used in a lot of different devices currently, and they are constantly improving in terms of energy density, power density, and cost. These batteries are preferred by many, due to their fast response time and abundance. Additionally, the efficiency is slowly increasing as well.

Efficiencies are frequently reported between the 93% and 95% [3, 39]. In this report an average

efficiency of 95% will be adopted, accounting for future increases in efficiency. In reality the efficiency depends on a number of factors such as the speed of charge and charging voltage [101]. In this report a constant efficiency will be assumed.

The lifetime of batteries is defined in terms of cycles, in which the battery charges and discharges. In literature a lifetime of between 4,000 to 8,000 cycles is found [3]. Assuming one cycle per day for twenty years, a cycle life of 7,300 would correspond to the lifetime of the PV modules. This lies within the range found in literature, and will therefore be adopted in this report. In literature it is found that the lifetime and degradation of batteries depends heavily on factors such as the ambient temperature [61]. This will not be taken into account in this report.

These batteries can furthermore hold their charge over a long time, with a 1%-5% monthly self-discharge [39]. The batteries implemented in this system will need to store energy during the day, and discharge these at night to operate the electrolyzer. Due to the small storage time, self-discharge will not be taken into effect. It has been deemed not feasible to store extra energy in the summer and spend this in the winter, as that would require a much larger capacity.

An overview of the different battery characteristics is given below in table 4.1.

Table 4.1: An overview of the battery characteristics used.

Property	
Efficiency	95%
Lifetime	7300 cycles
Self discharge	0%

4.3 Hydrogen storage

Regardless of how the hydrogen will be transported (could be in ammonia, as a liquid, or in another form), a constant stream of hydrogen will be needed. It is therefore necessary to either implement very large battery technology as discussed in section 4.2 or hydrogen storage. There are many different ways to store hydrogen, ranging from salt layer geography to piping solutions to new solid state hydrogen storage. In this report salt caverns and salt layer geographies will be excluded as this can only be applied when the geography is suitable, and new solid state hydrogen storage will be excluded because many of the technologies that fall under this label have not been proven yet at this scale.

The piping required for this project should last for about one day, meaning that it is acceptable that there is a day in which there is almost no sun and hence the system should hold 3 tons of H₂. A large advantage of piping over battery technology is that piping is needed anyway to transport the hydrogen to the liquefaction plant, reducing costs for the storage system.

4.4 Cabling

Typically, an electrical cable can have up to 5% voltage drop across it. To size the cable the following equation is used:

$$V_{drop} = IR = I \frac{\rho \cdot l}{A} \quad (4.1)$$

where I is current through cable, R is resistance of the cable, A is cross-sectional area, l is length of cable and ρ the resistivity of the cable. The resistivity of copper at 25°C is $\rho = 1.72 \cdot 10^{-8} \Omega \text{ m}$. Rewriting the equation above, we find the cross-sectional area for the cable as:

$$A = \frac{I \cdot \rho \cdot l}{0.05 \cdot V} \quad (4.2)$$

This equation gives the minimum cross-sectional area required. Instead of using the price of copper to calculate the cost of materials required for the cabling, it was deemed more accurate to use an average

cost of cabling per km, determined from [16]. This will be used in section 6.6 to determine the cable costs.

Chapter 5

Model tools

In the following sections different tools will be used to gain more insight into how the PV array will function, and how well the electrolyzer will respond.

5.1 Dependency

It is well known that the performance of the PV system depends on the module temperature and irradiance. Varying these and applying equation 3.13, the following relationships are seen.

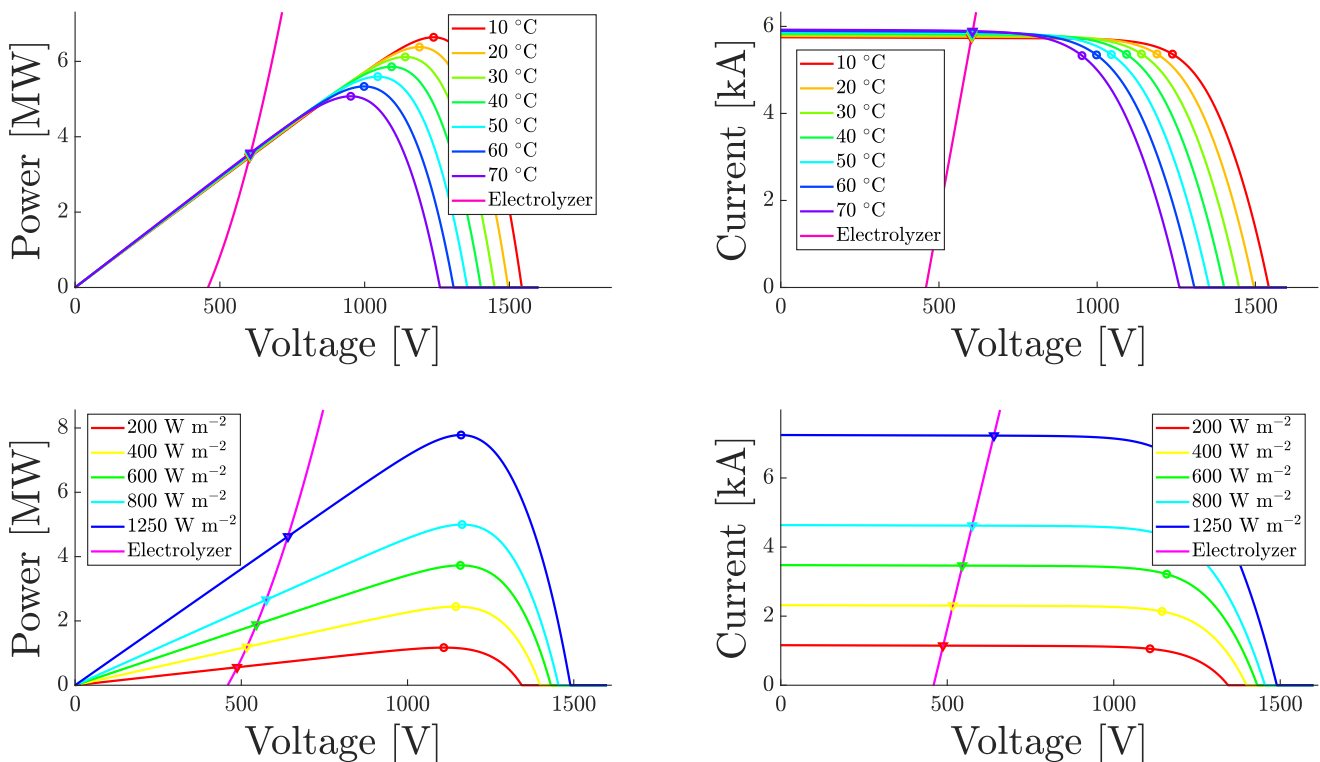


Figure 5.1: Temperature and Irradiance Dependency.

This is largely in line with literature, as the V_{oc} and I_{sc} change as the temperature and irradiance is changed. Figure A.1 in appendix A gives the I-V curves for the Tallmax modules, manufactured by Trina Solar. These show the same behavior as seen in figure 5.1. The specifications of the Tallmax modules, as well as their I-V and P-V curves, can be found in appendix A. From this it is feasible to

conclude that the one diode model works well.

5.2 Ramping

It has been speculated that the ramping up or down of the PV array can cause the electrolyzer to deteriorate quickly or cause other large problems. A sudden increase in voltage is especially dangerous, as the alkaline electrolyzer will not be able to respond as quickly. Ramping can also be seen as the speed at which an electrolyzer can change its DC power intake. Exceeding this can cause power to be wasted or electrolyzers to degrade, as speculated by Eichman et al. [26].

Depending on what paper is used, ramping can be instantaneous or can take around 20 minutes to reach the minimum threshold to produce hydrogen [10]. In this ramping investigation we will assume the electrolyzer to have a standby mode, meaning that it will be able to reach the minimum threshold to make hydrogen quickly. Furthermore, to go from the minimum threshold to produce hydrogen to the maximum load a maximum ramping rate of around 10% of max load per second is allowed. Some electrolyzers also come with a power conservation mode, which can reduce the start up time to minimum load to produce hydrogen to less than 1 minute. Ramp down can be at around 20-25% of maximum load per second [56]. Other sources such as NREL claim that alkaline electrolyzers can respond much quicker, up to 600% of the maximum current ramping down and up to 800% when ramping up [26].

Using the equations from the previous sections 2.1 and 3.1 it is possible to use meteorological data on a minute basis to find what the operating point is of the electrolyzer every minute. Here we assume the operating point to change linearly between each minute and the next. Wind data is also available from Broome, although this is given only on a monthly basis for each morning and afternoon. This has been extrapolated such that each day in the same month has the same wind speed every morning, as well as every afternoon. The module temperature has been found using the Duffie-Beckman model [46]:

$$T_M = T_a + \frac{T_{NOCT} - 20}{800} G \left(\frac{9.5}{5.7 + 3.8 \cdot w} \right) \left(1 - \frac{\eta_{PV}}{T \cdot \alpha} \right) \quad (5.1)$$

with w the wind speed at module height, T the transmittance of the module, α the absorptivity of the module, T_a the ambient temperature and η_{PV} the solar panel efficiency. Furthermore, the V_{oc} and I_{sc} values are calculated from the STC values as follows [46]:

$$V_{oc} = V_{oc,STC} + k_V (T_M - T_{STC}) + \frac{N_{cs}}{V_t(T)} \log \left(\frac{G}{G_{STC}} \right) \quad (5.2)$$

$$I_{sc} = I_{sc,STC} + k_I (T_M - T_{STC}) \quad (5.3)$$

This method is less accurate than the method described in section 3.3, as shown below in figure 5.2.

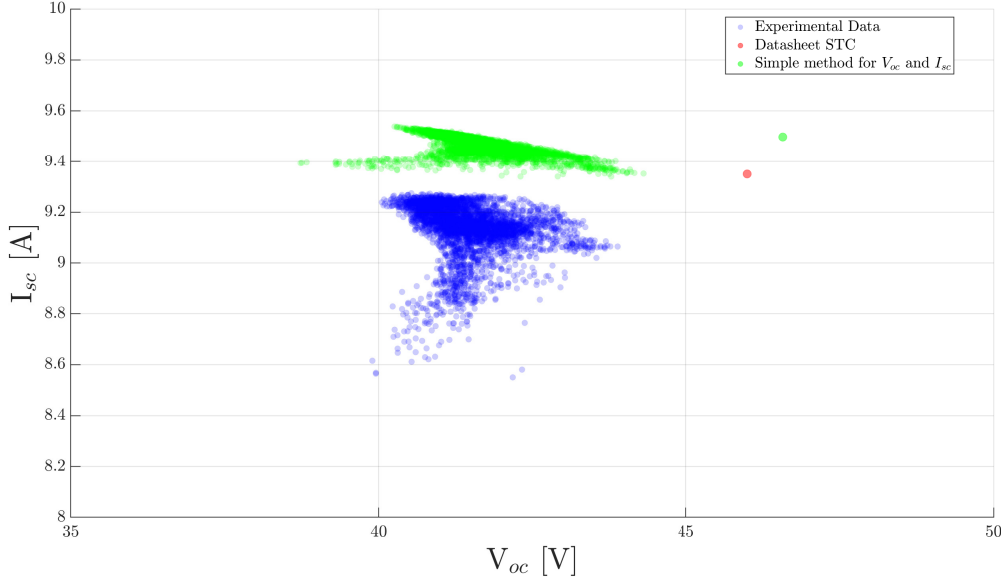


Figure 5.2: Comparing V_{oc} and I_{sc} data from PVsyst and equations 5.2 and 5.3.

We see here that the center of the new cloud is on average 0.5 A higher than the cloud generated via the previous method, and has a different shape. This will cause the I-V curve to shift upwards, resulting in a higher operating voltage. The ramping simulation will therefore be run twice; once with the V_{oc} and I_{sc} cloud seen above in figure 5.2 and one with the cloud moved down by 0.5 A. The increase in short circuit current is attributed to the simplicity of equation 5.3; here there is simple linear dependence on irradiance, which could incorrectly alter the current if the irradiance is not at the standard testing conditions of 1000 W m^{-2} .

We cannot use the process described in section 3.3 and the PVsyst data because PVsyst cannot handle data per minute. The data can however still be used; it is possible to reverse engineer the V_{oc} and I_{sc} corresponding to the PVsyst data using equations 5.2 and 5.3. In figure 5.2 we see that there is indeed a discrepancy with what the manufacturer claims their V_{oc} and I_{sc} are, and what the average is of the cloud generated via PVsyst and the aforementioned equations.

The second ramping simulation will use the average from figure 5.2. Further results of the ramping simulation are given in section 7.4.

It is worth noting that in these simulations weather data has been extrapolated from a small detector surface in the weather station to a whole PV field. In reality, clouds would not blanket the entire system in minutes meaning that the change in irradiance would be less pronounced, reducing the ramping rate even further. The speed of clouds has been shown to vary greatly, although the average is around 13 m s^{-1} and the maximum speed above 50 m s^{-1} [58]. Using a rough estimate of 55 kWh required to produce 1 kg of hydrogen, a daily production of 3 tons of hydrogen, a total solar and BoS efficiency of 15% and an average of 8.4 ESH per day, we find that $1.31 \cdot 10^5 \text{ m}^2$ is needed for the solar part of this system, or approximately 20 MW_p . Using a reasonably fast wind speed of 30 m s^{-1} , an average shading strength of 60%, taken from [58], and a square field, it would take approximately 17 seconds for the cloud to completely cover the PV array. A plausible power decrease as a result of clouds is shown below in figure 5.3.

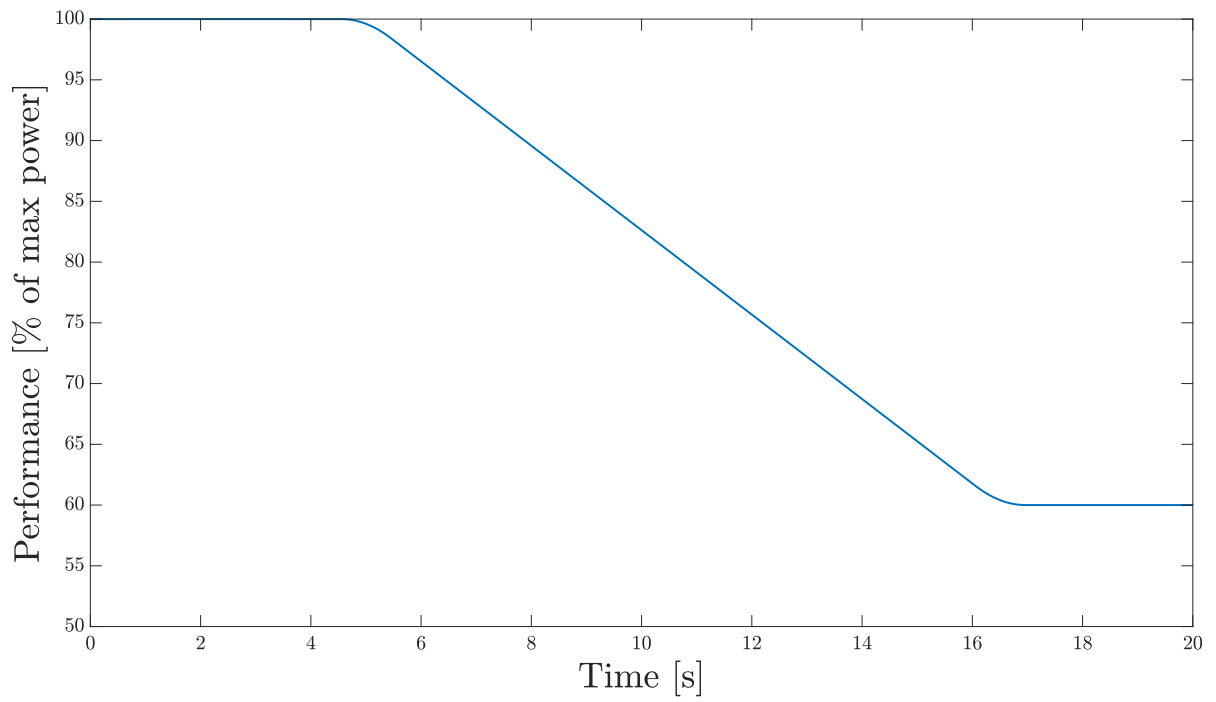


Figure 5.3: A simple cloud coverage simulation.

This shows that any results from the ramping simulation are most likely overestimated, as there is a maximum finite wind speed causing the operating point of the system to shift more slowly.

Chapter 6

Economic Evaluation

A comprehensive economic evaluation framework will need to be implemented in order to not only compare the different topologies but also to investigate the economic implications of building any kind of plant in Australia. In this report the financial figures and predictions from a number of different articles will be used.

The costs of land are not included as they are assumed to be marginal compared to the entire system cost, as this project will be built on land which has no other economic value than to host PV installations.

6.1 Layout

As a safety margin in PV design, electrical connections and components are sized to be 25% under the maximum current rating from the I_{sc} of all the strings connected. We furthermore assume that each panel is mounted length wise up, and the max V_{oc} and I_{sc} of the panels is approximately 48 volts and 10 A respectively. In the direct coupling topology, the maximum infeed to the DC busbar disconnecter is limited to 5000 A, meaning that the PV panels can inject at most 4000 A using a safety factor of 1.25. This means that a maximum of 400 panels are possible in parallel per busbar disconnecter. It is found that having 5 smaller plots produces the most optimum system configuration, and hence 5 plots will be used from now on.

In the other two topologies the central inverter is the constraint. The central inverter given in appendix B produced by SMA can be coupled together to accept up to 5.5 MW at 25°C. It is important to know approximately how many of these will be needed. Per inverter, up to 32 panels in series and 620 strings in parallel can be used. The topology of the electrolyzers is less important, as the transformer on the electrolyzer side will ensure that the correct operating point is fed to the electrolyzer system. Using an approximate specific energy demand of 55 kWh/kg and an average ESH of 8.4, it is found that we need approximately 20-25 MW_p to produce the required hydrogen. The inverter has a nominal power of 5.2 MW at 40°C, meaning that we need 4 inverters.

There must be some clearance to ground when mounting the panel. Hence, the center of the panel should be mounted 130 cm above the ground, resulting in the top of panel being 2.3 m above ground level when fully vertical. A separation of 3 times vertical height is assumed, leading to inter-string separation of approximately 7 m. Each panel is 1 m wide, meaning that for 32 panels in series the string would be approximately 32 m wide.

Using these measurements, we find that a land area of approximately 350 m by 350 m is needed for the PV installation in the MPP and DC scenarios.

In section 7.2 possible layouts will be discussed in more detail, and a comparison will be made between the centralized and decentralized layouts. Here we will also see that the number of panels needed to run the utilities for scenario 3 will also increase.

6.2 Electrolyzer

It is possible to make a prediction of the price of electrolyzers using the 2014 report "Development of Water Electrolysis in the European Union" [10]. The trend shown in figure 6.1 gives a good indication for the price evolution until 2030, after which we assume the same trend to take place.

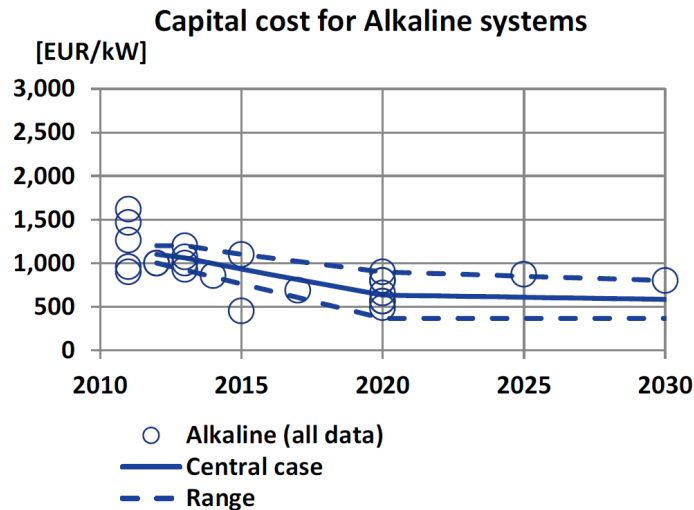


Figure 6.1: Electrolyzer CAPEX historical data and forecast until 2030, taken from [10].

We will take the line indicated by "central price" as our cost. This price encompasses the entirety of the electrolyzer installation. In scenario 3 (DC) the cost of the integrated transformer can be removed. For this, the price of a transformer from section 6.8 will be used.

The OPEX per year for electrolyzers is frequently quoted as being between 2-5% of the CAPEX [10, 13, 28, 79]. For this report an OPEX of 4% will be used in order to account for uncertainty in long term OPEX of electrolyzers but also to take the decrease in OPEX for large systems into account.

6.3 Photovoltaics

To estimate the cost of utility scale PV systems a forecast made by the International Energy Agency (IEA) will be used [45]; this is shown below in figure 6.2. In this report bifacial modules are not mentioned, although it is widely believed that these will decrease the price (in \$/kW) within a short time frame and will have a significant market share within a few years [37, 42]. It is furthermore predicted that bifacial modules could be combined with perovskite c-Si tandems cells in the future to create cheap and high efficiency solar panels [21].

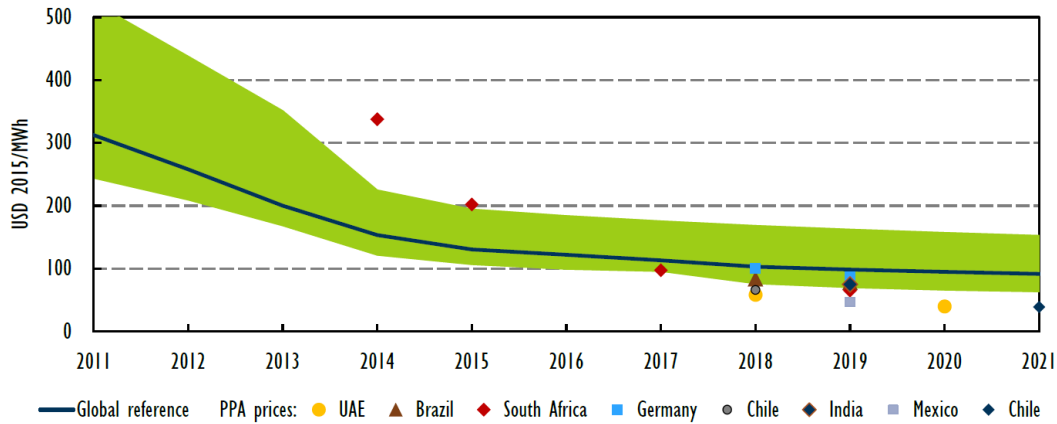


Figure 6.2: Historical and forecast LCOE range for utility-scale PV plants [45].

It is assumed that after 2021 the trend will continue, as although the absolute price to make a PV panel may decrease more rapidly and the efficiency may increase, other component costs like mounting may become more expensive. In this report the bottom of the green area reference will be used, as the IEA has a history of overestimating PV prices as shown below in figure 6.3.

Annual PV additions: historic data vs IEA WEO predictions
In GW of added capacity per year - sources World Energy Outlook and PVMA

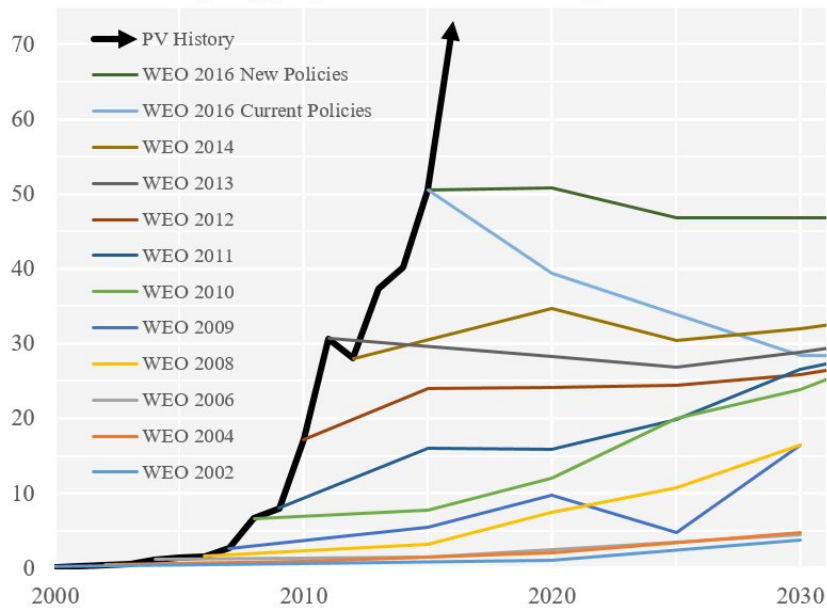


Figure 6.3: IEA forecasting trends [103].

In many papers a degradation of 0.5%/year is assumed [51, 52]. In this report it is furthermore assumed that the OPEX cost includes replacement of panels, meaning that the degradation is set to 0%. The lifetime of the entire PV system is set to 20 years, as this is frequently seen when looking for solar panels. Although there are panels available with longer lifetimes, it is assumed that 20 years is the lifetime that most panels will achieve.

To find the CAPEX and OPEX components a low interest rate of 4% is assumed, together with a lifetime of 20 years, and an average production of $2300 \text{ kWh kW}_p^{-1}$. Given is that the OPEX is 1% of the CAPEX [45]. From a 2017 LCoE of $95.2 \text{ USD MWh}^{-1}$, a CAPEX of $2273 \text{ \$ kW}_p^{-1}$ is found and an OPEX of $22.73 \text{ \$ kW}_p^{-1}$ for 2017.

Downtime for cleaning or reparations is not included in the PV simulation, as it is assumed that the effect of a single panel being cleaned or replaced will not have a large effect.

6.4 Battery costs

The reported cost of batteries varies greatly in literature. Values have been reported between 200-300 \$ kWh⁻¹ [22], while others report this to be 600 or 800 \$ kWh⁻¹ [3, 39]. In this paper an indicative value of 500 \$ kWh⁻¹ will be assumed, based also on conversations with Shell employees. This is in line with the predictions made by [75] shown in figure 6.4.

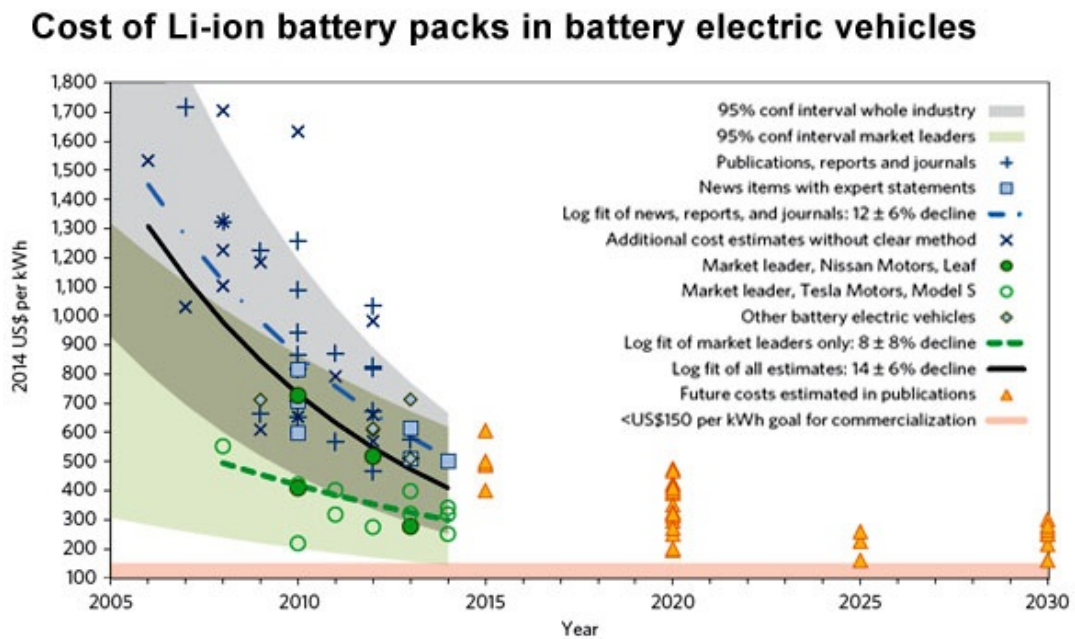


Figure 6.4: Historical data of CAPEX of car Li-ion battery systems, assumed to be comparable to batteries used in scenario 2 and 3 [75].

An OPEX of 2.5% will be used in order to account for the increase in monitoring and maintenance costs for these batteries [16].

6.5 Piping

The electrolyzers require an infeed of approximately 1 liter of pure process water to produce 1 Nm³ of hydrogen, as stated before. Each day 3000 kg of hydrogen should be produced, meaning 33,360 liter of water will be needed per day in total. The exact measurements of the different pipes required depend on the lengths and diameters of pipe needed. These are given later in section 7.2.

The CAPEX of the piping is estimated using raw material costs taken from [67, 68]. From this a number of extra costs (in percent of material costs) are applied: 200% for labor costs for installation, 6% for transport costs, 1000% for production from raw materials to pipe, and 15% for design and engineering [64].

The OPEX is furthermore taken as 2% of the respective CAPEX required [16].

6.6 Cable costs

The cost of cables will be determined using data from [16]. Here, Breyer et al. states that the average CAPEX of cables for a system like this is around $1.044 \text{ EUR kW}^{-1} \text{ km}^{-1}$. The OPEX will furthermore be taken as 0.29% of the CAPEX [16].

6.7 Hydrogen storage

Hydrogen storage is cheapest when this is done underground [4, 78]. To estimate the price of underground hydrogen storage a report from Kruck et al. will be used. This price is assumed to be constant because there is not enough information available to make an accurate prediction as to how this price evolves. Empty underground geological features are sometimes a cheaper but these are not present everywhere and thus it is assumed that the gaseous hydrogen should be stored in pipes underground [57, 78].

The CAPEX is taken as 390 \$/kg [57]. The efficiency is furthermore assumed to be 100% and the OPEX is taken to be 2% of the CAPEX [16]. These costs have been added to the economic evaluation framework.

6.8 Transformers and inverters

The price of the transformers and inverters are taken from [70]. It is assumed that the prices after 2020 will keep following the same trend as seen between 2016-2020.

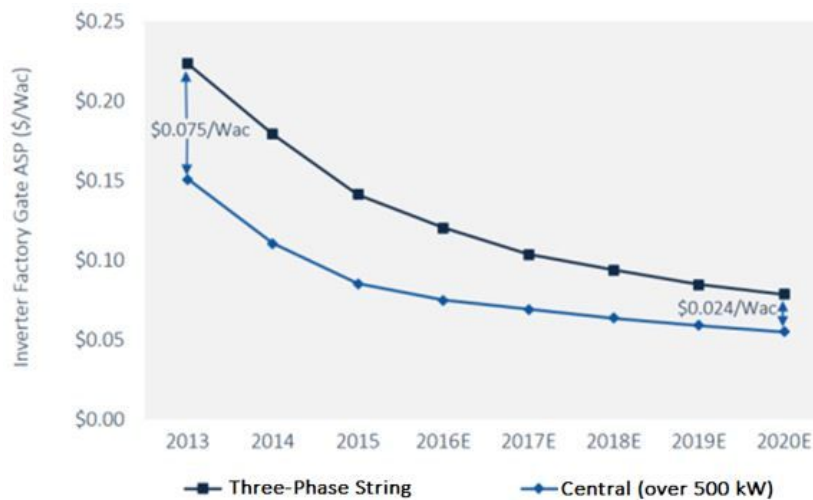


Figure 6.5: CAPEX of inverter stations, taken from [70]. In this report the bottom line will be used.

Furthermore, it is assumed that the price of an inverter is the same as that of a transformer, as no data or predictions could be found regarding transformers. The OPEX will be taken as 1% of the CAPEX [16].

Chapter 7

Results and Discussion

In this chapter the three different scenarios will first be independently assessed, after which they will be compared. An overview of the three different topologies can be found in figure 1.1. After this the results of the tools from chapter 5 will be provided and discussed.

The breakdown of the CAPEX and OPEX per scenario, as well as the comparison of the scenarios, is given in section 7.1.4. All of the prices below are including the extra costs of bank financing (7%).

7.1 Scenario topology optimization

7.1.1 Scenario 1: MPPT technology

In this scenario the standard MPP tracking approach is used, in which the panels are connected to a central inverter, and the power production is optimized using MPPT technology. The AC current is then fed to an alkaline electrolyzer, which is then converted back to DC power and fed into the electrolyzer, while also driving the utilities required. Using the PV and electrolyzer models described earlier, the following hydrogen production profile is found for one inverter:

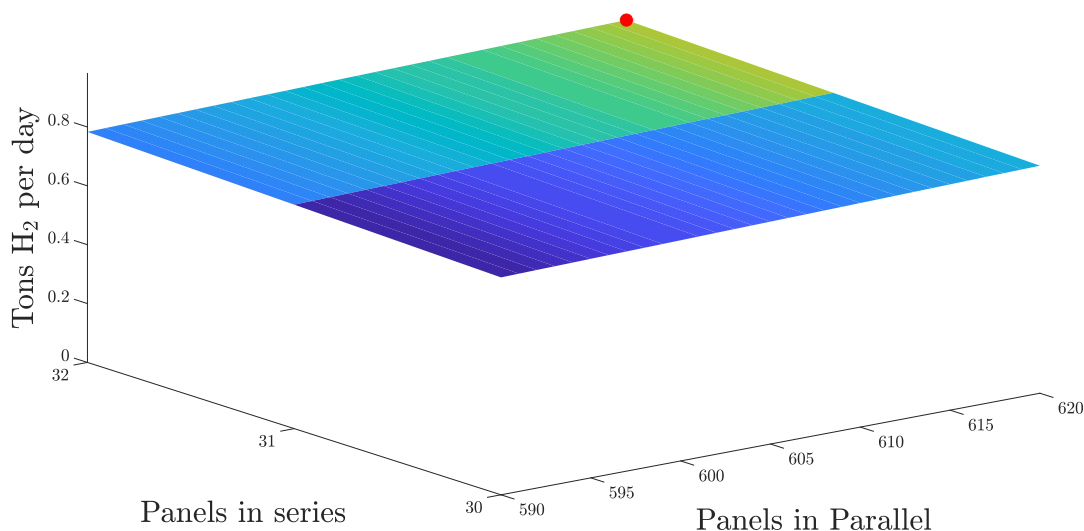


Figure 7.1: Hydrogen production using MPPT technology as in scenario 1 for one inverter, with a red dot showing the optimum number of panels.

Combining this with the economic evaluation framework found in chapter 6 and varying the number

of strings in parallel and panels in series as well as the number of electrolyzers in series and parallel, we see the following cost profile form:

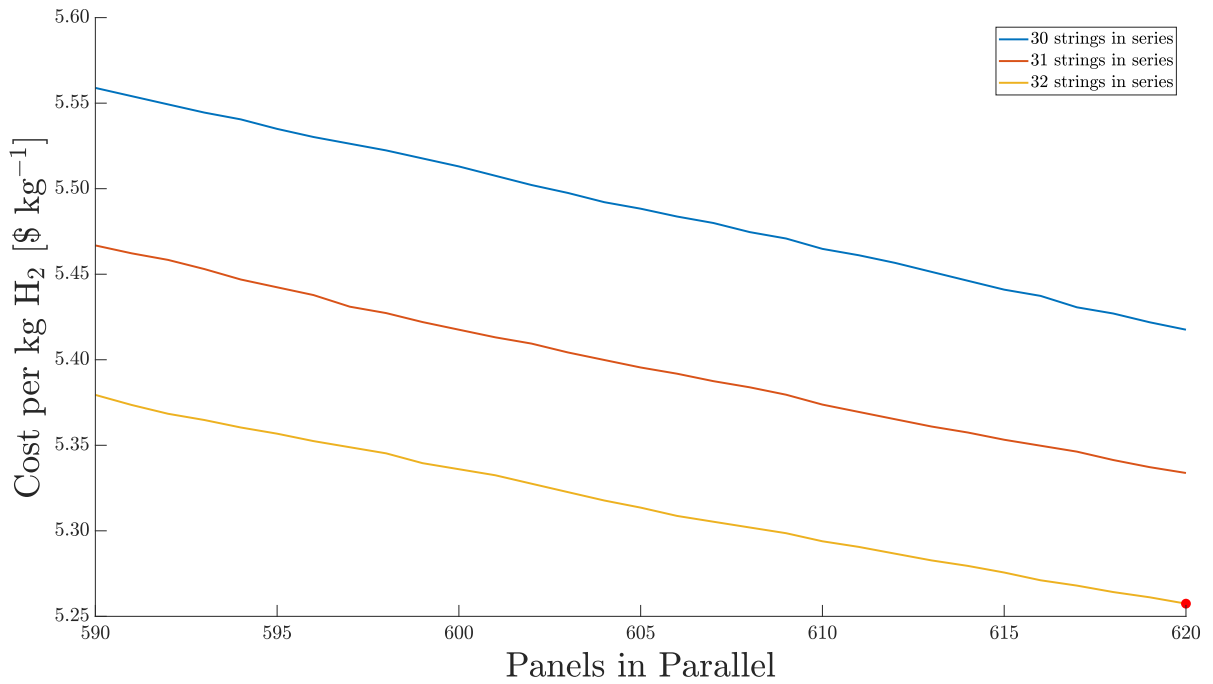


Figure 7.2: Costs for hydrogen production for scenario 1 over the entire system lifetime for one inverter, with the optimum configuration given by the red dot.

We see that despite increasing inverter curtailment the optimum configuration is to use the maximum number of panels. From this we can deduce that the electrolyzer limits are high enough that these are rarely met. This can also be seen in the power production graph, shown in figures 7.3. We see here that although the number of panels increases, the power utilized increases less, due to curtailment by the inverter.

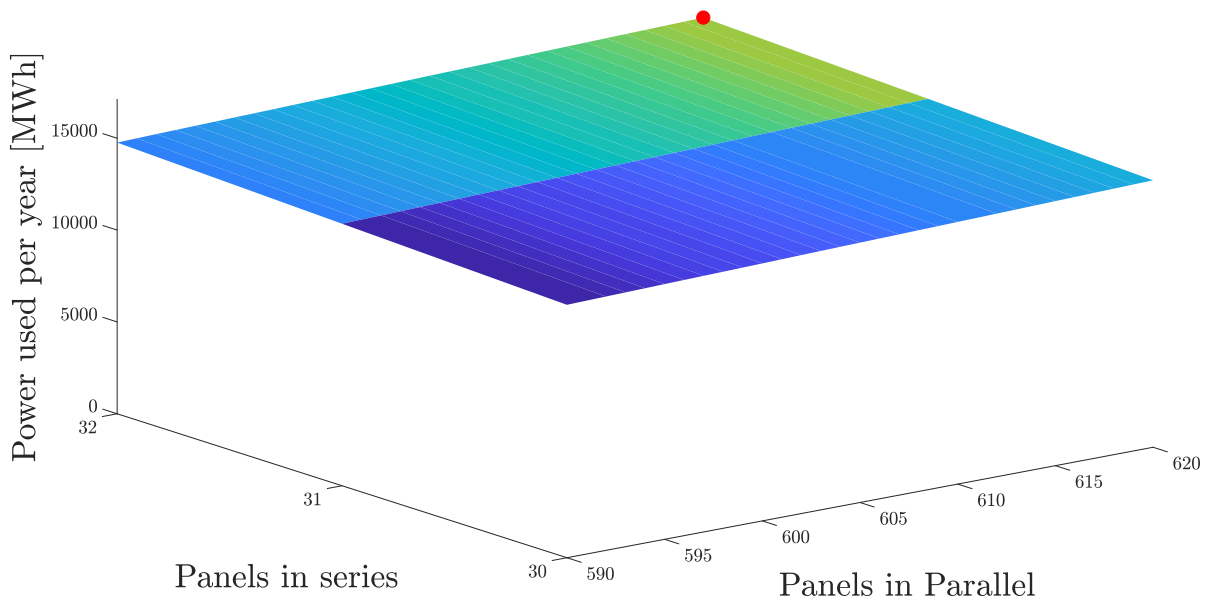


Figure 7.3: Power production from the solar farm using MPPT technology as in scenario 1 for one inverter, with a red dot showing the optimum number of panels.

The lowest price for hydrogen is \$4.16, found at 32 panels in series and 620 strings in parallel, with 6 electrolyzers in series and 19 electrolyzer strings in parallel per plot. From this we can deduce that the restrictions imposed by the inverter are limiting the optimum panel arrangement and number of panels that can be placed. However, moving to more plots only further increases the price.

7.1.2 Scenario 2: MPPT technology with battery

In this scenario the standard MPP tracking approach is used and supported by the implementation of a battery. The panels are first connected to a central inverter, and the power production is optimized using MPPT technology. The AC current is then fed to a charge controller, which can store or draw energy from the battery. The rest of the energy that is not put in to the battery is fed to an alkaline electrolyzer, which is then converted back to DC power and fed into the electrolyzer, while also driving the utilities required. Using the PV and electrolyzer models described earlier, the following hydrogen production profile is found:

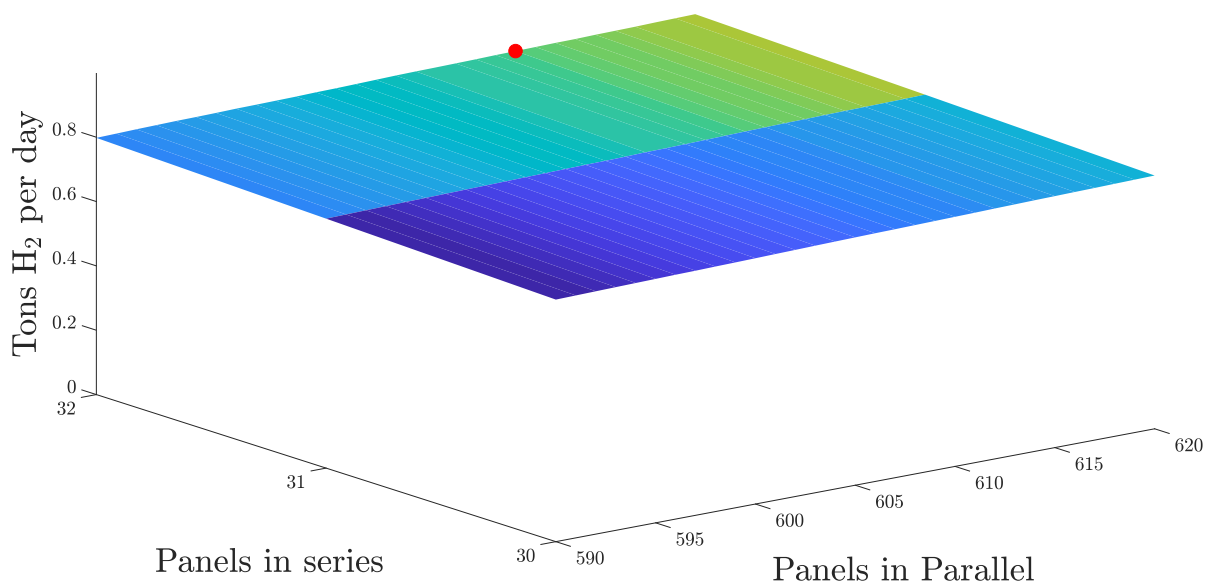


Figure 7.4: Hydrogen production using MPPT technology as in scenario 2 for one inverter, with a red dot showing the optimum number of panels.

Combining this with the economic evaluation framework found in chapter 6 and varying the number of strings in parallel and panels in series as well as the number of electrolyzers in series and parallel, we see the following cost profile form:

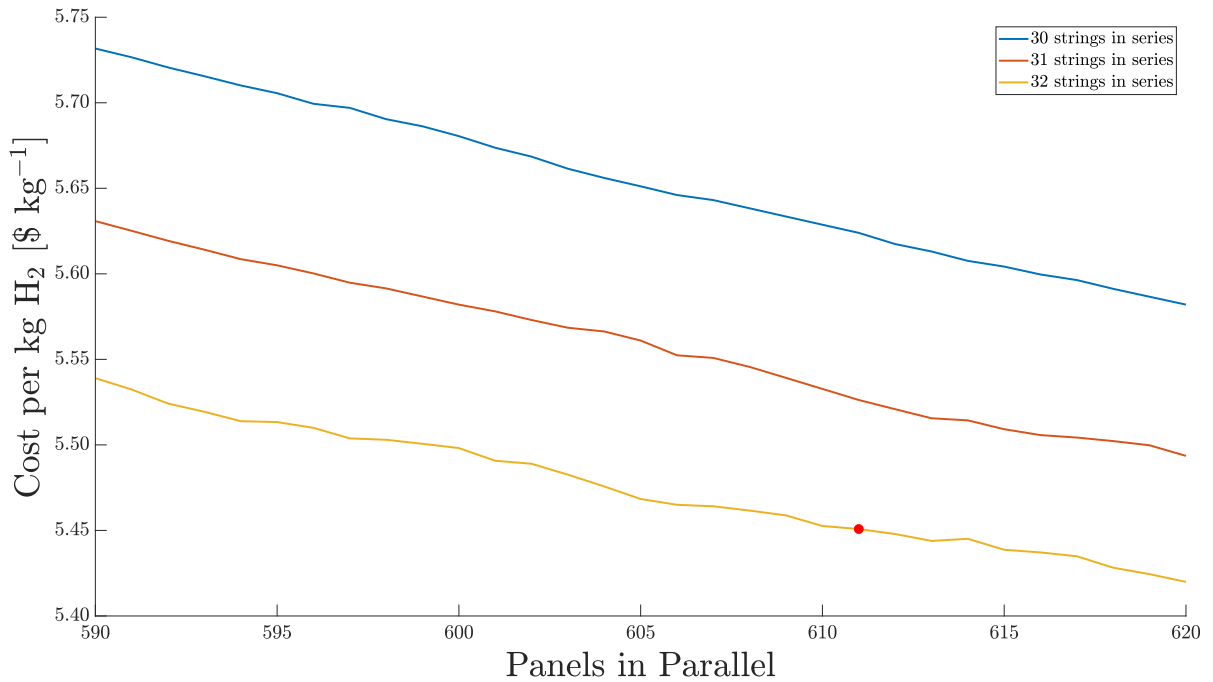


Figure 7.5: Costs for hydrogen production for scenario 2 over the entire system lifetime for one inverter, with the optimum configuration given by the red dot.

Here again we see that the optimum topology uses the maximum number of panels. Ideally this configuration would increase the number of panels used in order to also charge the battery when too much power is produced for the electrolyzers. However, due to the relatively high number of electrolyzers still present it is found that this rarely happens and because the previous scenario already utilizes the maximum number of panels it is not beneficial to add batteries. The power utilized, shown in figure 7.6, again demonstrates the same behaviour as previously seen in figure 7.3.

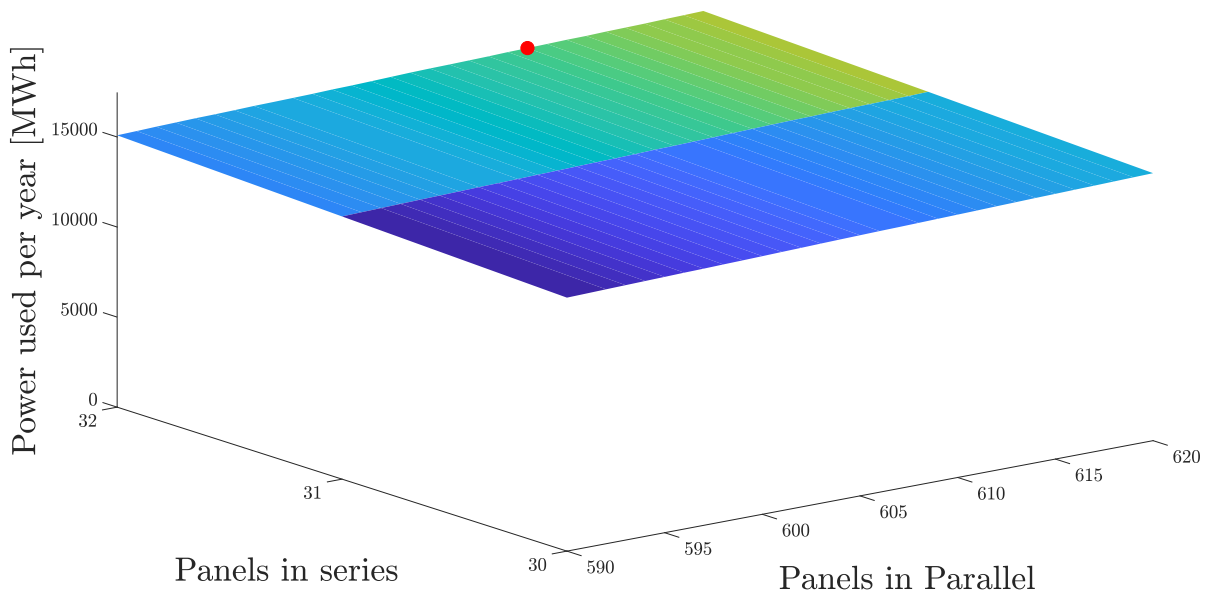


Figure 7.6: Power production from the solar farm using MPPT technology as in scenario 2 for one inverter, with a red dot showing the optimum number of panels.

The lowest price for hydrogen is \$4.39, found at 32 panels in series and 611 strings in parallel, with 6

electrolyzers in series and 19 electrolyzer strings in parallel per plot. This is using a battery of 1 MWh per plot. The number of strings in parallel has decreased due to the increase in CAPEX due to the battery, which shifts the preference to a therefore cheaper PV system. Additionally, adding a battery means that the PV power that is normally wasted can now be used to produce hydrogen. Hence, less panels are needed to reach the same amount of hydrogen. It is possible to vary this along side the system configuration which shows the price dependence on the battery capacity, as shown in figure 7.7.

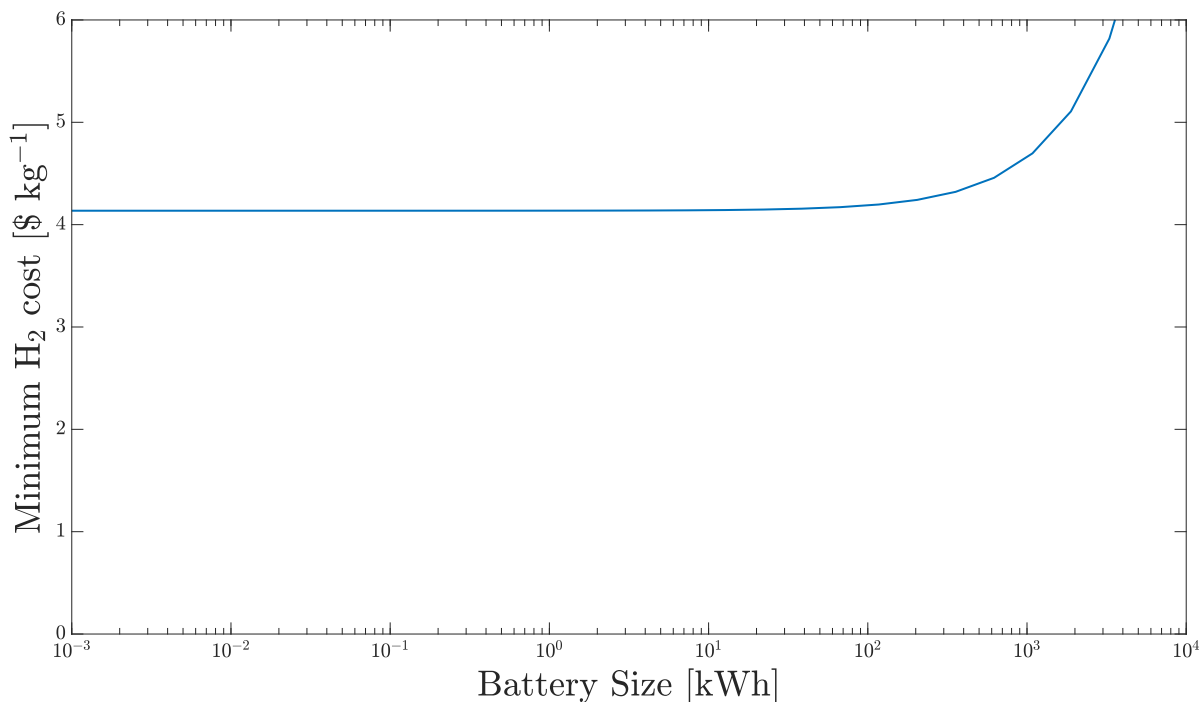


Figure 7.7: Price of hydrogen dependence on battery capacity.

We see here that adding batteries increases the price dramatically and as such, this topology should not be considered a viable or interesting option. It is worth noting that the added value of batteries is mostly present in a more stable H₂ production, but the same can be accomplished by using pipelines as a storage and transfer method between the electrolyzers and the liquefaction plant. In this scenario it is not advisable to omit the hydrogen storage as in order for the battery to replace the gaseous storage the battery must be extremely large, and therefore costly.

7.1.3 Scenario 3: Direct coupling

In this scenario the panels are connected as directly as possible to the electrolyzer, using a method called direct coupling. Here, the panel output power is not optimized but instead the operating point is determined by where the electrolyzer I-V curve meets the solar array I-V curve. In order to power the electrolyzer stack's utility energy demands, a separate and much smaller array must be implemented, together with a small battery system. Using the PV and electrolyzer models described earlier, the following hydrogen production profile is found:

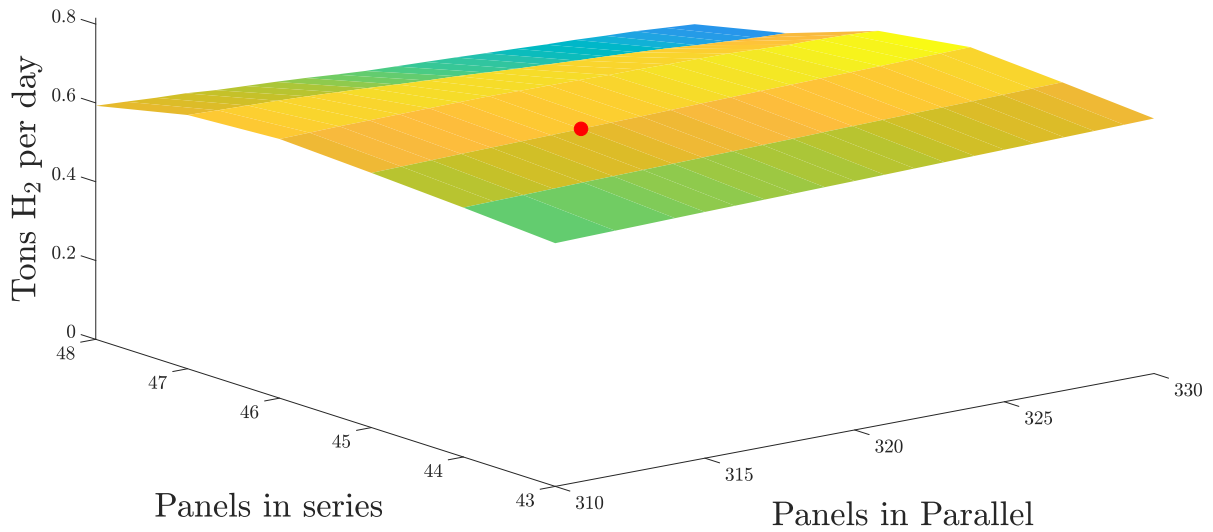


Figure 7.8: Hydrogen production using MPPT technology as in scenario 3 for one busbar, with a red dot showing the optimum number of panels.

Combining this with the economic evaluation framework found in chapter 6 and varying the number of strings in parallel and panels in series as well as the number of electrolyzers in series and parallel, we see the following cost profile form:

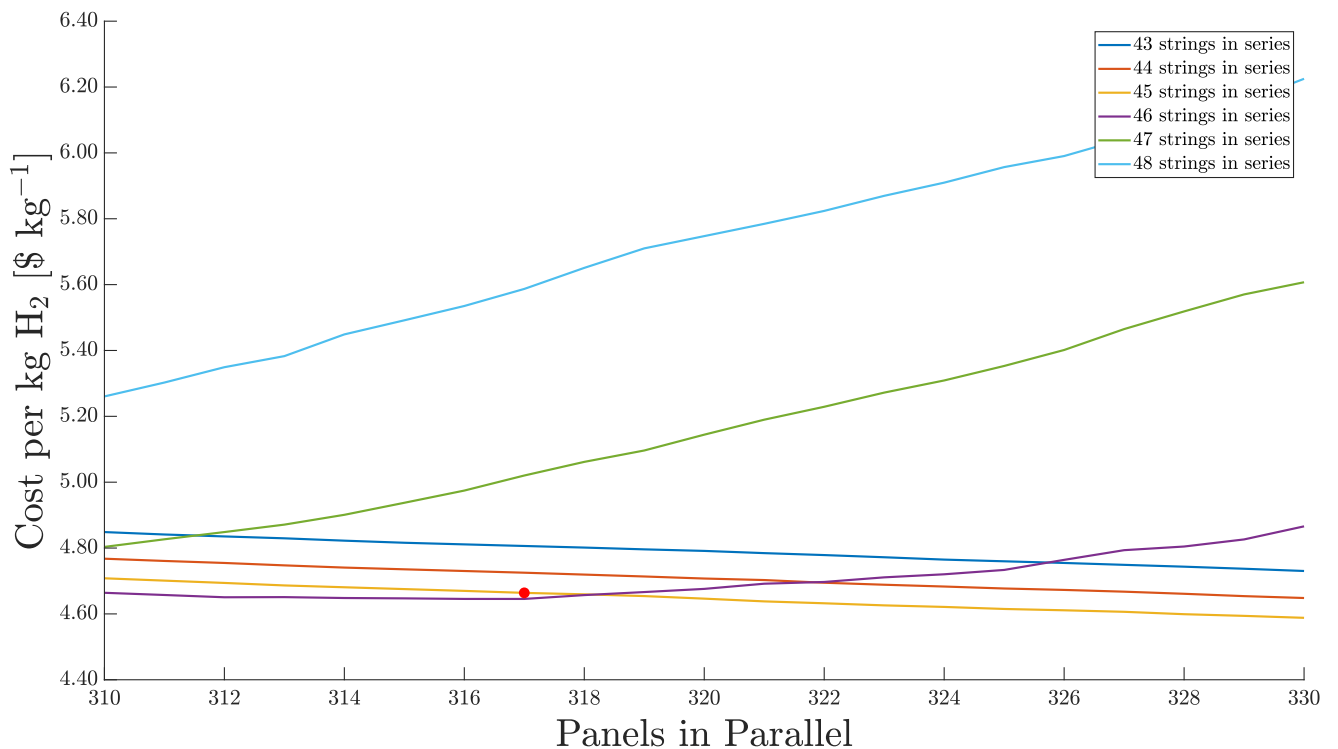


Figure 7.9: Costs for hydrogen production for scenario 3 over the entire system lifetime for one busbar, with the optimum configuration given by the red dot.

We see that fewer panels can be better, as they do not exceed the electrolyzer limits. This can be

seen in the power production graph, shown in figure 7.10. We see here that above a certain point it hardly increases further as otherwise the PV system overloads the inverter.

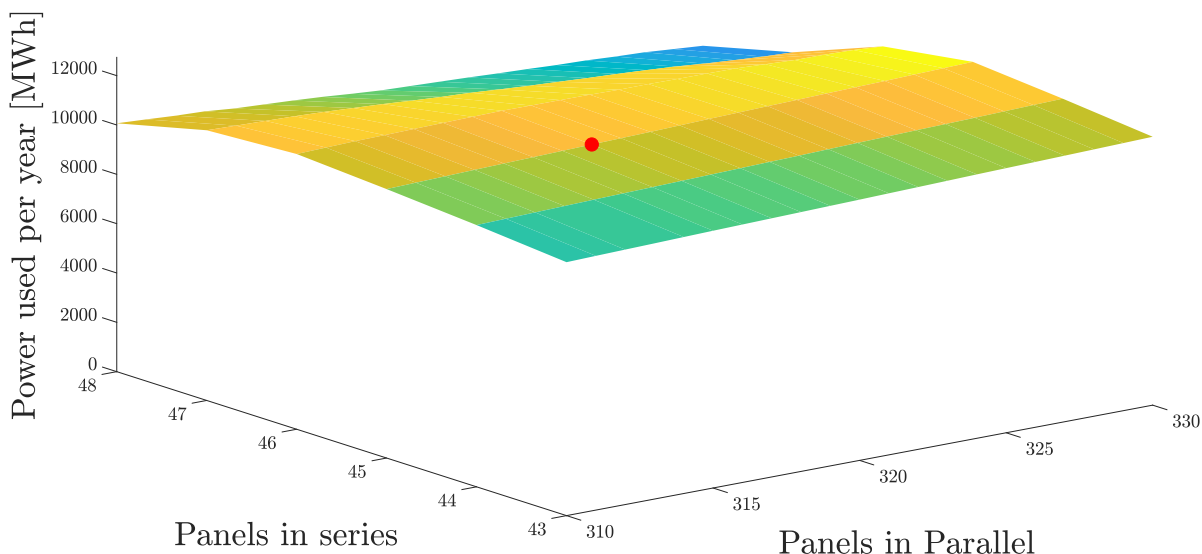


Figure 7.10: Power production from the solar farm using MPPT technology as in scenario 3 for one busbar, with a red dot showing the optimum number of panels.

The lowest price for hydrogen is \$4.02, found at 46 panels in series and 327 strings in parallel, with 15 electrolyzers in series and 5 electrolyzer strings in parallel per busbar.

7.1.4 Scenario comparison

Comparing the results from the three scenarios above we see the following:

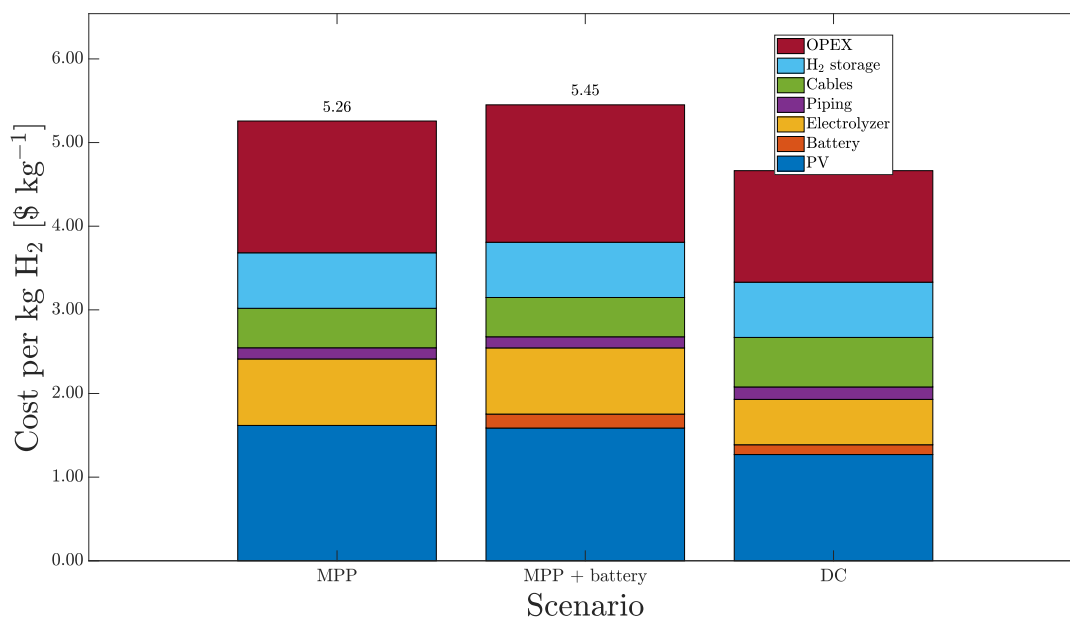


Figure 7.11: Hydrogen cost comparison.

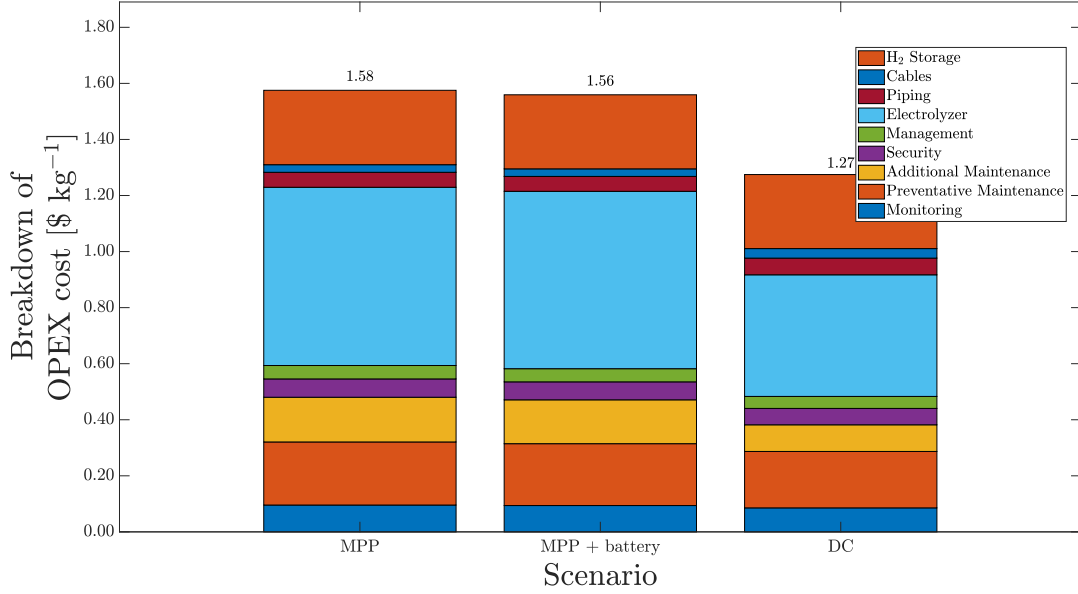


Figure 7.12: OPEX breakdown.

We see here that the third scenario is indeed cheaper, mostly due to the significantly decreased inverter (and battery) costs.

Table 7.1: Optimal plot layout and corresponding H₂ cost.

Scenario	PV		Electrolyzer		Plots	H ₂ cost [\$ kg ⁻¹]
	Series	Parallel	Series	Parallel		
1	32	620	6	19	4	4.16
2	32	611	6	19	4	4.39
3	46	327	15	5	5	4.02

A more detailed analysis of the piping costs will be carried out in section 7.2. These costs have been included in the calculations for table 7.1.

7.2 Layout

Minimizing land usage, the optimal physical layout can now be determined for the MPP and DC scenarios. The battery scenario is not included here due to the effects seen in figure 7.7.

7.2.1 Centralized layout

The following layouts are deemed to be the most interesting for the two scenarios listed above.

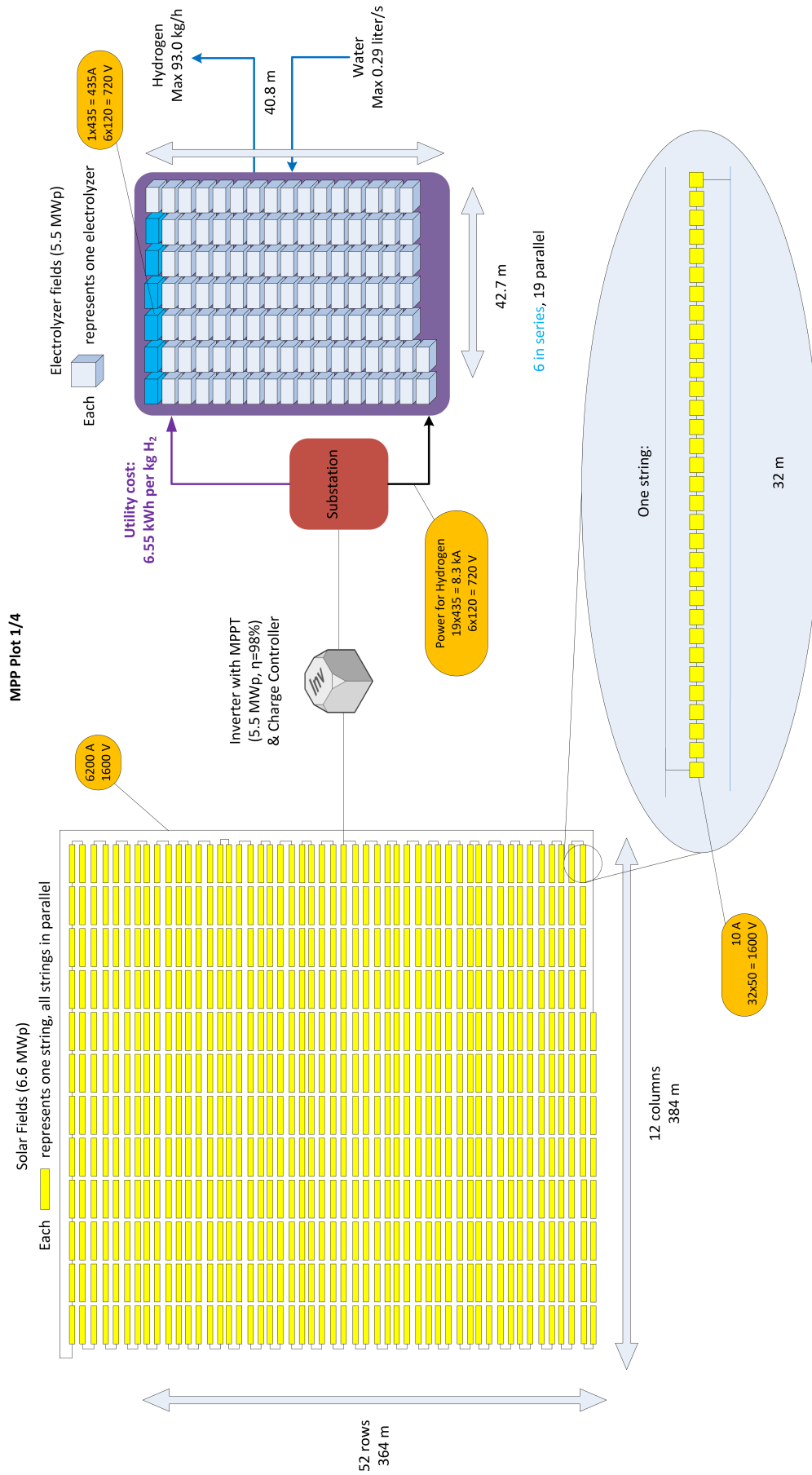


Figure 7.13: MPP optimum layout, with maximum cable specifications given in the yellow text boxes.

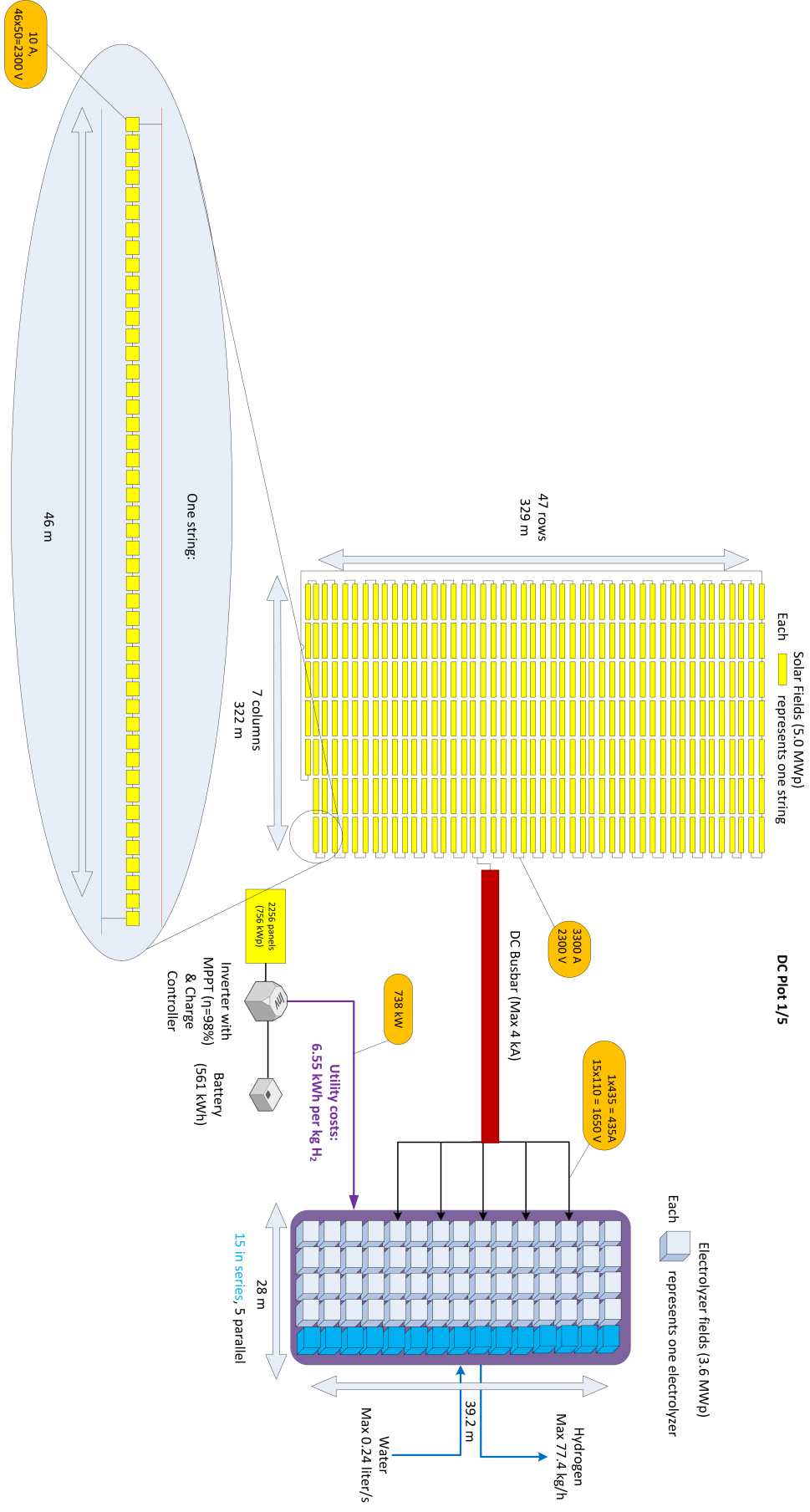


Figure 7.14: DC optimum layout, with maximum cable specifications given in the yellow text boxes.

The layouts above are determined by varying the orientation of the parallel and series strings in order to make the field as square as possible.

There are a number of different pipes required for electrolyzer infeed and outfeed. We assume that cooling water is not needed, and is instead replaced with local air cooling. The different pipes are given along with their specifications below in table 7.2. Each of these pipes also needs a 'header' pipe, or a pipe that connects the pipes between each plot. The specifications of this are given in table 7.3.

Table 7.2: Overview of total in-field piping specifications.

Scenario	Pipe	Length [m]	Pressure [barg]	Min. Diameter [in]
MPP				
	Nitrogen purge	1200	6	0.63
	Instrument air	1200	6	1.38
	Feed water	1200	3	0.53
	Water drain	1200	50	0.38
	Hydrogen	1200	27	0.94
DC				
	Nitrogen purge	1250	6	0.55
	Instrument air	1250	6	1.21
	Feed water	1250	3	0.39
	Water drain	1250	50	0.28
	Hydrogen	1250	27	0.83

The lengths are determined by assuming that all electrolyzer plots are centrally located as shown in figures 7.13 and 7.14, and these plots are located as closely together as possible. The difference in piping lengths is due to the changes in the electrolyzer configuration. Changing the number of electrolyzers in series and parallel results in a different electrolyzer system length and width, meaning that the pipes have a different length. The numbers given above are estimates, in reality the pipe lengths may differ slightly.

Table 7.3: Overview of header piping specifications.

Scenario	Pipe	Material	Length [m]	Pressure [barg]	Min. diameter [in]
MPP					
	Nitrogen purge	Carbon steel	714	6	1.16
	Instrument air	Carbon steel	714	6	2.56
	Feed water	Stainless steel	714	3	0.98
	Water drain	Low alloy (x2021)	714	50	0.69
	Hydrogen	Low alloy (x2021)	714	27	1.73
DC					
	Nitrogen purge	Carbon steel	945	6	1.14
	Instrument air	Carbon steel	945	6	2.52
	Feed water	Stainless steel	945	3	0.81
	Water drain	Low alloy (x2021)	945	50	0.57
	Hydrogen	Low alloy (x2021)	945	27	1.70

Using the pricing estimates calculated using the equations in section 6.5, these specifications are translated to prices as shown in table 7.4.

Table 7.4: Piping CAPEX overview.

Type	Usage	Total price ¹ [kUSD]	
		MPP	DC
In-field piping per plot			
	Nitrogen purge	26.6	23.2
	Instrument air	106.6	93.3
	Feed water	34.3	26.3
	Water drain	66.2	51.4
	Hydrogen	126.5	110.4
Header piping			
	Nitrogen purge	110.5	170.3
	Instrument air	595.1	923.8
	Feed water	144.2	194.4
	Water drain	274.1	368.9
	Hydrogen	591.7	915.3
Total		3165	4096

It is also worth noting that due to a decrease in system matching between PV and electrolyzer systems, we see that the number of panels needed for DC scenario utilities increases. We now need approximately 10,600 panels to run utilities.

7.2.2 Decentralized layout

A separate analysis for a decentralized MPP scenario is not included here, as this would yield mostly the same results. Because each plot size is defined by the maximum size of the inverter and all the power must go through that point, it is illogical to then spread the electrolyzers out throughout the plots. The larger electrolyzer could be replaced with smaller ones, but that would only split the plots up into smaller plots while still making each of these centralized. With smaller inverters the price increases, while the quality of matching between the PV and electrolyzer plots decreases.

For the DC case, this could be interesting as this would essentially split each plot into subplots, each with one string on 15 electrolyzers. Running the optimization tool again, we find that 46 panels in series and 66 strings in parallel are needed. This would also change some of the cable and piping characteristics and lengths, as shown below in table 7.5. The layout is shown in figure 7.15.

Table 7.5: Decentralized DC piping CAPEX.

Type	Usage	Total system length [m]	Total price [kUSD]
In-field piping per plot			
	Nitrogen purge	4200	13.1
	Instrument air	4200	47.4
	Feed water	4200	7.4
	Water drain	4200	4.4
	Hydrogen	4200	54.7
Header piping			
	Nitrogen purge	4350	51.2
	Instrument air	4350	259.8
	Feed water	4350	28.5
	Water drain	4350	75.7
	Hydrogen	4350	266.5
Total			4492

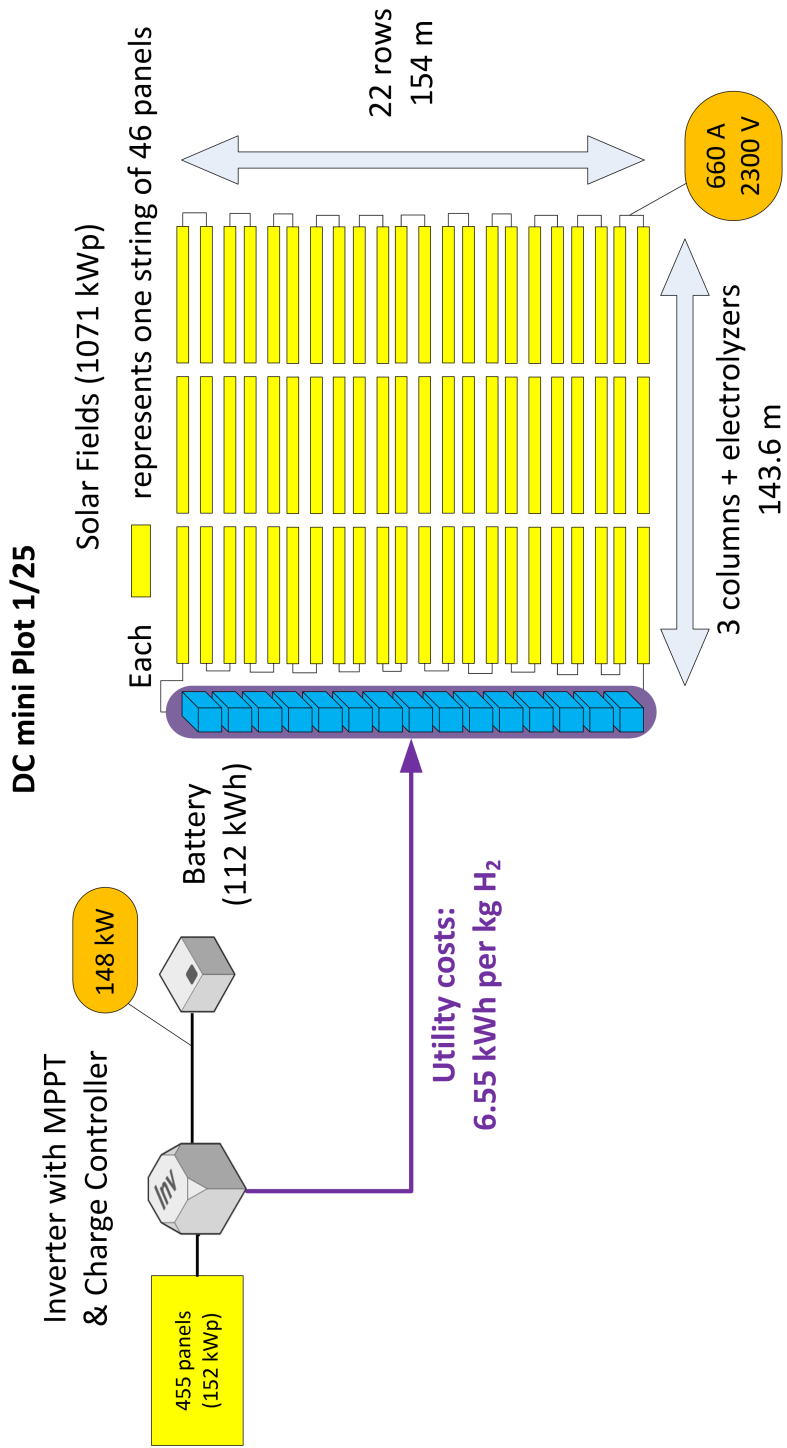


Figure 7.15: Decentralized DC optimum layout.

When running the optimization the base price for hydrogen, including all these components, is 4.09 USD per kg hydrogen. This is higher than the centralized DC scenario due to the decrease in matching between the PV and electrolyzer systems, as shown below.

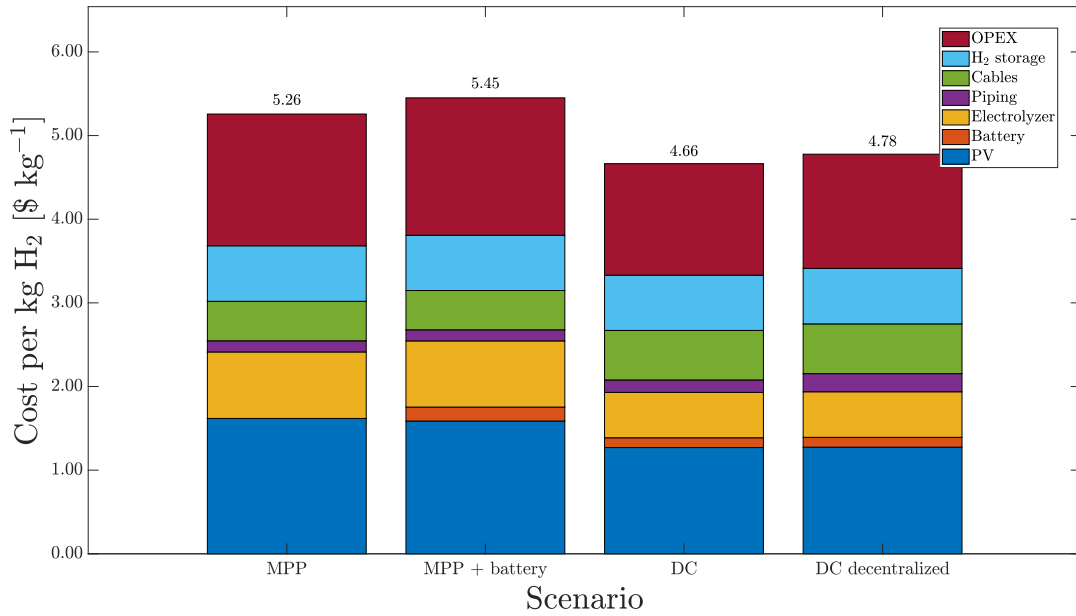


Figure 7.16: Hydrogen cost comparison (including decentralized DC).

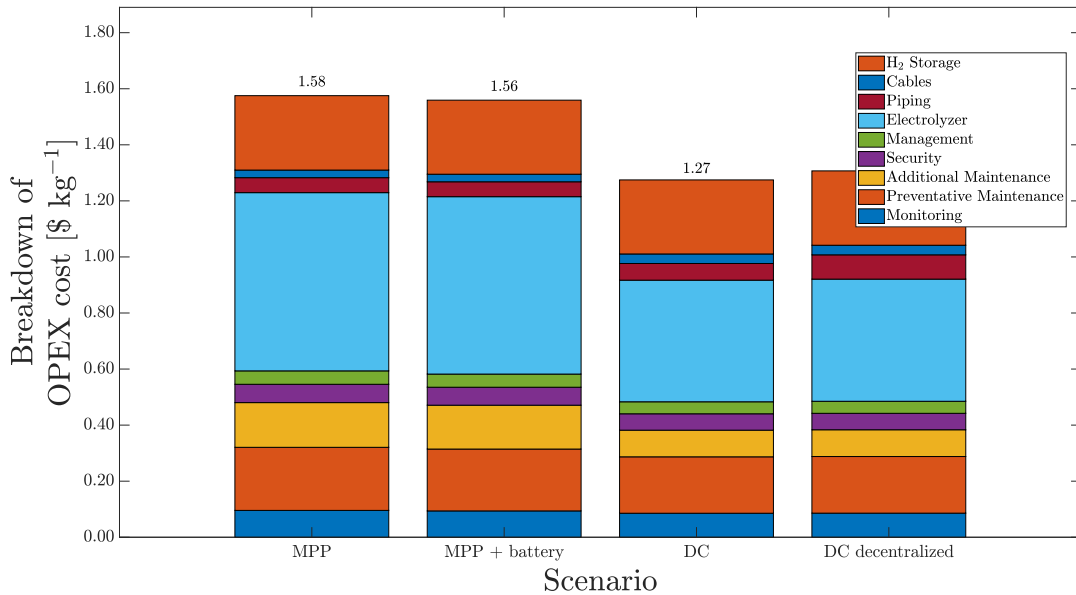


Figure 7.17: OPEX breakdown (including decentralized DC).

It is also interesting to look at some other metrics for the different scenarios. Namely, looking at the average specific energy demand we see that the DC scenario does need more power per kg of hydrogen produced, due to the extra solar field being underutilized at times. This causes power to be wasted, meaning a higher energy demand.

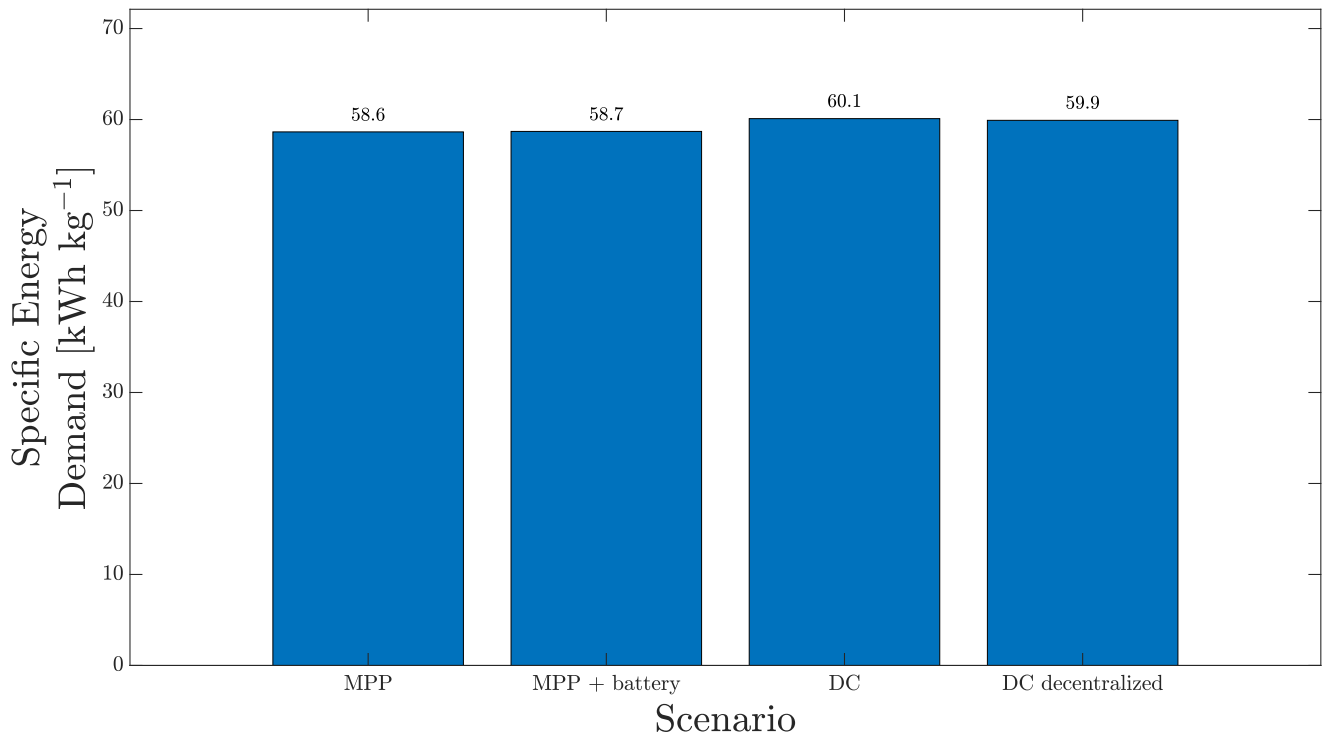


Figure 7.18: Specific energy demand comparison.

This is again reflected in the production of hydrogen per W_p of solar power installed, as shown below in figure 7.19. We see here that the DC scenarios produce less hydrogen per panel due to the inefficient usage of the utility PV field.

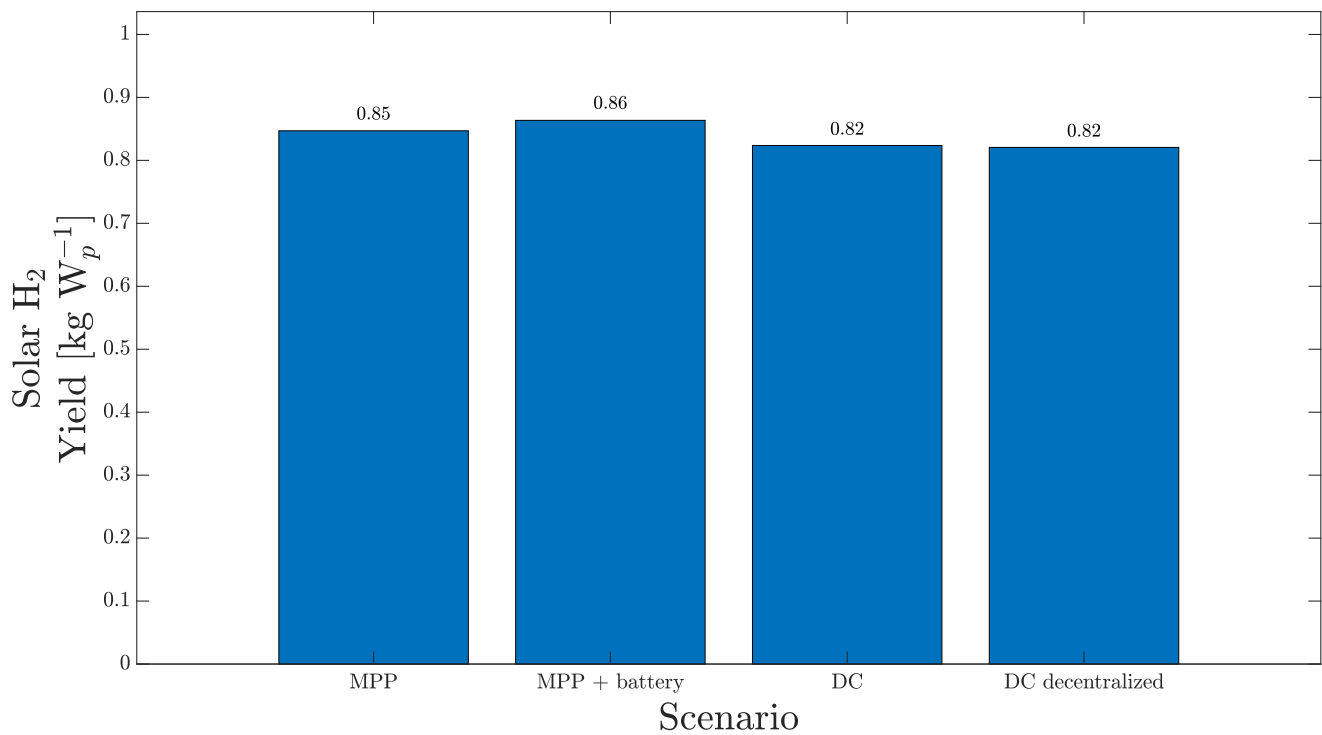


Figure 7.19: Comparison of lifetime hydrogen production per W_p of solar power installed.

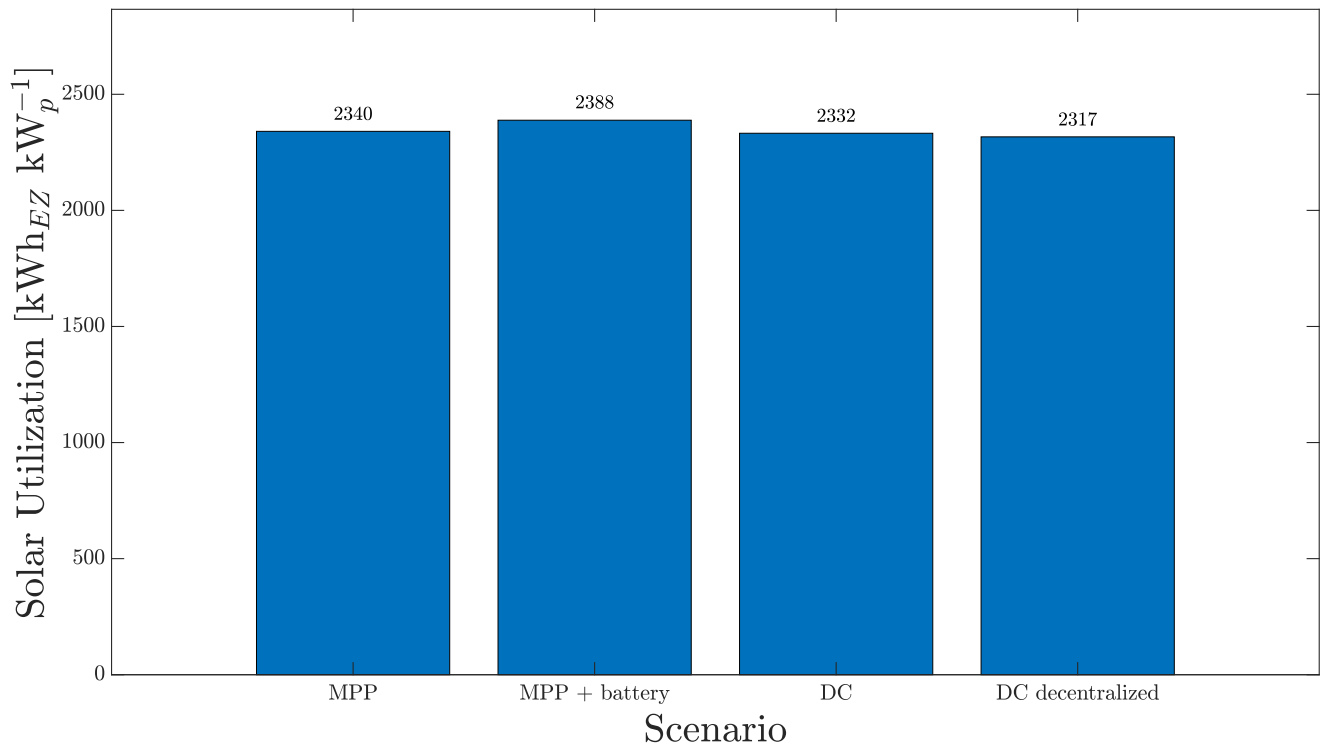
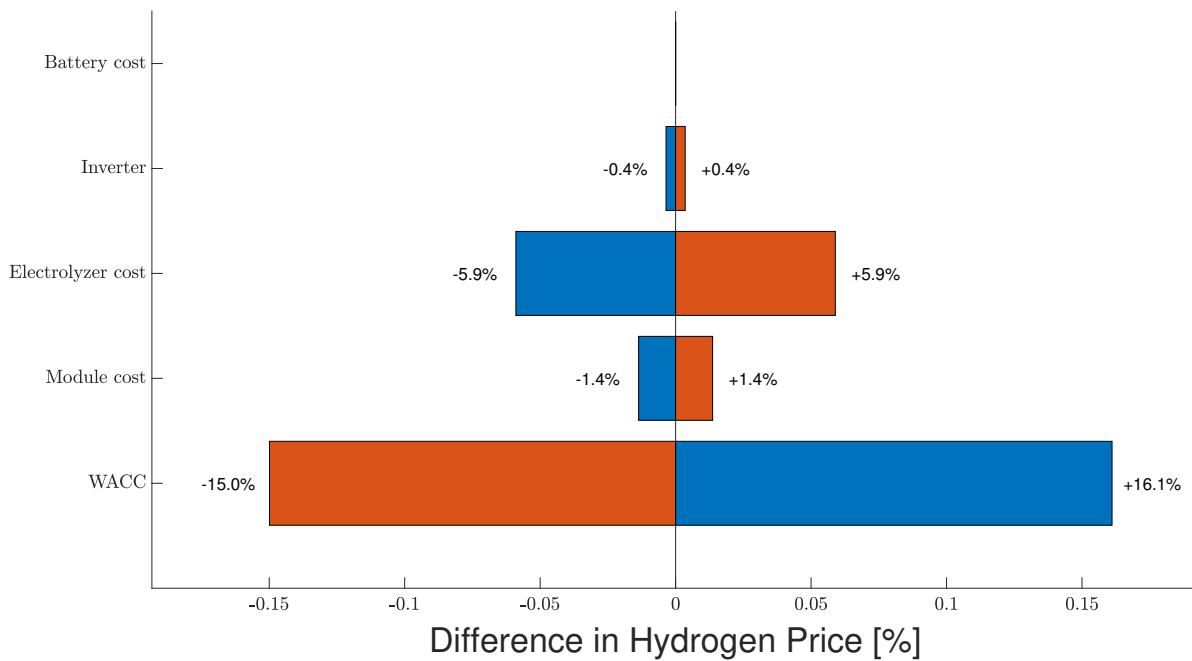


Figure 7.20: Comparison of usable solar energy generated per W_p installed.

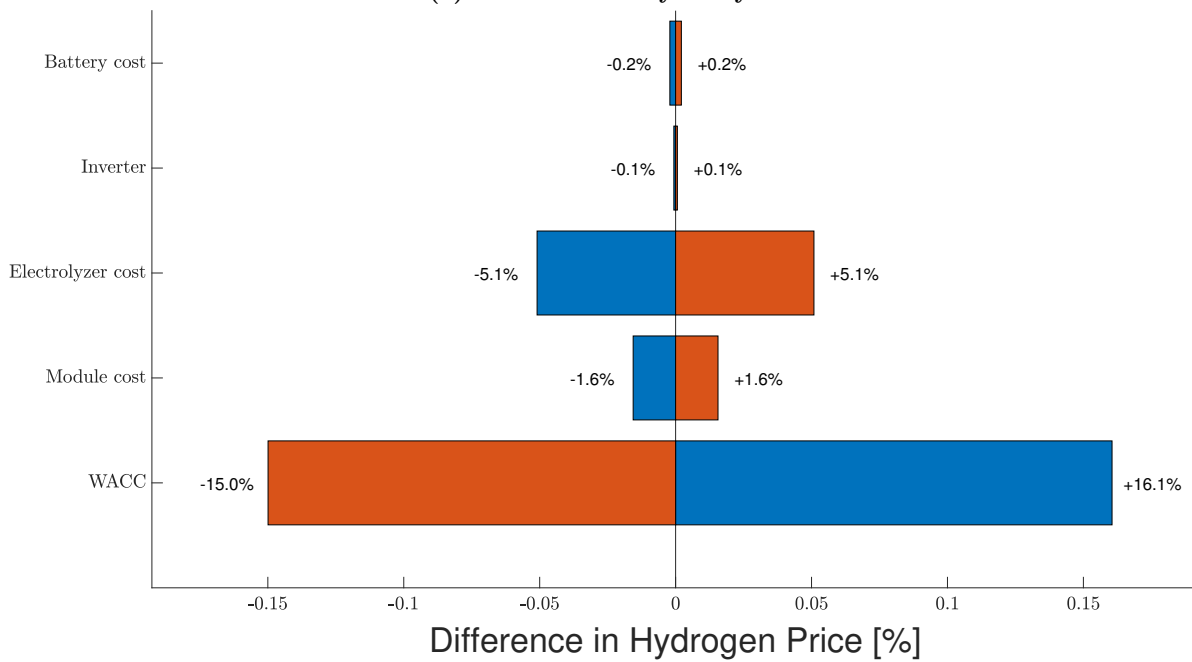
Finally, looking at the solar utilization we see that the MPP scenario is indeed the most efficient at producing usable energy and therefore has the optimal power usage between the PV and electrolyzer systems. The increase when adding a battery is due to the ability to do peak-shaving which allows more energy to be used. Furthermore, the difference between the decentralized and centralized DC topologies is caused by a slight decrease between the PV and the electrolyzer system matching.

7.3 Sensitivity Analysis

In order to see how the price changes for the two most attractive scenarios (MPP and centralized DC) a sensitivity analysis may be carried out. Varying the WACC, PV module price, electrolyzer price, inverter price, or battery price we see the following:



(a) MPP sensitivity analysis



(b) DC sensitivity analysis

Figure 7.21: Sensitivity analysis with the WACC at 0.5 and 0.9 (default 0.7), and the PV, electrolyzer, inverter and battery prices varied from 90% to 110% of the current values.

We see that the prices of hydrogen are most sensitive to the cost of capital. Furthermore, it is found that if the inverter price would decrease by 65% then the DC and MPP scenarios have the same price. Furthermore, if the battery price were to increase by 110% then the DC and MPP scenarios would again have the same hydrogen price.

7.4 Ramping

As discussed earlier, alkaline electrolyzers cannot respond immediately to changes in voltage and a quick increase or decrease in load could damage the electrolyzer. A more complex model such as in [50] could include the ramping limits. These ramping calculations have been done for the optimal system found in section 7.1.1 for scenario 1. All voltages given in this section are per electrolyzer.

The maximum ramping seen in this system for the MPP scenario and the DC scenario was seen on the 27th of February at 12:11 and the 29th of January at 5:33 respectively, using equations 5.2 and 5.3. The changes in operating point are visualized below in figure 7.22.

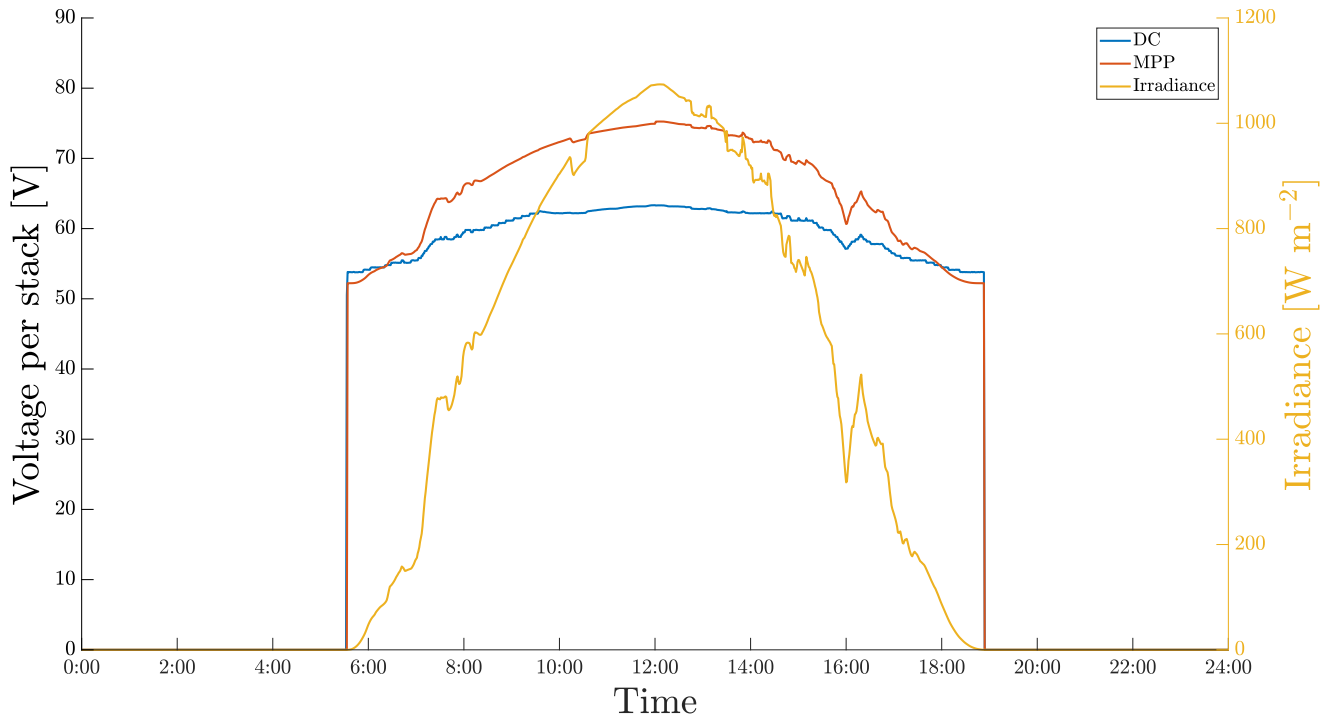


Figure 7.22: Voltage changes due to changing environmental conditions on a minute time scale.

The figure above illustrates the quickest voltage change, from 63.1 to 64.6 V per electrolyzer for the MPP scenario, which equates to a change of 1.5 V/min upwards. Looking at downwards ramping in the MPP scenario the steepest ramp is -1.5 V/min, from 57.6 to 56.1 V. For the DC scenario the largest increase in voltage was from 50.5 V to 53.8 V per electrolyzer, which equates to a change of 3.3 V/min. Looking at downwards ramping this was -3.3 V/min, from 53.8 V to 50.5 V. These are all within the allowed ramping margins of electrolyzers. It is also interesting to see that the DC scenario voltage changes more than the MPP scenario, as one would expect due to the sensitivity of the operating point with respect to the shape of the photovoltaic I-V curve. An overview of these results is given in table 7.6.

In section 5.2 it was also decided to simulate the operating points with all V_{oc} 's and I_{sc} 's shifted downwards to offset the variation seen in figure 5.2. The maximum ramping seen in this system for the MPP scenario was seen at 11:56 on January 16th. For the DC scenario this was found to be on April 19th at 17:35. The changes in operating point are visualized below in figure 7.23.

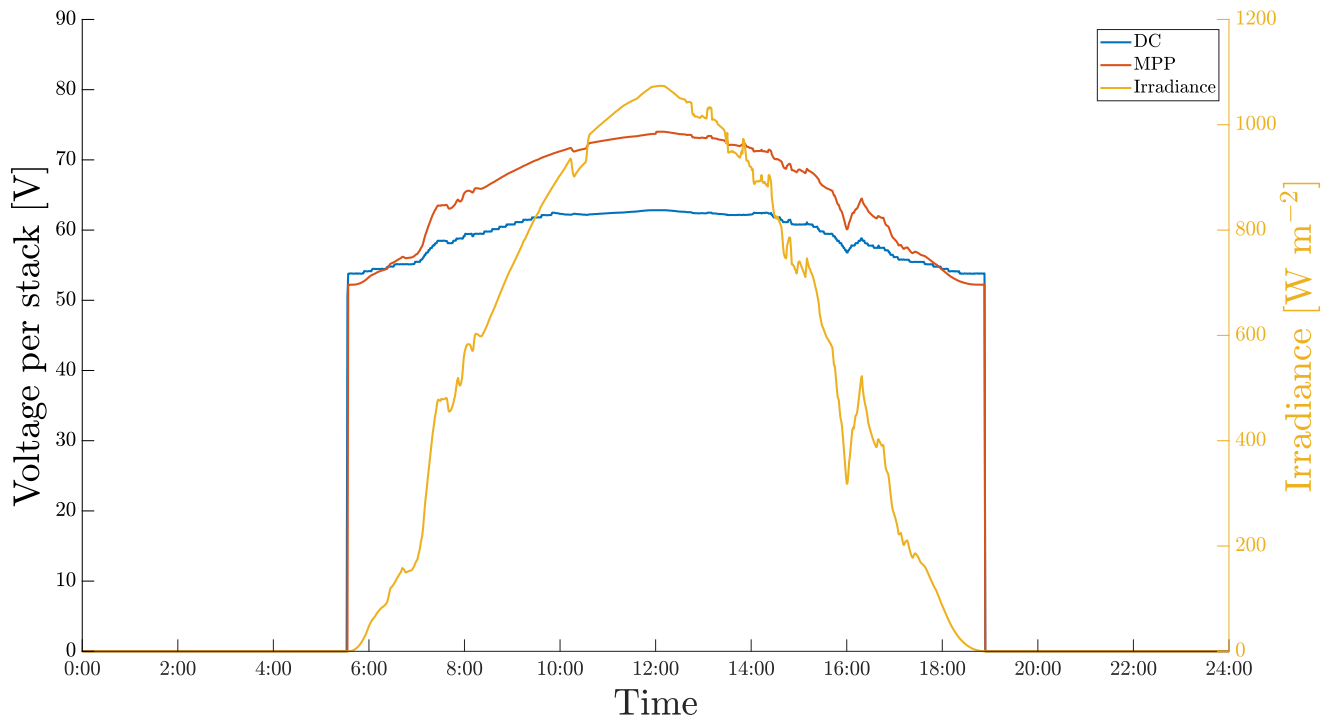


Figure 7.23: Voltage changes due to changing environmental conditions on a minute time scale.

In the MPP scenario the maximum upward ramping speed is 1.4 V/s from 62.4 to 63.8 V. Downwards the maximum ramping speed is -1.4 V/s. For the DC scenario the maximum and downward ramping speeds are 3.3 V/s and -3.3 V/s, respectively. This is well within the limits set by electrolyzer manufacturers. An overview of these results is given in table 7.6.

Table 7.6: Overview of the ramping results

I_{sc} & V_{oc}	DC		MPP	
	Upwards [ΔV]	Downwards [ΔV]	Upwards [ΔV]	Downwards [ΔV]
Original	3.3	-3.3	1.5	-1.5
Shifted	3.3	-3.3	1.4	-1.4

In section 5.2 it was explained how an electrolyzer should ideally not ramp up faster than 10% of its maximum power per second, and down no faster than 20% per second. If we assume that the operating point of the electrolyzers does not rapidly change per second but instead that they operate linearly between each minute, we find that the electrolyzers do not ramp above their safety limits.

Chapter 8

Summary and recommendations

Hydrogen is and will continue to be a key molecule of interest for the future energy transition as a dense energy carrier and fuel, capable of moving energy efficiently over long distances. In order to allow renewable hydrogen to compete on a cost basis with fossil based hydrogen, significant cost reductions are required, primarily in the systems components implemented. Power electronics have been identified as significant contributors, with rectifiers, transformers and inverters accounting for up to 25% of PV system costs and 30% of electrolyzer costs.

Photovoltaic technologies are playing an increasingly large role in the energy transition of humanity moving towards a greener future. By combining this with electrolysis it is possible to create truly green hydrogen, where no carbon dioxide or other greenhouse gasses are emitted.

In this report it has been shown that the centralized direct coupling scenario is the most cost effective way of producing hydrogen. This method reduces costs by decreasing cable lengths, while still matching the PV and electrolyzer I-V curves. A total cost of \$4.02 USD per kg hydrogen is found. This price excludes the costs of liquefaction, land costs, and purification of hydrogen and water. **Based on this, it is advised to use a decentralized topology, combined with a decentralized layout consisting of multiple smaller plots.** Although the centralized layout is slightly cheaper, it contains more system critical components which could cause a large portion of the system to be inactive if they are broken.

It was also shown that the ramping speeds found here, based on minute-by-minute data, are within the maximum ramping speeds allowed for this type of alkaline electrolyzer. If higher ramping speeds would have been found then it would have been advisable to switch to electrolyzers that can respond quicker, like PEM electrolyzers.

It was furthermore found that electrolyzer degradation caused a 5.8% decrease on average of hydrogen production. This was then applied as a constant factor to ensure that the hydrogen production reflected the average production. In reality electrolyzer degradation would cause the electrolyzer system to be slightly smaller, so that during its lifetime the I-V curve would shift to the right and would match better. The addition of PV degradation would also cause the matching between the PV and electrolyzer systems to increase during their lifetime although this was not included here due to PV replacement being included in the OPEX corresponding to the photovoltaic system.

There are a number of additional aspects in which this research could be extended. By not relying on hourly data but instead data collected minute-by-minute, the accuracy of this model could significantly increase. However, this increases the computation time by almost a factor of 60 and requires more memory.

Currently the solar profile uses a monofacial panel, as PVsyst cannot correctly model a bifacial solar profile. As bifacial and tracking technologies become more and more accessible, their market penetration is expected to increase significantly. It is therefore advisable to exchange the PVsyst monofacial profile with a single axis tracking bifacial profile. However, at the time of publishing there were very few proven bifacial profiles available, let alone ones with single axis tracking.

Furthermore, it is still unclear whether PV_{syst} includes factors such as mist and weather uncertainties. It is very reasonable to say that the largest uncertainty in this report lies not within the calculations or models themselves but in the meteorological data on which everything builds.

The total power generated in the reconstructed case has a systematic error of +0.8% compared to the values PV_{syst} gives. The consequence of the slightly higher reconstructed voltages is that the power production is also slightly higher than what is predicted by PV_{syst}, increasing the time the electrolyzers can operate slightly.

8.1 Out of scope

A number of elements were deemed out of the scope of this investigation. These are given below, with relevant papers listed afterwards.

- PV
 - The performance of solar panels and temperature dependencies for power are frequently material dependent [40]. It may be interesting to see what the heat in Australia does to characteristics like lifetime of the PV system.
 - The heat in Australia is a serious concern, so it is also interesting to investigate the feasibility of using the infeed water to the electrolyzers to cool off the PV panels, while heating up the infeed water [6, 49, 72, 73, 83].
- System
 - Replacing the battery with a grid connection could allow for a more resilient system, at the cost of a higher system cost.
 - No scenario was modelled which combines direct coupling and batteries, as then system components should be reintroduced to facilitate the battery connection.
 - No modelling was done around a water and hydrogen purification step. The model could be expanded such that these elements are included.
 - Model the liquefaction plant and look at momentary hydrogen production instead of average. This could verify the need for a large hydrogen storage system.
 - Batteries were included in this investigation for the DC scenario as the electrolyzer utilities should still be able to run when the weather is poor. In reality it may be interesting to replace these batteries with diesel generators. This was deemed out of the scope of this report as the goal was to make 100% green hydrogen. In reality however this would decrease the costs of the DC scenario further.
 - No extra precautions were taken in maintaining a backup of materials and components. Normally a reserve of system critical components are kept close by so that components like large central inverters or pumps can be replaced quickly, in order to reduce overall system downtime. This was not included in this investigation as it was not clear which components need to be quickly replaced, and which components are more readily available.
 - The downtime for cleaning is not included in the PV simulation, as it is assumed that the effect of a single panel being cleaned will not have a large effect.

8.2 Suggestions for further research

From this research a number of topics come forward as possible follow up areas for investigation. In the list below these topics are given, along with some relevant papers.

- Experimental validation of the model.

- Verify electrolyzer lower and upper hydrogen production threshold, as well as degradation and lifetime [10, 79].
- Replace the experimental electrolyzer model with experimental data such as given by [2, 33].
- Investigate what intermittency does to an electrolyzer [87, 99].
- Investigate the effects of ramping with real module temperature and wind data instead of using the models used here.
- Vary electrolyzer types and models (different suppliers or use different technology all together) and see how that effects hydrogen production.
- Investigate how much electrolyzers cool down overnight to verify the linear constant temperature electrolyzer model given in section 2.1.

Bibliography

- [1] Abdelkader Abbassi, Rabiaa Gammoudi, Mohamed Ali Dami, Othman Hasnaoui, and Mohamed Jemli. An improved single-diode model parameters extraction at different operating conditions with a view to modeling a photovoltaic generator: A comparative study. *Solar Energy*, 155: 478–489, 2017.
- [2] Z Abdin, CJ Webb, and E MacA Gray. Modelling and simulation of an alkaline electrolyser cell. *Energy*, 138:316–331, 2017.
- [3] Piergiorgio Alotto, Massimo Guarnieri, and Federico Moro. Redox flow batteries for the storage of renewable energy: A review. *Renewable and Sustainable Energy Reviews*, 29:325–335, 2014.
- [4] Wade A Amos. Costs of storing and transporting hydrogen. Technical report, National Renewable Energy Lab., Golden, CO (US), 1999.
- [5] Petros J Axaopoulos, Emmanouil D Fylladitakis, and Konstantinos Gkarakis. Accuracy analysis of software for the estimation and planning of photovoltaic installations. *International Journal of Energy and Environmental Engineering*, 5(1):1, 2014.
- [6] H Bahaidarah, Abdul Subhan, P Gandhidasan, and S Rehman. Performance evaluation of a pv (photovoltaic) module by back surface water cooling for hot climatic conditions. *Energy*, 59: 445–453, 2013.
- [7] Ashraf Balabel and Mohamed S Zaky. Experimental investigation of solar-hydrogen energy system performance. *international journal of hydrogen energy*, 36(8):4653–4663, 2011.
- [8] Frano Barbir. PEM electrolysis for production of hydrogen from renewable energy sources. *Solar energy*, 78(5):661–669, 2005.
- [9] H Bayhan and M Bayhan. A simple approach to determine the solar cell diode ideality factor under illumination. *Solar Energy*, 85(5):769–775, 2011.
- [10] Luca Bertuccioli, Alvin Chan, David Hart, Franz Lehner, Ben Madden, and Eleanor Standen. Development of water electrolysis in the european union. *Fuel Cells and Hydrogen Joint Undertaking*, page 83, 2014.
- [11] Ramchandra Bhandari, Clemens A Trudewind, and Petra Zapp. Life cycle assessment of hydrogen production via electrolysis—a review. *Journal of cleaner production*, 85:151–163, 2014.
- [12] Noriah Bidin, Siti Radhiana Azni, M Azat Abu Bakar, Abd Rahman Johari, Daing Hanum Farhana Abdul Munap, M Farizuddin Salebi, Siti Noraiza Abd Razak, Nur Syahirah Sahidan, and Siti Nur Aqilah Sulaiman. The effect of sunlight in hydrogen production from water electrolysis. *International Journal of Hydrogen Energy*, 42(1):133–142, 2017.
- [13] Dmitrii Bogdanov, Ashish Gulagi, and Christian Breyer. Pv generation share in the energy system and battery utilisation correlation in a net zero emission world. In *6th Solar Integration Workshop, Vienna*, 2016.
- [14] James R Bolton. Solar photoproduction of hydrogen: a review. *Solar energy*, 57(1):37–50, 1996.

- [15] BP. Solar energy statistical review. Website. <https://www.bp.com/en/global/corporate/energy-economics/statistical-review-of-world-energy/renewable-energy/solar-energy.html>, 2016.
- [16] Christian Breyer, Michael Child, Otto Koskinen, and B Dmitrii. A low-cost power system for europe based on renewable electricity. *Proceedings of the European Utility Week, Barcelona, Spain*, pages 15–17, 2016.
- [17] Séverine Busquet, Charles-Emile Hubert, Julien Labbe, Didier Mayer, and Rudolf Metkemeijer. A new approach to empirical electrical modelling of a fuel cell, an electrolyser or a regenerative fuel cell. *Journal of Power Sources*, 134(1):41–48, 2004.
- [18] Alexander Buttler and Hartmut Spliethoff. Current status of water electrolysis for energy storage, grid balancing and sector coupling via power-to-gas and power-to-liquids: A review. *Renewable and Sustainable Energy Reviews*, 2017.
- [19] Hayrettin Can, Damla Ickilli, and Koray Sener Parlak. A new numerical solution approach for the real-time modeling of photovoltaic panels. In *Power and Energy Engineering Conference (APPEEC), 2012 Asia-Pacific*, pages 1–4. IEEE, 2012.
- [20] Luz Elena Peñaranda Chenche, Oscar Saul Hernandez Mendoza, and Enio Pedone Bandarra Filho. Comparison of four methods for parameter estimation of mono-and multi-junction photovoltaic devices using experimental data. *Renewable and Sustainable Energy Reviews*, 2017.
- [21] Haejun Chung, Xingshu Sun, Aditya D Mohite, Rahul Singh, Lokendra Kumar, Muhammad A Alam, and Peter Bermel. Modeling and designing multilayer 2d perovskite/silicon bifacial tandem photovoltaics for high efficiencies and long-term stability. *Optics Express*, 25(8):A311–A322, 2017.
- [22] Rebecca E Ciez and JF Whitacre. Comparative techno-economic analysis of hybrid micro-grid systems utilizing different battery types. *Energy Conversion and Management*, 112:435–444, 2016.
- [23] R de Boer. *Technologies and Prospects for Photochemical Conversion and Storage of Solar Energy: A survey of the state-of-the-art*. Netherlands Energy Research Foundation, 2001.
- [24] Chris Deline, Bill Marion, Jennifer Granata, and Sigifredo Gonzalez. Performance and economic analysis of distributed power electronics in photovoltaic systems. Technical report, National Renewable Energy Laboratory (NREL), Golden, CO., 2011.
- [25] Tamunosaki Graham Douglas, Andrew Cruden, and David Infield. Development of an ambient temperature alkaline electrolyser for dynamic operation with renewable energy sources. *International Journal of Hydrogen Energy*, 38(2):723–739, 2013.
- [26] J Eichman, K Harrison, and Michael Peters. Novel electrolyzer applications: providing more than just hydrogen. Technical report, National Renewable Energy Laboratory (NREL), Golden, CO., 2014.
- [27] K Et-torabi, I Nassar-eddine, A Obbadi, Y Errami, R Rmaily, S Sahnoun, M Agunaou, et al. Parameters estimation of the single and double diode photovoltaic models using a gauss–seidel algorithm and analytical method: A comparative study. *Energy Conversion and Management*, 148:1041–1054, 2017.
- [28] Mahdi Fasihi, Dmitrii Bogdanov, and Christian Breyer. Economics of global lng trading based on hybrid pv-wind power plants. In *Proceedings of the 31st European Photovoltaic Solar Energy Conference (EU PVSEC), Hamburg, Germany*, pages 14–18, 2015.
- [29] Hassan Fathabadi. Novel high efficiency dc/dc boost converter for using in photovoltaic systems. *Solar Energy*, 125:22–31, 2016.
- [30] Janine Freeman, Jonathan Whitmore, Nate Blair, and Aron P Dobos. Validation of multiple tools for flat plate photovoltaic modeling against measured data. In *Photovoltaic Specialist Conference (PVSC), 2014 IEEE 40th*, pages 1932–1937. IEEE, 2014.

-
- [31] Jason C Ganley. High temperature and pressure alkaline electrolysis. *International journal of hydrogen energy*, 34(9):3604–3611, 2009.
- [32] R Garcia-Valverde, C Miguel, R Martínez-Béjar, and A Urbina. Optimized photovoltaic generator–water electrolyser coupling through a controlled dc–dc converter. *International Journal of Hydrogen Energy*, 33(20):5352–5362, 2008.
- [33] R García-Valverde, N Espinosa, and A Urbina. Optimized method for photovoltaic-water electrolyser direct coupling. *international journal of hydrogen energy*, 36(17):10574–10586, 2011.
- [34] Thomas L Gibson and Nelson A Kelly. Predicting efficiency of solar powered hydrogen generation using photovoltaic-electrolysis devices. *International journal of hydrogen energy*, 35(3):900–911, 2010.
- [35] Agata Godula-Jopek. *Hydrogen production: by electrolysis*. John Wiley & Sons, 2015.
- [36] Brian Goss, Ian Cole, Thomas Betts, and Ralph Gottschalg. Irradiance modelling for individual cells of shaded solar photovoltaic arrays. *Solar Energy*, 110:410–419, 2014.
- [37] R Guerrero-Lemus, R Vega, Taehyeon Kim, Amy Kimm, and LE Shephard. Bifacial solar photovoltaics—a technology review. *Renewable and Sustainable Energy Reviews*, 60:1533–1549, 2016.
- [38] MA Hamdy and RL Call. The effect of the diode ideality factor on the experimental determination of series resistance of solar cells. *Solar Cells*, 20(2):119–126, 1987.
- [39] Mohammad A Hannan, MSH Lipu, A Hussain, and A Mohamed. A review of lithium-ion battery state of charge estimation and management system in electric vehicle applications: Challenges and recommendations. *Renewable and Sustainable Energy Reviews*, 78:834–854, 2017.
- [40] M Hasanuzzaman, ABMA Malek, MM Islam, AK Pandey, and NA Rahim. Global advancement of cooling technologies for pv systems: A review. *Solar Energy*, 137:25–45, 2016.
- [41] William Hayes, Alex Panchula, and Lauren Nelson. Thermal modeling accuracy of hourly averaged data for large free field cadmium telluride pv arrays. In *Photovoltaic Specialists Conference (PVSC), Volume 2, 2012 IEEE 38th*, pages 1–4. IEEE, 2012.
- [42] Andreas Hübner, Armin G Aberle, and Rudolf Hezel. Novel cost-effective bifacial silicon solar cells with 19.4% front and 18.1% rear efficiency. *Applied physics letters*, 70(8):1008–1010, 1997.
- [43] Ali M Humada, Mojgan Hojabri, Saad Mekhilef, and Hussein M Hamada. Solar cell parameters extraction based on single and double-diode models: A review. *Renewable and Sustainable Energy Reviews*, 56:494–509, 2016.
- [44] Hydrogenics. Electrolyzer datasheet. Information obtained via Jeff Martin, 2018.
- [45] IEA. Medium Term Market Report. *International Energy Agency: Paris, France*, 2016.
- [46] Olindo Isabella, Arno Smets, Klaus Jäger, Miro Zeman, and Rene van Swaaij. *Solar Energy: The Physics and Engineering of Photovoltaic Conversion, Technologies and Systems*. UIT Cambridge, 2016. ISBN 9781906860325.
- [47] Carles Jaen, Cristian Moyano, Xavier Santacruz, Josep Pou, and Antoni Arias. Overview of maximum power point tracking control techniques used in photovoltaic systems. In *Electronics, Circuits and Systems, 2008. ICECS 2008. 15th IEEE International Conference on*, pages 1099–1102. IEEE, 2008.
- [48] Amit Jain and Avinashi Kapoor. Exact analytical solutions of the parameters of real solar cells using lambert w-function. *Solar Energy Materials and Solar Cells*, 81(2):269–277, 2004.
- [49] Sanjeev Jakhar and Manoj S Soni. Experimental and theoretical analysis of glazed tube-and-sheet photovoltaic/thermal system with earth water heat exchanger cooling. *Energy Conversion and Management*, 153:576–588, 2017.

- [50] Lucas Bolivar Jaramillo and Anke Weidlich. Optimal microgrid scheduling with peak load reduction involving an electrolyzer and flexible loads. *Applied Energy*, 169:857–865, 2016.
- [51] Dirk C Jordan and SR Kurtz. Analytical improvements in pv degradation rate determination. In *Photovoltaic Specialists Conference (PVSC), 2010 35th IEEE*, pages 002688–002693. IEEE, 2010.
- [52] Dirk C Jordan, RM Smith, CR Osterwald, E Gelak, and Sarah R Kurtz. Outdoor pv degradation comparison. In *Photovoltaic Specialists Conference (PVSC), 2010 35th IEEE*, pages 002694–002697. IEEE, 2010.
- [53] Nese Kavasoglu, A Sertap Kavasoglu, and Sener Oktik. A new method of diode ideality factor extraction from dark i–v curve. *Current Applied Physics*, 9(4):833–838, 2009.
- [54] A Khalilnejad and GH Riahy. A hybrid wind-pv system performance investigation for the purpose of maximum hydrogen production and storage using advanced alkaline electrolyzer. *Energy Conversion and Management*, 80:398–406, 2014.
- [55] Mohan Kolhe and Ozcan Atlam. Empirical electrical modeling for a proton exchange membrane electrolyzer. In *Applied Superconductivity and Electromagnetic Devices (ASEMD), 2011 International Conference on*, pages 131–134. IEEE, 2011.
- [56] Joonas Koponen. Review of water electrolysis technologies and design of renewable hydrogen production systems. Technical report, Lappeenranta University of Technology, 2015.
- [57] Olaf Kruck, Fritz Crotogino, Ruth Prelicz, and Tobias Rudolph. Overview on all known underground storage technologies for hydrogen. Technical report, HyUnder, 2013.
- [58] Kari Lappalainen and Seppo Valkealahti. Analysis of shading periods caused by moving clouds. *Solar Energy*, 135:188–196, 2016.
- [59] James Larminie, Andrew Dicks, and Maurice S McDonald. *Fuel cell systems explained*, volume 2. J. Wiley Chichester, UK, 2003.
- [60] Ga Rick Lee, Lyndon Frearson, and Paul Rodden. An assessment of photovoltaic modelling software using real world performance data. In *26th European PV Solar Energy Conference*, 2011.
- [61] Feng Leng, Cher Ming Tan, and Michael Pecht. Effect of temperature on the aging rate of li ion battery operating above room temperature. *Scientific reports*, 5:12967, 2015.
- [62] Linear Technology. Linear technology - design simulation and device models. Website. <http://www.linear.com/designtools/software/>, 2017.
- [63] Sara MacAlpine, Michael Brandemuehl, and Robert Erickson. Beyond the module model and into the array: Mismatch in series strings. In *Photovoltaic Specialists Conference (PVSC), 2012 38th IEEE*, pages 003392–003396. IEEE, 2012.
- [64] Jeff Martin and Arnoud Higler. Private conversations at the Shell Technology Center Amsterdam, 2018.
- [65] MathWorks. MATLAB. Website. <https://www.mathworks.com/products/matlab.html>, 2017.
- [66] André Mermoud. Conception et dimensionnement de systèmes photovoltaïques: Introduction des modules pv en couches minces dans le logiciel PVsyst. Technical report, Université de Genève, 2005.
- [67] MetalMiner. Carbon steel prices. Website. <https://agmetminer.com/metal-prices/carbon-steel/>, last accessed on May 26th, 2018, 2018.
- [68] MetalMiner. Stainless steel prices. Website. <https://agmetminer.com/metal-prices/stainless-steel/>, last accessed on May 26th, 2018, 2018.
- [69] Ministerial Council on Renewable Energy, Hydrogen and Related Issues. Basic hydrogen strategy. Technical report, METI, 2017 2017.

-
- [70] Scott Moskowitz. The global pv inverter and mlpe landscape 2016: Prices, forecasts, market shares and vendor profiles. Technical report, Wood Mackenzie, 2016.
- [71] I Nassar-Eddine, A Obbadi, Y Errami, M Agunaou, et al. Parameter estimation of photovoltaic modules using iterative method and the lambert w function: A comparative study. *Energy Conversion and Management*, 119:37–48, 2016.
- [72] Sandro Nižetić, AM Papadopoulos, and E Giama. Comprehensive analysis and general economic-environmental evaluation of cooling techniques for photovoltaic panels, part i: Passive cooling techniques. *Energy Conversion and Management*, 149:334–354, 2017.
- [73] Sandro Nižetić, E Giama, and AM Papadopoulos. Comprehensive analysis and general economic-environmental evaluation of cooling techniques for photovoltaic panels, part ii: Active cooling techniques. *Energy Conversion and Management*, 155:301–323, 2018.
- [74] NREL. System Advisor Model (SAM). Website. <https://sam.nrel.gov/>, 2018.
- [75] Björn Nykvist and Måns Nilsson. Rapidly falling costs of battery packs for electric vehicles. *nature climate change*, 5(4):329, 2015.
- [76] Morten Nymand and Michael AE Andersen. High-efficiency isolated boost dc-dc converter for high-power low-voltage fuel-cell applications. *IEEE Transactions on Industrial Electronics*, 57(2):505–514, 2010.
- [77] OECD. World energy balances 2017. Technical report, IEA, 2017.
- [78] Ahmet Ozarslan. Large-scale hydrogen energy storage in salt caverns. *International Journal of Hydrogen Energy*, 37(19):14265–14277, 2012.
- [79] David Parra and Martin K Patel. Techno-economic implications of the electrolyser technology and size for power-to-gas systems. *International Journal of Hydrogen Energy*, 41(6):3748–3761, 2016.
- [80] Bidyut Paul. Direct-coupling of the photovoltaic array and PEM electrolyser in solar-hydrogen systems for remote area power supply. Technical report, RMIT University, 2009.
- [81] Bidyut Paul and John Andrews. Optimal coupling of pv arrays to pem electrolyzers in solar-hydrogen systems for remote area power supply. *International journal of hydrogen energy*, 33(2):490–498, 2008.
- [82] Maria Teresa Penella and Manel Gasulla. A simple and efficient mppt method for low-power pv cells. *International Journal of Photoenergy*, 2014, 2014.
- [83] Zhijun Peng, Mohammad R Herfatmanesh, and Yiming Liu. Cooled solar pv panels for output energy efficiency optimisation. *Energy Conversion and Management*, 150:949–955, 2017.
- [84] PVsyst. Photovoltaic software. Website. pvsyst.com, 2017.
- [85] QUCS. Quite universal circuit simulator. Website. <http://www.linear.com/designtools/software/>, 2017.
- [86] Nasrudin Abd Rahim, Hew Wooi Ping, Jeyraj Selvaraj, et al. Photovoltaic module modeling using simulink/matlab. *Procedia Environmental Sciences*, 17:537–546, 2013.
- [87] Christoph Rakousky, Uwe Reimer, Klaus Wippermann, Susanne Kuhri, Marcelo Carmo, Wiebke Lueke, and Detlef Stolten. Polymer electrolyte membrane water electrolysis: Restraining degradation in the presence of fluctuating power. *Journal of Power Sources*, 342:38–47, 2017.
- [88] Mohamed BH Rhouma, Adel Gastli, Lazhar Ben Brahim, Farid Touati, and Mohieddine Benamar. A simple method for extracting the parameters of the pv cell single-diode model. *Renewable Energy*, 113:885–894, 2017.

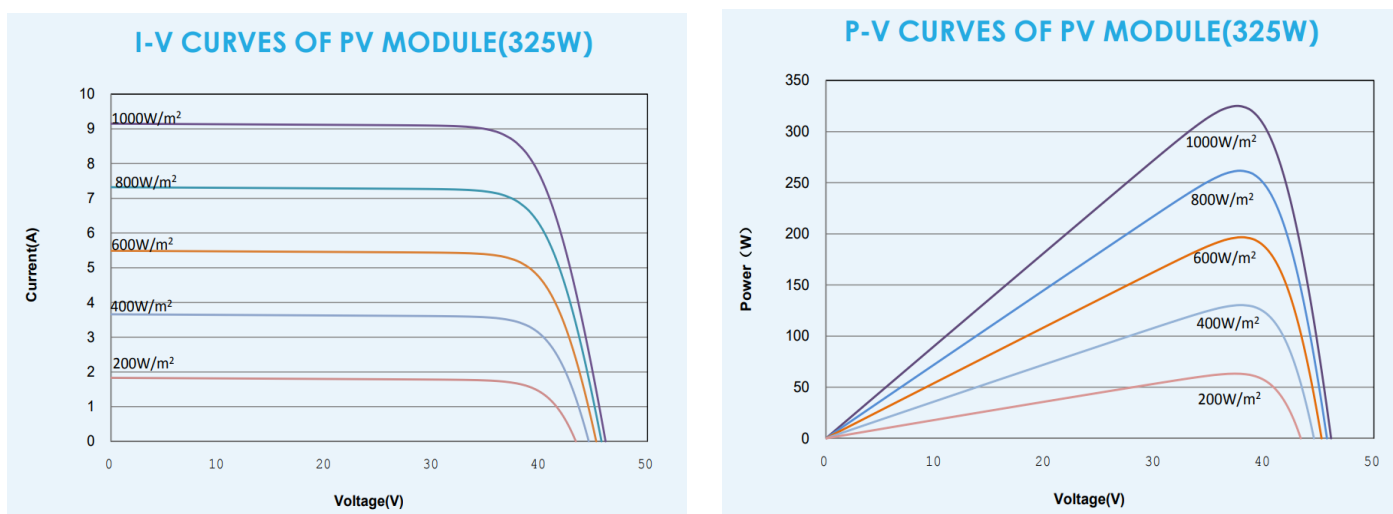
- [89] Samlex Solar. Solar cell-module-array. Website. <http://www.samlexsolar.com/learning-center/solar-cell-module-array.aspx>, 2018.
- [90] Pablo Sanchis, Jesús López, Alfredo Ursúa, Eugenio Gubía, and Luis Marroyo. On the testing, characterization, and evaluation of pv inverters and dynamic mppt performance under real varying operating conditions. *Progress in Photovoltaics: Research and Applications*, 15(6):541–556, 2007.
- [91] Diogo MF Santos, César AC Sequeira, and José L Figueiredo. Hydrogen production by alkaline water electrolysis. *Química Nova*, 36(8):1176–1193, 2013.
- [92] Kenneth J Sauer, Thomas Roessler, and Clifford W Hansen. Modeling the irradiance and temperature dependence of photovoltaic modules in PVsyst. *IEEE Journal of Photovoltaics*, 5(1):152–158, 2015.
- [93] Nahla Mohamed Abd Alrahim Shannan, Nor Zaihar Yahaya, and Balbir Singh. Single-diode model and two-diode model of pv modules: A comparison. In *Control System, Computing and Engineering (ICCSC), 2013 IEEE International Conference on*, pages 210–214. IEEE, 2013.
- [94] N Santakrus Singh, Amit Jain, and Avinashi Kapoor. Determination of the solar cell junction ideality factor using special trans function theory (stft). *Solar Energy Materials and Solar Cells*, 93(8):1423–1426, 2009.
- [95] Trina Solar. Tallmax. Website. <http://www.trinasolar.com/us/product/tallmax?cellType=Multicrystalline#profamilylist>, February 2017.
- [96] Sven Teske, Steve Sawyer, Oliver Schäfer, Thomas Pregger, Sonja Simon, Tobias Naegler, Stephan Schmid, Enver Doruk Özdemir, Johannes Pagenkopf, Florian Kleiner, et al. Energy [R]evolution - A Sustainable World Energy Outlook 2015. Technical report, Greenpeace International, 2015.
- [97] Øystein Ulleberg. Modeling of advanced alkaline electrolyzers: a system simulation approach. *International journal of hydrogen energy*, 28(1):21–33, 2003.
- [98] Alfredo Ursua, Luis M Gandia, and Pablo Sanchis. Hydrogen production from water electrolysis: current status and future trends. *Proceedings of the IEEE*, 100(2):410–426, 2012.
- [99] Alfredo Ursúa, Ernesto L Barrios, Julio Pascual, Idoia San Martín, and Pablo Sanchis. Integration of commercial alkaline water electrolyzers with renewable energies: limitations and improvements. *International Journal of Hydrogen Energy*, 41(30):12852–12861, 2016.
- [100] Valentin Software. Photovoltaic planning software PV*SOL. Website. <http://www.valentin-software.com/en/products/photovoltaics/55/pvsol>, 2017.
- [101] Lars Ole Valøen and Mark I Shoesmith. The effect of phev and hev duty cycles on battery and battery pack performance. In *PHEV 2007 Conference*, pages 4–5, 2007.
- [102] NJCM Van der Borg and MJ Jansen. Energy loss due to shading in a bipv application. In *Photovoltaic Energy Conversion, 2003. Proceedings of 3rd World Conference on*, volume 3, pages 2220–2222. IEEE, 2003.
- [103] Visual Capitalist. Experts are hilariously bad at forecasting solar installations. Website. <http://www.visualcapitalist.com/experts-bad-forecasting-solar/>, 2018.
- [104] Rong-Jong Wai, Chung-You Lin, Rou-Yong Duan, and Yung-Ruei Chang. High-efficiency dc-dc converter with high voltage gain and reduced switch stress. *IEEE Transactions on Industrial Electronics*, 54(1):354–364, 2007.
- [105] Geoff Walker et al. Evaluating mppt converter topologies using a matlab pv model. *Journal of Electrical & Electronics Engineering, Australia*, 21(1):49, 2001.
- [106] Weidong Xiao, William G Dunford, and Antoine Capel. A novel modeling method for photovoltaic cells. In *Power Electronics Specialists Conference, 2004. PESC 04. 2004 IEEE 35th Annual*, volume 3, pages 1950–1956. IEEE, 2004.

-
- [107] Tan Yates, Bradley Hibberd, and B Solar. Production modeling for grid-tied pv systems. Technical report, SolarPro, 2010.
- [108] Kai Zeng and Dongke Zhang. Recent progress in alkaline water electrolysis for hydrogen production and applications. *Progress in Energy and Combustion Science*, 36(3):307–326, 2010.
- [109] Andreas Züttel, Andreas Borgschulte, and Louis Schlapbach. *Hydrogen as a future energy carrier*. John Wiley & Sons, 2011.

Appendix

A PV panel characteristics

In PVsyst the module that has been simulated is the Trina Solar Tallmax 335 W_p module. For the full datasheet see [95]. Below are some excerpts of the datasheet.



(a) Irradiance dependence of the I-V curve.

(b) Irradiance dependence of the I-V curve.

Figure A.1: Characteristic I-V and P-V curves of Tallmax modules, taken from [95].

Table A.1: Module parameters for the Tallmax modules, taken from [95].

	At STC	At NOCT	
Peak Output P_{mpp}	335	249	[W]
V_{mpp}	37.6	34.8	[V]
I_{mpp}	8.91	7.14	[A]
V_{oc}	46.0	42.6	[V]
I_{sc}	9.35	7.55	[A]
Module efficiency	17.2		[%]
Number of cells	72		
Module area	1.94		[m ²]
P_{mpp} temperature coefficient	-0.41		[% C ⁻¹]
V_{oc} temperature coefficient	-0.32		[% C ⁻¹]
I_{sc} temperature coefficient	0.05		[% C ⁻¹]

B SMA Central Inverter Datasheet

SUNNY CENTRAL 1500 V

Technical Data	Sunny Central 2500-EV	Sunny Central 2750-EV
Input (DC)		
MPP voltage range V_{DC} (at 25 °C / at 50 °C)	800 V to 1425 V / 778 V to 1275 V	877 V to 1425 V / 849 V to 1275 V
Min. input voltage $V_{DC, min}$ / Start voltage $V_{DC, Start}$	778 V / 928 V	849 V / 999 V
Max. input voltage $V_{DC, max}$	1500 V	1500 V
Max. input current $I_{DC, max}$ (at 25 °C / at 50 °C)	3200 A / 2956 A	3200 A / 2956 A
Max. short-circuit current rating	6400 A	6400 A
Number of DC inputs	32	32
Max. number of DC cables per DC input (for each polarity)	2 x 800 kcmil, 2 x 400 mm ²	2 x 800 kcmil, 2 x 400 mm ²
Integrated zone monitoring	○	○
Available DC fuse sizes (per input)	200 A, 250 A, 315 A, 350 A, 400 A, 450 A, 500 A	
Output (AC)		
Nominal AC power at $\cos \phi = 1$ (at 25 °C / at 40 °C / at 50 °C)	2500 kVA / 2350 kVA / 2250 kVA	2750 kVA / 2600 kVA / 2500 kVA
Nominal AC power at $\cos \phi = 0.8$ (at 25 °C / at 40 °C / at 50 °C)	2000 kW / 1880 kW / 1800 kW	2200 kW / 2080 kW / 2000 kW
Nominal AC current $I_{AC, nom} = \text{Max. output current } I_{AC, max}$	2646 A	2674 A
Max. total harmonic distortion	< 3% at nominal power	< 3% at nominal power
Nominal AC voltage / nominal AC voltage range ^{1) 8)}	550 V / 440 V to 660 V	600 V / 480 V to 690 V
AC power frequency	50 Hz / 47 Hz to 53 Hz 60 Hz / 57 Hz to 63 Hz	50 Hz / 47 Hz to 53 Hz 60 Hz / 57 Hz to 63 Hz
Min. short-circuit ratio at the AC terminals	> 2	> 2 ⁹⁾
Power factor at rated power / displacement power factor adjustable ⁸⁾	● 1 / 0.8 overexcited to 0.8 underexcited ¹⁰⁾ ○ 1 / 0.0 overexcited to 0.0 underexcited ¹⁰⁾	
Efficiency		
Max. efficiency ²⁾ / European efficiency ²⁾ / CEC efficiency ³⁾	98.6% / 98.3% / 98.0%	98.7% / 98.5% / 98.5%
Protective Devices		
Input-side disconnection point	DC load-break switch	
Output-side disconnection point	AC circuit breaker	
DC overvoltage protection	Surge arrester, type I	
AC overvoltage protection (optional)	Surge arrester, class I	
Lightning protection (according to IEC 62305-1)	Lightning Protection Level III	
Ground-fault monitoring / remote ground-fault monitoring	○ / ○	
Insulation monitoring	○	
Degree of protection: electronics / air duct / connection area (as per IEC 60529)	IP65 / IP34 / IP34	
General Data		
Dimensions (W / H / D)	2780 / 2318 / 1588 mm (109.4 / 91.3 / 62.5 inch)	
Weight	< 3400 kg / < 7496 lb	
Self-consumption (max. ⁴⁾ / partial load ⁵⁾ / average ⁶⁾	< 8100 W / < 1800 W / < 2000 W	
Self-consumption (standby)	< 370 W	
Internal auxiliary power supply	Integrated 8.4 kVA transformer	
Operating temperature range ⁸⁾	-25 to 60 °C / -13 to 140 °F	
Noise emission ⁷⁾	64,3 dB(A)	
Temperature range (standby)	-40 to 60 °C / -40 to 140 °F	
Temperature range (storage)	-40 to 70 °C / -40 to 158 °F	
Max. permissible value for relative humidity (condensing / non-condensing)	95% to 100% (2 month / year) / 0% to 95%	
Maximum operating altitude above MSL ⁸⁾ 1000 m / 2000 m / 3000 m	● / ○ / ○ (earlier temperature-dependent derating)	
Fresh air consumption	6500 m ³ /h	
Features		
DC connection	Terminal lug on each input (without fuse)	
AC connection	With busbar system (three busbars, one per line conductor)	
Communication	Ethernet, Modbus Master, Modbus Slave	
Communication with SMA string monitor (transmission medium)	Modbus TCP / Ethernet (FO MM, Cat-5)	
Enclosure / roof color	RAL 9016 / RAL 7004	
Display	● Identicator lights / ○ HMI touchscreen (10.1") ○ (2.5 kVA)	
Supply transformer for external loads	○ (2.5 kVA)	
Standards and directives complied with	CE, IEC / EN 62109-1, IEC / EN 62109-2, BDEW-MSRL, IEEI 547, Arrêté du 23/04/08	
EMC standards	EN 55011:2011-4, IEC / EN 61000-6-2, EN 55022, CISPR 22:2008 modified class A, FCC Part 15 Class A	
Quality standards and directives complied with	VDI/VDE 2862 page 2, DIN EN ISO 9001	
● Standard features ○ Optional		
Type designation	SC-2500-EV-10	SC-2750-EV-10

1) At nominal AC voltage, nominal AC power decreases in the same proportion

2) Efficiency measured without internal power supply

3) Efficiency measured with internal power supply

4) Self-consumption at rated operation

5) Self-consumption at < 75% P_n at 25 °C6) Self-consumption averaged out from 5% to 100% P_n at 25 °C

7) Sound pressure level at a distance of 10 m

8) Values apply only to inverters. Permissible values for SMA MV solutions from SMA can be found in the corresponding data sheets.

9) A short-circuit ratio of < 2 requires a special approval from SMA

10) Depending on the DC voltage